University of Nottingham

PhD in Physics

Novel exploitation of cold atom experimental techniques for the development of Quantum Technologies

Candidate: David Johnson

Supervisors: Dr. Lucia Hackermüller
Dr. Weibin Li

October 22, 2024

Abstract

Ultracold atom experiments permit a wide range of applications within the field of quantum technologies by studying atom - photon interactions at micro kelvin temperatures. Cold atom systems are already used in a variety of fields including developing quantum computers, high precision sensors such as magnetometers and gravimeters, tests of fundamental physics including detecting dark matter and tests of quantum gravity and many, many more.

The aim of this thesis is to demonstrate over the course five different projects the techniques needed to improve the applications of cold atom systems. There are two larger projects, one of which seeks to demonstrate photon storage in a waveguide chip, which offers an alternative method to quantum computer development than the current method depending on Rydberg atoms. The other intends to use multi frequency light to increase the amount of atoms that can be trapped in cold atom experiments, which would improve the sensitivity of cold atom magnetometers, gravitimeters and other cold atom based sensors currently in use, and also develop the use of cold atom experiments to test theories of quantum gravity.

The other three projects are smaller in scope and look to offer improvements in deploying cold atom systems outside of laboratory conditions. This includes using dual frequency locking to improve laser stability, testing 3D printed vapour cells for their optical properties and usability in cold atom systems and laser locking, and finally the use of coating 3D printed designs with Non Evaporable Getters (NEGs) to improve their passive pumping rate. These NEGs could then be used along side or replace active pumps which are far heavier, bulkier and power consuming. The overarching aim of these smaller projects is to make cold atom systems smaller, lighter and more stable against background noise, in order to bring these experiments 'out of the lab' and improve their applicability in real world situations. The terms 3D printing and additive manufacturing are used interchangeably throughout this thesis.

Declaration of Authorship

I, David Johnson, declare that this thesis titled, "Novel exploitation of cold atom experimental techniques for the development of Quantum Technologies" and the work presented in it are my own. I confirm that:

- This work was done wholly or mainly while in candidature for a research degree at this University.
- Where any part of this thesis has previously been submitted for a degree or any other qualification at this University or any other institution, this has been clearly stated.
- Where I have consulted the published work of others, this is always clearly attributed.
- Where I have quoted from the work of others, the source is always given. With the exception of such quotations, this thesis is entirely my own work.
- I have acknowledged all main sources of help.
- Where the thesis is based on work done by myself jointly with others, I have made clear exactly what was done by others and what I have contributed myself.

Acknowledgements

Thanks is given to Dr Lucia Hackermüller for her role as a supervisor, providing key feedback and support throughout my PhD. Dr Nathan Cooper has helped directly in all of the experimental projects discussed in this thesis and in developing my own skills as a scientist. Ben Hopton, Matt Overton and Daniele Baldolini are thanked for invaluable contributions in the various experiments undertaken as part of my PhD. Finally, I thank my family for always giving me the love and support I needed.

All CAD designs presented in this work were produced by Ben Hopton. Several diagrams in this thesis were made with the aid of the Inkscape ComponentLibrary on quantum optics, made by Alexander Franzen. All diagrams not made by me have been attributed to their original author.

Contents

List of Figures

Abbreviations

MOT	Magneto Optical Trap
DP	Dipole
DT	Dipole Trap
EIT	Electromagnetically Induced Transparency
AM	Additive Manufacturing/Additively Manufactured
DAVLL	Dichroic Atomic Vapour Laser Locking
F - P	Fabry - Perot (Interferometer)
VCO	Voltage Controlled Oscillator
ECDL	External Cavity Diode Laser
DFB	Distributed Feedback (laser)
TA	Tapered Amplifier
PI	Proportional Integral
SPCM	Single Photon Counter Module
AOM	Acusto Optical Modulator
CCD	Charged Coupled Device
ASE	Amplified Spontaneous Emission
FSR	Free Spectral Range
BEC	Bose Einstein Condensate
CAD	Computer Aided Design
NEG	Non Evaporable Getter

Chapter 1

Introduction

Since the first demonstration of a Magneto Optical Trap (MOT) in 1987 [1], the study of atom–photon interactions and optical confinement of atoms have been central to the development of quantum technologies. This has resulted in a wide range of applications in sensors, medical imaging and fundamental research. There is thus a huge interest in developing these technologies and understanding the underlying physics. This thesis will cover five projects within the field of ultracold atoms which seek to advance quantum techologies in a variety of ways.

The two major projects are demonstrating Electromagnetically Induced Transparency (EIT) in a waveguide chip and utilising multiple frequency MOTs to increase the size of atom clouds, with the eventual aim of testing certain theories of quantum gravity [2]. The three smaller projects involved demonstrating a novel 3D printed vapour cell for use in brain imaging magnetometers, developing laser frequency stabilisation techniques, and optimising the using of passive vacuum pumps for satellite based quantum sensors. Demonstrating EIT in a waveguide chip would offer new approaches to quantum computing, whilst the multi–frequency MOT sought to improve the sensitivity of all atom based quantum sensors and to build towards testing theories of quantum gravity [2].

The first thirty months of my PhD were mainly spent on demonstrating EIT in a waveguide chip, with the hope of eventually demonstrating 'slow light'. EIT is the phenomenon by which the relative absorption of resonant light on an atom cloud is reduced by an incident control beam [3]. This is because the control beam pumps the atoms into a dark state relative to the probe beam, so the atoms can no longer absorb the probe light. By controlling the relative absorption of an incident beam in this way, we can create an 'optical transistor'. Demonstrating this technique has potential applications in building quantum computers [4–6], which would revolutionise fields such as cryptography and database searches [7].

Additionally, when the control beam is on, it increases the refractive index of the atom cloud such that the group velocity of the resonant photons is greatly reduced. This leads to the phenomenon of 'slow light', which could be used as a means of storing information inside the atom cloud. The aim of the project

is to test how practical this approach might be, by using a wave–guide chip to measure how much control over the photons can be achieved using this method [8, 9]. A fibre with a laser drilled hole is placed in a vacuum chamber, and atoms are moved from a MOT into the hole in the fibre using a dipole trap, which holds the atoms inside the hole. Photons of a specific frequency are then sent along the fibre to interact with the atoms, and by measuring the relative absorption of the light as a function of the control frequency, we can demonstrate EIT. We can then estimate the optical depth of the atom cloud, and thus the expected photon group velocity. Thus, we will also attempt to directly measure the group velocity of photons inside the atom cloud by observing the relative delay with the control beam on. This will demonstrate how well information could be stored and then extracted using this method. EIT has already been demonstrated in previous experiments, such as inside a nanofibre [10], using metamaterials [11], Rydberg atoms [12], and other systems [13].

A wave–guide chip is used as the interaction area is smaller [14, 15], allowing for the light to be tightly focused onto a small interaction region. It also allows this technique to be highly scalable, as laser drilled holes can be in principle placed anywhere along a given fibre. By drilling multiple holes along the same fibre, interactions between the atom clouds can be mediated by photons travelling through the fibre. The wave–guide chip can also be very flexible in its design, for example allowing for a single fibre to divide into multiple ones [16], or having multiple fibres to be combined into a single fibre. This method thus allows for a variety of complex designs, offering advantages over other quantum computer designs which depend on Rydberg atoms [17, 18]. At the end of my work on this project, we had successfully demonstrated EIT in the fibre by measuring the transmission of light through the fibre. Since then, another PhD student has directly measured the group velocity of photons in the hole in the fibre, and demonstrated new Bayesian techniques for improving the data collection rate. This remains an active research project.

The last eighteen months of my PhD have been spent on developing larger atoms traps for improved sensing. A wide range of sensors such as magnetometers [19], accelerometers and gravimeters [20, 21] rely on cold atom traps. Additionally, a range of fundamental tests of physics also rely on cold atom sensors, such as efforts to test certain theories of quantum gravity, and to search for dark matter. A recent proposal to use cold atom traps to examine theories of quantum gravity is found here [2], and another to test theories on spontaneous wavefunction collapse [22]. In all these applications, the sensitivity depends on the number of atoms trapped, so that any techniques which improve the size of these atom traps will thus have significant implications for a variety of fields.

The principal method used to increase the number of cold atom trapped is to use multiple frequency components. A simpler method is to use more powerful beams with larger diameters, but this is physically uninteresting and expensive in terms of equipment, power and space requirements. Using multiple frequencies allows a much larger range of atom velocities to be trapped by these beams, dramatically increasing loading rates of atoms clouds and thus provides a larger atom cloud at equilibrium. Previous work has demonstrated a three to

five–fold increase in trapped atom number using dual frequency cooling beams [23, 24]. This method will, however, induce greater collisional losses within the atom trap, and so methods must also be developed to remove or minimise this effect. One such method is using axicons to alter the power distribution across the beam to create a 'dark spot' MOT. This can be considered the inverse of a Gaussian beam, so that the light intensity is strongest at the edges and weakest in the middle. There are additional methods being developed which will be discussed in in the chapter on multi frequency MOTs.

Finally, there are three smaller projects with a variety of aims, but in general seek to make cold atom experiments more stable and more portable. These develop techniques that can be used generally in cold atom experiments or other applications that seek to improve laser frequency stability or reduce the size of vacuum pumps, for example.

1.1 Thesis Layout

The rest of this thesis will cover in detail the work discussed above. The next chapter will discuss the theoretical foundations of cold atoms physics and the equations describing atom photon interactions and atom trapping. This will only be a relatively brief overview of the relevant equations, as the details have been covered in many other works and will not be repeated here. A more in depth overview of the theory of EIT will be given, however, as this is more specific to our experiment and will become relevant in the chapter on EIT.

The third chapter will describe how lasers are stabilised with respect to frequency and polarisation. Three separate locking techniques will be discussed, as well as the advantages and disadvantages of each. We also describe how absorption imaging is used to find the atom number, atom density and temperature of cold atom clouds. These fundamental techniques are common throughout the different projects I have contributed to over my PhD, and so are collected into this chapter for ease of reading. The specifics of each project will be covered in the relevant chapter.

The fourth chapter will be dedicated to my work on demonstrating EIT in a wave–guide chip. This is an experiment with significant work done by others before I joined the group, and has continued to develop after I moved onto the project on multi frequency MOTs. I will thus only discuss the progress made whilst I was a part of that project. This includes demonstrating EIT in a wave–guide chip, as well as changes made to the setup. It will briefly cover work done after I left, but only for showing how the experiment has developed, and will clearly mark work that is not my own.

The fifth chapter will cover the last eighteen months of my PhD working on constructing a multi–frequency MOT, which potentially could develop into forming a large BEC to test theories of quantum gravity. The process of creating and analysing the multi–frequency comb is discussed, and used to demonstrate an increase in loading rate. Unlike the project on EIT, this is a new experiment which I joined from virtually the beginning. This is very much an ongoing

project with much work left to be done, and so will also discuss the potential developments of the project after I finish my PhD.

The sixth chapter discusses the smaller projects I have worked on. The three projects are as follows: developing a novel method of laser locking using dual frequency techniques for improved laser frequency stability and a reduction in needed optical components; testing and developing additively manufactured vapour cells for use in magnetometers by measuring the frequency stability of a laser locked using such a cell; and testing 3D printed samples coated with a getter material to enable an improvement in passive pumping techniques, which could supplant or even replace more bulky active vacuum pumps.

The last chapter serves to conclude the thesis. Tying together so many separate projects into a cohesive thesis is itself a challenge, but working on such a diverse range of experiments has greatly improved my own knowledge of cold atom techniques. The final conclusions of each project are reiterated, and subsequent developments are also discussed.

1.2 Publications

I have co-authored the following papers which are either published, submitted or still in preparation:

- Nathan Cooper, Somaya Madkhaly, David Johnson, Benjamin Hopton, Daniele Baldolini, and Lucia Hackermüller. "Dual-frequency Doppler-free spectroscopy for simultaneous laser stabilization in compact atomic physics experiments". In Phys. Rev. A Vol. 108, Iss. 1 — July 2023. Included in appendix.

- Feiran Wang, Nathan Cooper, Yinfeng He, Benjamin Hopton, David Johnson, Peng Zhao, Christopher J. Tuck, Richard Hague, T. Mark Fromhold, Ricky D. Wildman, Lyudmila Turyanska, and Lucia Hackermüller. "Additive manufacturing of functionalised atomic vapour cells for next-generation quantum technologies". Submitted to IOP Quantum Science and Technology. Included in appendix.

- Nathan Cooper, David Johnson, Benjamin Hopton, Laurence Coles, Manolis Papastavrou, Lucia Hackermüller, David Stupple, Edward Wilson and James Robinson. "Enhanced passive pumping for high vacuum systems via additively manufactured mesoscopic surface structures". In preparation.

- Nathan Cooper, Jesus Rubio, Matt Overton, David Johnson, Lucia Hackermüller and Janet Anders. "Demonstration of Bayesian Sensing with Adaptive Symmetry-Informed Strategies for Trapped Atom Experiments". In preparation.

Chapter 2

Theoretical Background

Throughout this thesis we confine our interest in atom–photon interactions strictly to alkali metals, in particular rubidium and caesium. This is mainly because alkali atoms in their ground state possess only 1 electron in their outermost electron orbital. As such, the relevant mathematics are greatly simplified, by allowing us to ignore the interactions between the other electrons and assuming that the system can be described by the interaction between the outermost electron and the nucleus in the centre, who's electric charge is shielded by the other electrons. Although a greatly simplified system, this approach can still allow us to describe the atom–photon interactions with sufficient accuracy. Additionally, the fine structure is such that these atoms can be excited along the D_2 line with near infrared light. This is important because lasers at these frequencies are well developed, being both reasonably cheap and possessing good laser characteristics in terms of power, stability, free spectral range and beam quality. The only stable isotopes [25, 26] of these elements are ^{133}Cs for caesium and ^{85}Rb rubidium, although ^{87}Rb has a half life of roughly 50 billion years [27].

The overarching electronic structure is similar for both caesium and rubidium. The details of the hyperfine states of these species and their interactions with photons have been discussed in great detail [25–29]. Herein we give an outline of the electronic structure of these alkali metals, and how their interaction with light can be exploited to trap and cool atom clouds. The hyperfine structures of ^{133}Cs and ^{85}Rb are shown in Figures 2.1 and 2.2.

We are particularly interested in F, the total atomic angular momentum [28], which is given by the equation

$$F = J + I = L + S + I, \tag{2.1}$$

where J is the total electron angular momentum and I is the total nuclear angular momentum. J can be written as the sum of L, the orbital angular momentum of the electron and S, the spin angular momentum of the electron. By studying how these separate angular momenta interact with each other, the hyperfine state of the atom can be derived. The spin angular moment S

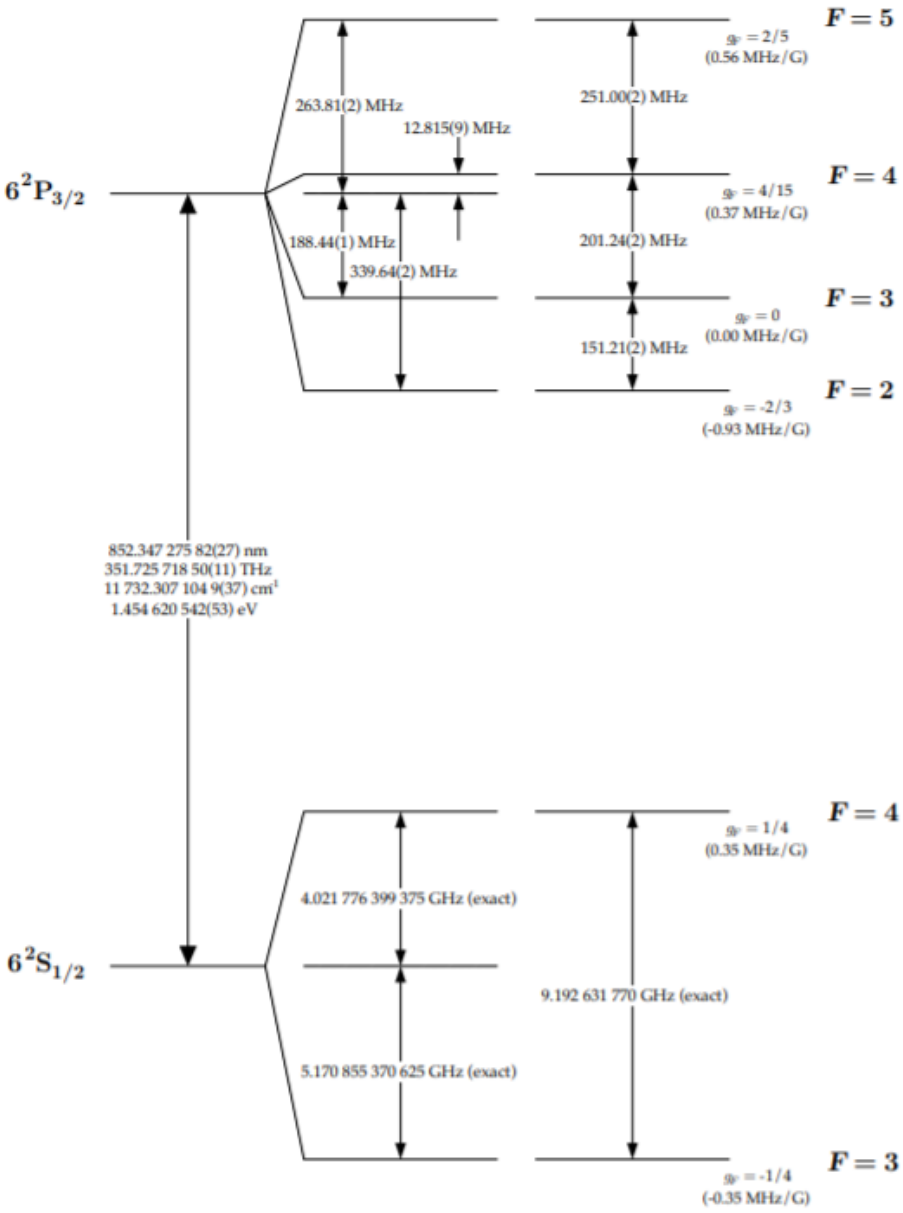

Figure 2.1: Hyperfine structure of the D_2 line of ^{133}Cs [26].

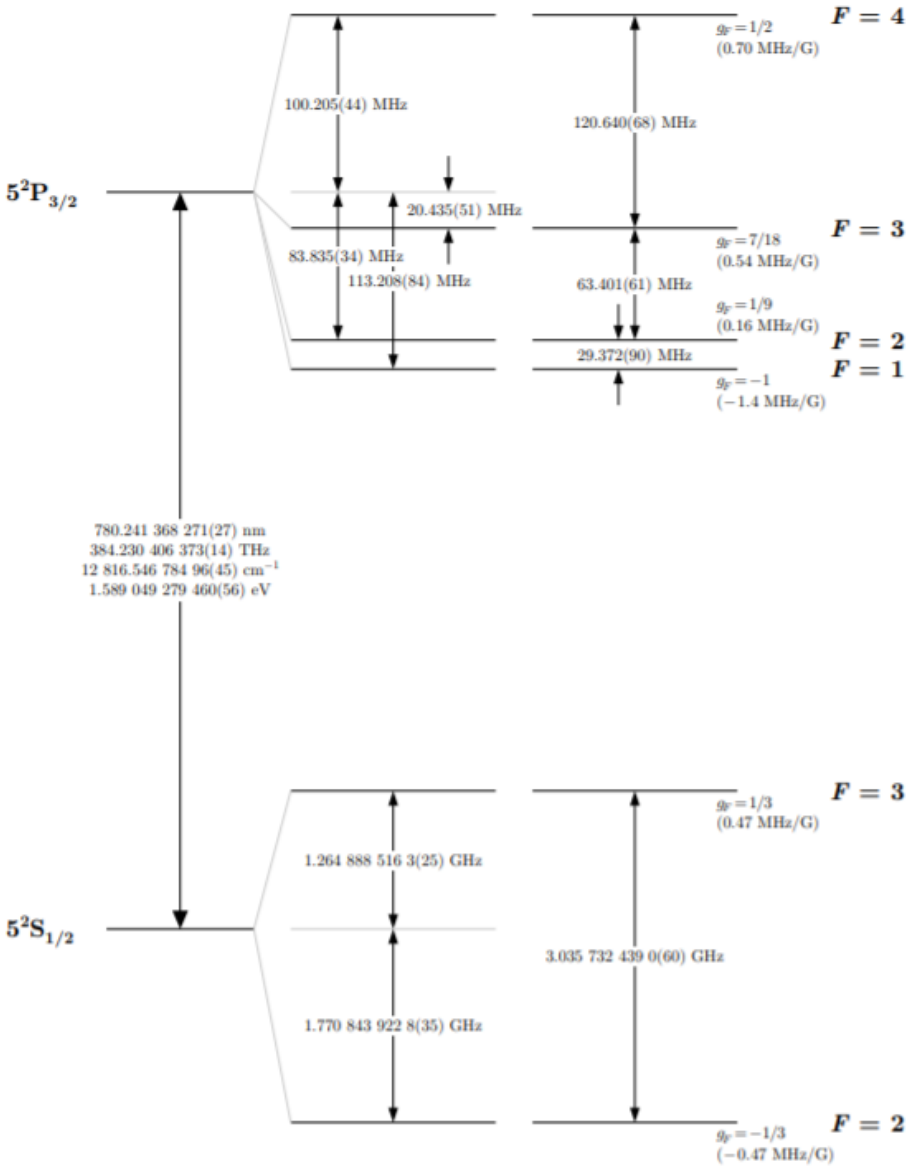

Figure 2.2: Hyperfine structure of the D_2 line of ^{85}Rb [25].

is either 1/2 or -1/2, depending on the relative spin compared to the overall angular momentum. The nuclear angular momentum I depends on the atom being studied, with ^{133}Cs having a nuclear spin of 7/2 [26] and ^{85}Rb having a nuclear spin of 5/2 [25]. J will vary depending on the orbital the electron is in. F can take any integer value [28, 30] that satisfies

$$|J - I| \leq F \leq J + I. \tag{2.2}$$

Finally, it can be shown [28] that in a weak magnetic field, the degeneracy of the m_f states are lifted according to

$$\delta E = g_F \mu_B m_f B_z, \tag{2.3}$$

where the magnetic field strength is given by B_z and g_F and μ_B are the Landé g-factor and Bohr magneton respectively. This is called the anomalous Zeeman effect.

2.1 Atom - photon interactions

Atom–photon interactions underpin virtually all experiments in cold atom physics. Here again we see the benefit of utilising alkali metals, as the transition frequencies of the valence electron are very different from those of the rest of the electrons, so by only considering light close to the resonant transitions of the outer electron, and far detuned from the transition frequencies of all the other electrons, we can treat the atom as a two level system.

A simple perturbation theory [28, 29] uses a semi-classical formalism based on a two level atom with ground state $|g\rangle$ and excited state $|e\rangle$, with resonant frequency ω_0. Light is treated as a classical electromagnetic wave travelling in the z - axis so that $E = \epsilon E_0 \cos(kz - \omega t)$. The unit vector of the electric field ϵ must be orthogonal to the z - axis. The magnitude of the electric field is E_0, while k and ω are the wave vector and frequency of the electromagnetic wave.

The Hamiltonian H can then be written as the sum of the uncoupled Hamiltonian H_0 and the interaction Hamiltonian H_{int}

$$H = H_0 + H_{int} = \hbar\omega_0 |e\rangle\langle e| - d \cdot E, \tag{2.4}$$

where d is the electric dipole moment of the atom. We assume the driving frequency of the electric field is not far detuned from the atomic resonance frequency, allowing us to apply to the rotating wave approximation. We thus exclude higher frequency terms and concentrate only on terms dependant on the detuning $\delta = \omega_0 - \omega$.

Defining the Rabi frequency as

$$\Omega = \frac{-\langle g|\epsilon \cdot d|e\rangle E_0}{\hbar}, \tag{2.5}$$

the Hamiltonian can be rewritten in the rotating frame as

$$H = \hbar\omega_0|e\rangle\langle e| + \frac{\hbar}{2}[\Omega^* a + \Omega a^\dagger]. \tag{2.6}$$

Here we have defined the creation and annihilation operators as $a^\dagger = |e\rangle\langle g|$ and $a = |g\rangle\langle e|$ respectively. This simplified model allows the populations of the ground and excited states to be calculated as a function of time, but critically ignores the decay of the excited state by spontaneous emission.

A more general approach [28, 31] requires using the density matrix

$$\rho = \begin{pmatrix} \rho_{gg} & \rho_{ge} \\ \rho_{eg} & \rho_{ee} \end{pmatrix}, \tag{2.7}$$

where the diagonal terms are probabilities for the occupation of the ground and excited states and the off-diagonals are the coherence values. With this, the spontaneous emission process can be accounted for and the time evolution of the density matrix can be described using the equation

$$\frac{\partial\rho}{\partial t} = \frac{i}{\hbar}[\rho, H] - \frac{1}{2}\begin{pmatrix} -2\Gamma\rho_{gg} & \Gamma\rho_{ge} \\ \Gamma\rho_{eg} & 2\Gamma\rho_{ee} \end{pmatrix}, \tag{2.8}$$

where Γ is the spontaneous decay rate of $|e\rangle$. The steady state solution for the excited state can then be found as

$$\tilde{\rho_{ee}} = \frac{\Omega^2/4}{\delta^2 + \Omega^2/2 + \Gamma^2/4}. \tag{2.9}$$

2.2 Doppler Cooling

Slowing thermal velocity atoms is vital before they can be trapped, as the small radiation forces from the laser means the trap depth is significantly smaller than the kinetic energy of room temperature atoms. Doppler cooling relies on a continuous cycle of absorption and spontaneous emission processes. The spontaneous emission occurs isotropically, and so the net momentum gain is zero. Photon absorption, however, only occurs in the direction of the laser beam, and so over time the atom will be pushed away from the beam. The net force on the atom by a beam of photons with momentum $\hbar k$ is given by [28, 31]

$$\delta F = \hbar k\kappa = \hbar k\Gamma\rho_{ee}, \tag{2.10}$$

where we define the scattering rate as $\kappa = \Gamma\rho_{ee}$. To slow the atoms, the beam is slightly red detuned from the resonant frequency. Thus, when an atom is travelling against the beam direction, it is blue shifted into resonance. The atom can then absorb a photon. As the atom is travelling against the beam direction, the momentum change is in the opposite direction to the atom's initial velocity, and so the atom slows down. As the spontaneous emission process is isotropic, over repeated collisions the atom will lose momentum, and so slow down. Importantly, if the light is instead blue detuned from the atomic resonance frequency, then the atom will instead only absorb a photon when travelling

co-propagating with the light. This means when the atom absorb a photon, the atom will gain kinetic energy. This gain in kinetic energy can allow the atom to escape a MOT, so it is very important to prevent any blue detuned light from incidenting onto these atoms.

Additionally, the atom can only be slowed if the Doppler shift brings the atom onto resonance with the beam, so the range of atom velocities that are address by the beam is limited to $\Delta v \approx \Gamma k$ [28]. This means only a small fraction of the total atoms present will be addressed by the slowing beam. In a MOT, the magnetic field will increase this velocity range, and in chapter 5 we will discuss using multi-frequency light to address a significantly larger velocity range. Defining the saturation intensity as [28]

$$I_{sat} = \frac{\pi h c \Gamma}{3\lambda^3}, \tag{2.11}$$

equation 2.10 can be rewritten as

$$\delta F = \frac{\hbar k \Gamma}{2} \frac{I/I_{sat}}{1 + I/I_{sat} + 4\delta^2/\Gamma^2}. \tag{2.12}$$

As the light intensity I tends to infinity, the scattering force tends to $\hbar k\Gamma/2$, because the fractional populations of the ground and excited states both approach $1/2$.

There is however, a limit to which atoms can be cooled by this process, known as the Doppler temperature. This is because whilst the isotropic nature of spontaneous emission means the net momentum change is zero, the net change in kinetic energy is greater than zero. This limits the Doppler temperature to [28]

$$T_D = \frac{\hbar \Gamma}{2k_B}. \tag{2.13}$$

For ^{133}Cs this temperature is $125\mu K$ [26] and for ^{85}Rb this temperature is $146\mu K$ [25].

2.3 Magneto Optical Traps

We have explained how atoms can by slowed, to a point, by incident beams of light slightly red detuned from transition. We would also like to confine these atoms to a given region, for which Magneto Optical Traps (MOTs) are excellent. Only a brief overview will be given here. A more detailed analysis can be found in [28, 30, 31].

The details of how a MOT works can be broken down into slowing and trapping. To trap the atoms, their kinetic energy must first be brought below the trapping potential. To do this, we have six orthogonal red detuned beams pointing towards the centre. As discussed in the previous section, any atoms moving out of the MOT will be addressed by the beams and so slowed down.

This alone is insufficient to trap the atoms, as the restoring force is only velocity dependant and not position dependant.

For atom trapping, the idea is to use an anti–Helmholtz coil configuration, as shown in Figure 2.3, to create a quadrupole trap. At the centre of the trap there is linear magnetic field gradient so that in the centre of the trap the B field is zero, but further away from the trap the Zeeman effect shifts the atoms on to resonance with the incoming beam, pushing the atom back towards the centre of the trap. By using six beams pointing inwards on each axis, the atoms can be confined, provided that they are first cooled below the trap depth.

Figure 2.4 shows a simplified 1D MOT, where we take $J = 0$ as the ground state and $J = 1$ as the excited state. Consider an atom in the centre moving towards the right. The magnetic field shifts the transition from the ground state to the $m_J = +1$ state onto resonance with the red detuned beam, whilst the transition to the $m_J = -1$ state is shifted further away from resonance. Selection rules dictate that photons of σ_- are absorbed, pushing the atom back towards the centre of the MOT. A similar process will occur if the atoms move toward the left. The atoms are thus slowed and trapped in the centre, with the MOT coils providing a spatially dependant frequency shift.

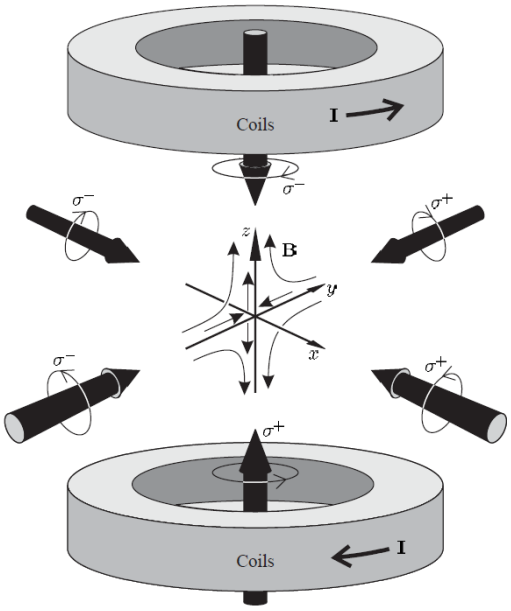

Figure 2.3: Anti - Helmholtz coil configuration to create a quadropole magnetic field. Six circularly polarised light beams trap and cool the atoms at the intersection point. Figure is adapted from [28].

The upper limit for the size of a given MOT depends on the loss rate. The main source of atom loss from a MOT are collisional losses [30], either between atoms trapped in the MOT and other atoms in the vacuum chamber,

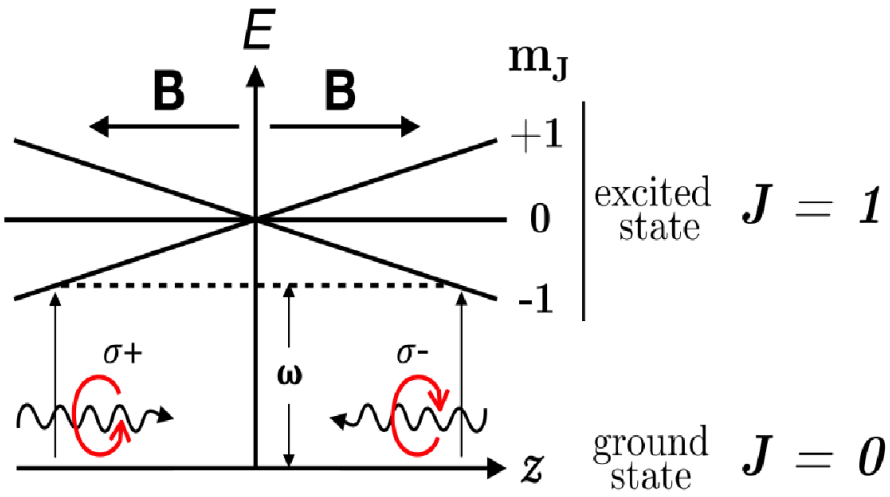

Figure 2.4: 1D MOT setup, showing how the magnetic splitting of the m_J states shift the atomic transition on resonance with the incoming beam, pushing the atom back towards the centre of the trap. Adapted from [28].

and collisions between atoms in the chamber. 3 body collisional losses only become relevant at atom densities found in BECs, and so they are ignored here. The 1 body collisions with background atoms can be reduced by reducing the vacuum pressure, which in our chambers are approximately 10^{-10} mbar. 2 body collisions can cause excitation in the atom energy states. When the state decays to release a photon, the atom gains kinetic energy which can push the atom out of the trap. These are particularly relevant as the excitation of the atomic states by light increases the rate of these two body losses. There a few methods to reduce such losses, the primary method being to reduce the temperature of the MOT. In chapter 5 we will look at a 'dark spot' MOT as another method to reduce collisional losses.

An important detail we have so far neglected is that for many atomic species, including Cs and Rb, there is no closed cooling loop i.e. after excitation, the atom can de-excite to a state that the incident light cannot excite. For example, in Rubidium we use the $F = 3 \rightarrow F' = 4$ transition for trapping and cooling, using the techniques we have so far described. It is possible, however, for the atom to de-excite via the $F' = 3 \rightarrow F = 2$ transition. The cooler light can not interact with any atoms in the $F = 2$ state, and so the atom escapes the MOT. To deal with this, we introduce another laser resonant to the $F = 2 \rightarrow F' = 3$ transition. Atoms in the $F = 2$ state are thus pumped back into the $F' = 3$ state, and can then decay back to the $F = 3$ state. This beam is, for obvious reasons, called the repumper.

2.4 Sub Doppler Cooling

Whilst examining the first MOT clouds in the late 80's, the measured temperature of the atom cloud was surprisingly found to be significantly below the Doppler limit [32]. This is due to additional cooling effects not understood until later [33]. This additional cooling effect is now called Sisyphus cooling.

The principle idea is that the counter propagating light beams interfere such that the polarisation of the total light field changes along the axis of the beam. For orthogonal linearly polarised light, the total polarisation depends on the relative phase and will shift from linear to circularly polarised and back along the beam axis. The energy of m_f states strongly depends on polarisation, so as the atom moves along the beam, the energy of the m_f states will vary as shown in Figure 2.5.

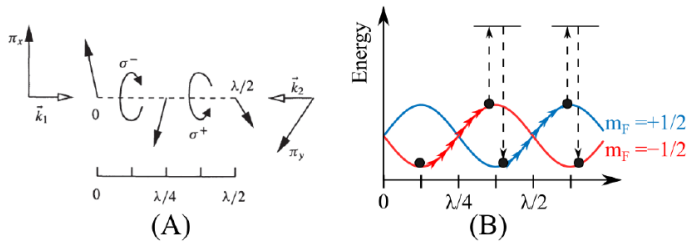

Figure 2.5: A) Polarisation of the light along the beam axis. Figure is adapted from [31]. B) Energy of m_f states as a result.

The Clebsch-Gordon coefficients mean [28] that the atom is more likely to absorb a photon at the top of the peak, and de-excite into a valley. As the emitted photon has a higher frequency and is thus more energetic, the atom must lose kinetic energy as a result, and thus slow down. This allows the atoms to be cooled below the Doppler limit to the recoil temperature, which is limited by the energy gained by the atom from emitting a single photon. The recoil temperature can be calculated [31] to be

$$T_{Recoil} = \frac{\hbar^2 k^2}{k_B m}. \tag{2.14}$$

For caesium, the recoil temperature is $180nK$ [26], and $357nK$ for rubidium [25]. These temperatures are significantly cooler than the Doppler temperatures.

For circularly polarised light, the interference between the two anti parallel beams creates a linearly polarised beam, where the direction of polarisation rotates about the axis along the beam. This is shown in Figure 2.6. If atoms are closer to one of the beams, this linearly polarised light pumps them into an m_f state which makes the atom couple more strongly to the nearer circularly polarised beam, thus slowing the atoms down. Note that this process occurs in the absence of a magnetic field, and so when used first requires forming a MOT and then ramping down the magnetic field. Whilst this does lead to further

cooling, it also removes the trapping force. As the atoms are already very cold at this point, it will take longer for the atom cloud to disperse, but there is a trade off in how much cooling can be done.

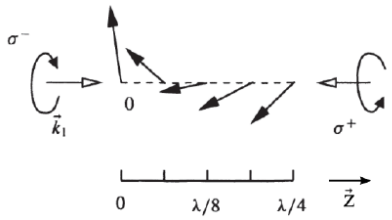

Figure 2.6: Two circularly polarising beam interfere to create a linearly polarised beam. Figure is from [31].

2.5 Dipole Trapping

To cool atoms further below the limit achievable by a MOT alone, and to be able to transport atoms from the trap to another region of interest, such as in a waveguide chip, we require a Dipole Trap. For the EIT experiment, we use a 30W 1064nm laser, which is far red detuned from the cooler and repumper transitions of Caesium ($\approx 852nm$). The principle of the Dipole Trap is that a focused, powerful beam creates a large electric field E which induces an electric dipole moment $p = \alpha E$ on the atoms in the beam, where α is the complex polarisability of the atoms. As the atomic radius of the atom ($< 1nm$) is much smaller than the wavelength of the dipole beam ($\approx 1\mu m$), the atoms can simply be treated as point dipoles. There is then an attractive force between the induced electric dipole and the electric field of the laser, which increases with the field intensity. Thus, the atoms are attracted to the focus of the beam, where the electric field is strongest. Scattering forces and radiative pressure from the dipole beam create losses from the trap which also need to be accounted for. As the dipole trap is far red detuned, the hyperfine structure of the atoms is not resolved. The dipole potential of this trap can be written as [34]

$$U(r) = -\frac{3\pi c^2}{2\omega_0^3}\left(\frac{\Gamma}{\omega_0 - \omega} + \frac{\Gamma}{\omega_0 + \omega}\right) I(r), \tag{2.15}$$

where ω_0 is the resonant frequency of the D_2 line, shown in Figure 2.1, and ω is the frequency of the dipole beam. Dipole traps can be used to further reduce the temperature of the atom cloud below the recoil limit through a process called evaporative cooling. Essentially, the trapping depth of the dipole trap is slowly decreased over time. The hottest atoms will leave the trap, whilst the remainder will re-thermalise via elastic collisions. This will result in a significant loss of atom number, but is the simplest way to achieve the low temperatures needed for a BEC.

2.6 Electromagnetically Induced Transparency

The main aim of the ErBeStA experiment is to demonstrate EIT in a waveguide chip. This is the phenomena where a cloud of atoms is optically pumped by a control beam so that it enters a dark state for another probe beam that is on resonance between the ground state and an excited state [3]. In effect, the amount of absorption of the probe beam by the atom cloud can be controlled by a control beam. Thus, we have created a light switch which is the photonic analogue of the electronic transistor. Additionally, the presence of the control beam reduces the group velocity of the probe beam inside the atom cloud. If this group velocity can be significantly reduced, then photons are effectively trapped inside the atom cloud. This method of photon storage can allow for information to be stored and retrieved via the control beam.

EIT requires a three level system. This can either be V, a ladder, or as in our system, a lambda. In a lambda system, shown in Figure 2.7, two lower states can each be excited into an upper state by the control beam and probe beam respectively. The transition between the two lower states is dipole forbidden. Our experiment uses the ^{133}Cs D_2 line, specifically the $F = 3 \rightarrow F' = 4$ as the control beam and the $F = 4 \rightarrow F' = 4$ as the probe beam. The intensity of the probe beam is assumed to be weak compared to the control beam.

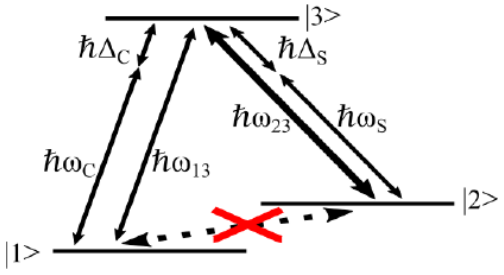

Figure 2.7: The lambda configuration for EIT.

The total applied electric field is

$$E = E_C cos(\omega_C t) + E_P cos(\omega_P t) \tag{2.16}$$

and the Hamiltonian can be written as

$$H = \Omega_s(\sigma_{13} + \sigma_{31}) + \Omega_c(\sigma_{23} + \sigma_{32}), \tag{2.17}$$

where $\sigma_{ab} = |a\rangle\langle b|$.
The time evolution of the state populations can be found using

$$\frac{\partial \rho}{\partial t} = -\frac{i}{\hbar}[H, \rho] - \frac{1}{2}\{\gamma, \rho\}. \tag{2.18}$$

We define γ as the spontaneous decay matrix. As the probe beam is weak, we assume the majority of the atoms remain in the ground state. We can thus find

$$\dot{\rho}_{12} \approx i\Omega_P + i\Omega_C\rho_{13} - \gamma\rho_{12} \tag{2.19}$$

and

$$\dot{\rho}_{13} \approx i\Omega_C\rho_{12}. \tag{2.20}$$

The susceptability χ can be defined as

$$\chi = \frac{P}{\epsilon_0 E} \tag{2.21}$$

and the polarisation density P can be found using

$$P = NTr(d\rho), \tag{2.22}$$

where N is the atom density. Inserting the steady state solution of (2.18) into (2.22), we find the dependence of the susceptibility on the control frequency ω_c is

$$\chi(\omega_c) = -\frac{N}{V\varepsilon_0}\frac{\mu^2}{\hbar}\frac{2\omega_c}{2(\omega_c^2 - \Omega_c^2) + i\omega_c\gamma}. \tag{2.23}$$

The susceptibility is an important quantity to calculate because the amount of absorption, refraction and dispersion can all be found using either the real or imaginary part of the susceptibility. The real and imaginary parts of the susceptibility are shown in Figure 2.8.

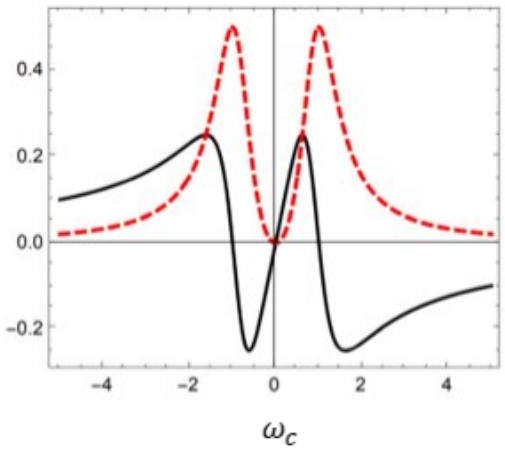

Figure 2.8: The imaginary part of the susceptibility is plotted using red dashed lines, whilst the black solid line is the real part of the susceptibility.

In particular, we can use the susceptibility to find the group velocity of the probe beam inside the atom cloud. The relationship between the two quantities is

$$v_{\mathrm{g}} = \frac{c}{n(\omega)} = \frac{c}{1 + \omega_{\mathrm{s}} \frac{\partial Re\chi(0)}{\partial \omega_{\mathrm{c}}}}. \tag{2.24}$$

We can see from Figure 2.8 that when the control beam is close to resonance, $\frac{\partial Re\chi(0)}{\partial \omega_{\mathrm{c}}} >> 0$, so the group velocity is reduced to far below the speed of light. Additionally, the absorption of the probe beam is proportional to the imaginary part of the susceptibility, which falls to zero when the control beam is on resonance.

Chapter 3

Laser stabilisation and Imaging

In general, the greatest difficulties in cold atom experiments are to do with lasers. In particular, cold atom experiments require very precise control of laser frequencies. This chapter will discuss the variety of lasers used in our experiments, how they can be frequency stabilised (called 'locking') against either an atomic transition or another laser, and how they are used to image atom clouds.

3.1 Laser stabilisation methods

As we have seen in the theory section, cold atom experiments require highly stable single mode lasers to work properly. Whilst we try to maintain stable conditions in the lab and use temperature and humidity regulators, this will not account for local variations in conditions within the lab. Additionally, some equipment will produce significant amounts of noise whilst in operation, such as vacuum pumps. As such, corrections must be made for fluctuations in temperature, pressure and humidity, as well as other noise sources such as vibrations from other components. Methods used to correct for frequency fluctuations are called laser locking. An overview of laser locking methods can be found in [35]. Generally, we use External Cavity Diode Lasers (ECDLs) and a grating mounted on a piezo to provide the cavity feedback needed for the laser. The piezo gives fine control over the angle and position of the grating, which changes the size of the cavity and the wavelength of the first order reflected back to the diode. This allows for fine control over the laser frequency. The laser diode also has a thermistor and peltier connected to a PI controller to prevent temperature drifts. For some applications, which will be discussed when appropriate, we use Distributed FeedBack lasers (DFBs). DFBs do not have an external cavity or piezo, and so the wavelength is controlled by the temperature and current. DBFs tend to be more stable than ECDLs, but have limited power output [36].

For applications where significant power is needed, Tapered Amplifiers (TA) are used. TAs amplify a seed input laser using a provided current, which can generally not exceed a given amount depending on the TA without damaging it. Providing excess current without sufficient seed power, or seeding the TA without providing current, will also damage or, given sufficient time, break the TA. Care must be taken to ensure the seed beam is well aligned to the input of the TA. An aspheric lens must be used to focus the seed beam onto the TA, and the polarisation of the seed beam must also be considered as the coupling efficiency of the TA depends on the polarisation of the seed. Collimating the TA output requires both an aspheric and a cylindrical lens, as the divergence of the output is different on the y - axis compared to the x - axis.

There are three methods used in our experiments for laser locking: Doppler free spectroscopy locking, Dichroic Atomic Vapour Laser Locking (DAVLL) and offset laser locking. We will discuss each of these in turn.

3.1.1 Doppler free spectroscopy locking

Doppler free spectroscopy locking, also called saturated absorption spectroscopy locking [37, 38], is in many ways the standard method for laser frequeny stabilisation, and in general is the go to method for cold atom experiments [39–43]. For this method, the laser is passed through a vapour cell and then retro-reflected back along the same path, before then hitting a photodiode. Figure 3.1 demonstrates the optical setup. The current to the laser diode is modulated with a frequency of approximately 100 kHz, so that the frequency of the laser rapidly oscillates [44]. As the vapour cell is at room temperature, there are a large range of atom velocities along the path of the beam. When the laser first passes through the vapour cell, the intensity would be reduced as light is absorbed by the atoms which are Doppler shifted to a resonant frequency. As the laser oscillates, the number of atoms which have been Doppler shifted to the resonant frequency changes, and so the amount of absorption, and thus the decrease in intensity, changes according to the thermal distribution of the atoms. By triggering an oscilloscope off the current applied to the laser, we can measure the intensity of the laser on the photo diode against the laser frequency.

When the beam is retro-reflected back along the same path, then the relative Doppler shift changes sign. This means that the laser will again be absorbed by atoms Doppler shifted to the correct frequency, and so the intensity will again be reduced. This creates the Doppler valley seen on the photodiode. The exception will be from atoms which are travelling perpendicular to the laser beam, and so are not Doppler shifted at all. These atoms will absorb the light which is resonant to the non-Doppler shifted transition frequencies. When the beam is retro-reflected, these atoms are already excited by the first beam, and so cannot absorb the retro-reflected beam, leading to no loss in intensity. This is seen on the oscilloscope as a peak in the Doppler valley at the resonant frequencies. If the atom velocity is such that the Doppler shift is exactly halfway between the energy states of the upper manifold of the hyperfine structure, then a laser with a frequency corresponding to this halfway point can be absorbed by atoms

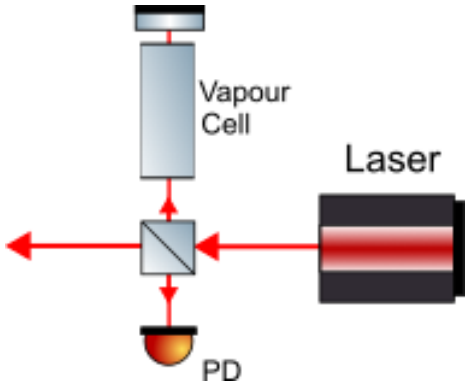

Figure 3.1: Setup for Doppler free spectroscopy used in laser locking.

with either positive or negative of this velocity. Retro-reflected light which has the opposite Doppler shifted frequency is thus not attenuated. This creates a 'crossover peak' in the spectroscopy signal. These peaks are generally higher than on resonant peaks because they involve two separate velocity classes of atoms, depending on which frequency is directly incident and which is retro-reflected. Thus, twice the amount of light is absorped by the atoms and so the peak appears much larger.

We can extract the spectroscopy signal by modulating the laser current with some frequency ω_1. By multiplying the photodiode output by a sin wave of frequency ω_1 and integrating the result, the desired error signal is extracted by relying on the fact that as time T tends to infinity, then

$$f = \int_0^T A\sin(\omega_1 t) \times B\sin(\omega_2 t)\, dx \tag{3.1}$$

approaches zero unless $\omega_1 = \omega_2$. In this case, the lock in amplifier will return a signal proportional to the derivative of the input, called the error signal. This is important because when the laser is on resonance there is a peak in the spectroscopy, and so the derivative is zero. We thus wish to provide feedback to the laser such that this signal is as close to zero as possible. We can do this with a Proportional Integral (PI) card, which for a given input signal $x(t)$ returns a signal

$$y(t) = A \times x(t) + B \times \int_0^t x(\tau) d\tau. \tag{3.2}$$

This is a simpler version of the more standard PID feedback, which also includes a derivative term. A and B are constants that can be tuned by adjusting potentiometers on the PI card. The first term provides the main feedback, by setting A to some negative number. This feedback to the laser will thus act to push x back towards zero. Setting A too high will create oscillations, so typically A is tuned until just below that point. The integral term prevents

a systematic offset by forcing the central frequency to the right value. Thus, a stable feedback to the laser is created, which corrects for any drift in laser frequency.

This feedback system does not account for the response of the laser itself, i.e. it does not consider the impulse response function of the system. This is simply the measured change in the photodiode signal from a delta pulse sent to the laser, and so will depend on the laser as well as the spectroscopy system used to generate the signal. Whilst this allows the feedback system to be used generally regardless of specifics of the spectroscopy system, a more stable feedback signal could be generated by including the impulse response function. Usually, however, the system we have described is sufficient for the frequency stability required.

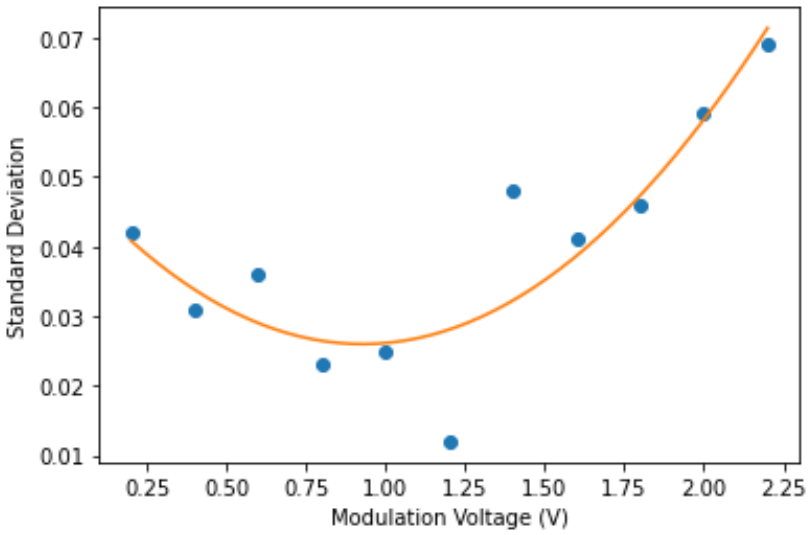

Figure 3.2: Standard deviation of 30 repeated absorption measurements through the fibre, plotted against modulation amplitude of the Cs repumper. The data is fit to a quadratic line of best fit (yellow) which gives an optimal voltage of approximately 0.93V.

We can further improve the stability of the lasers by optimising the modulation of the lasers locked using Doppler free spectroscopy. To do this, we need some independent way of measuring the laser frequency stability. In later sections we will discuss how to measure the Allan deviation of the error signal, which is one method of measuring laser stability. Another method is to consider the standard deviation of repeated absorption measurements, either in free space or through a fibre. We can then adjust the amplitude or frequency of the modulation signal and measure the resulting change in frequency stability. As an example, Figure 3.2 is a graph of the standard deviation for absorption measurements through the fibre against the amplitude of current modulation for

the repumper laser in the EIT experiment, which we will discuss in more detail in section 4.4. We can thus use this method to find the optimal modulation amplitude and frequency for all the lasers locked using this method.

3.1.2 DAVLL

An alternative to Doppler free spectroscopy locking is to use Dichroic Atomic Vapour Laser Locking (DAVLL). DAVLL takes advantage of the fact that a magnetic field will split the energy levels of the atomic vapour due to the Zeeman effect [45]. When linearly polarised light passes through the cell, the left and right circularly polarised components will have their respective Doppler valleys shifted in opposite directions. Using a polarising beam splitter to separate these signals, a simple subtraction circuit can convert these shifted Doppler valleys into a signal with a sharp slope in the centre of the valley, as shown in Figure 3.3.

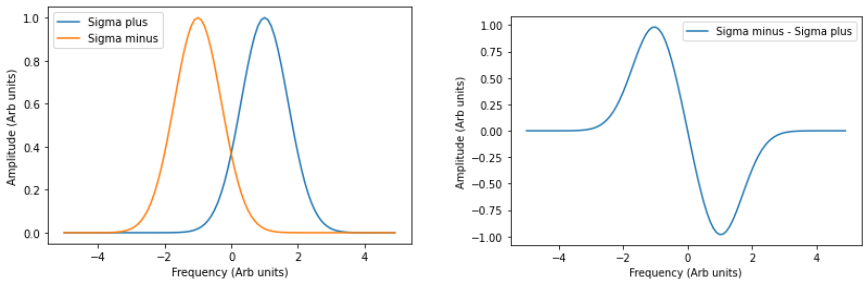

Figure 3.3: The splitting of the Doppler valley due to the Zeeman effect, and how the difference provides a useful locking slope. A linear polariser ensures that light passing through the vapour cell has only linearly polarised components.

Neodymium magnets are used to generate the strong magnetic field needed, and their position and angle relative to the vapour cell can be adjusted to optimise the DAVLL signal. This signal can then be passed to a PI controller to lock the laser as with Doppler free spectroscopy locking. The setup for DAVLL laser stabilisation is shown in Figure 3.4. Note here we are using the Doppler valley and not the sub-Doppler features to lock. In general, the slope will not be as sharp as for Doppler free spectroscopy, but will extend over a larger frequency range. As such, it is particularly useful for the Rb repumper, as the Doppler free signal for this transition is weak, and so long as there is sufficient repumper power ($\approx$ 10mW), then the MOT cloud is less dependant on the frequency of the repumper. This type of locking is used to lock the repumper is the multi-frequency MOT experiment. See section 5 for further details.

3.1.3 Offset laser locking

In some cases we wish to have fine control over the frequency of a laser, or be able to adjust it whilst the control sequence is running. This is because in the

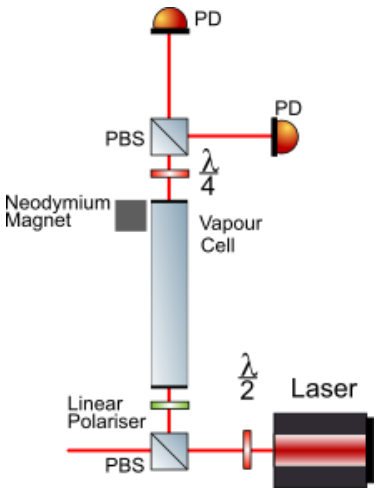

Figure 3.4: A simplified diagram of a DAVLL setup. The two photodiodes measure either the sigma minus or sigma plus component. The locking signal can then be derived by simply subtracting the signal of one photodiode from the other.

chamber the exact resonant frequency can change, for example, by changing the magnetic offset fields. We also want to measure the linewidth of the absorption to ensure there aren't any sources of linewdith broadening, and when we take EIT data, we will want to scan the frequencies of the control and signal lasers independently. In other cases, we want to take advantage of crossover peaks on the spectroscopy signal, which in general are more prominent than the peaks of 'pure' transitions. In these cases, we instead use offset laser locking, also called beatlocking.

Beatlocking involves locking a given laser to a reference laser, which is usually locked using Doppler-free spectroscopy to the desired transition. The two lasers are spatially overlapped, and wave plates are used to ensure they are both linearly polarised along the same axis. Additionally, the beam powers are adjusted so that they are as close as practical.

As they are spatially overlapped and linearly polarised along the same axis, there will be strong interference between the two lasers. For reference frequency ω_1 and main laser frequency ω_2, interference will give a wave with two frequencies $\delta\omega = \omega_1 - \omega_2$ and $\omega_1 + \omega_2$. As the interference will not be perfect, there will still be some light at the original frequencies.

Assuming that $\omega_1 \approx \omega_2$, then $\delta\omega$ (order MHz) will be much smaller than any of the other frequencies (order THz). The photodiode response rate is too slow to read the larger frequencies, so only $\delta\omega$ is measured. This signal from the photodiode is mixed with one from a Voltage Controlled Oscillator (VCO), which outputs a signal whose frequency, ω_{VCO} is finely controlled by the input voltage. As before, the resulting signal has a mix of frequencies. A low pass

filter ensures only the lowest frequency, $\Delta\omega = \delta\omega - \omega_{VCO}$, can pass. This signal is then split through an interfereometer, which induces a time delay τ and thus creates a phase difference $\Delta\omega\tau$. When combined and again sent through a low-pass filter, the resulting signal can be used to create an error signal that is proportional to the phase difference. This signal is passed to a PI card which feeds back to the main laser so that this phase difference is kept constant. When the VCO is adjusted, the feedback to the main laser forces the frequency ω_2 to shift in response. This allows for very fine control of the laser frequency.

It is important to note that the VCO can only accept 0 or positive voltages as inputs, not negative ones. This means we can only push the frequency in one direction compared to the frequency of the reference laser. Thus, we lock the beat signal with the VCO in the centre of its frequency range, wich allows us to shift the laser frequency in both directions.

3.1.4 Polarisation Stability

We have discussed during the theory section how the cooling and trapping of the atoms require the correct polarisation. As such, we use polarisation maintaining fibres to transport light from the preparation area to the MOT chamber. This also ensures that any drift in alignment by the spectroscopy setup will not impact the alignment of the MOT beams or imaging beam. The fibres are only polarisation maintaining for two orthogonal linear polarisations, and so we need to ensure the in going polarisation is correct. A quarter waveplate placed after the fibres is sufficient to create the circularly polarised light needed for the MOT. The waveplates need to be rotated to ensure the correct polarisation is acquired, but this is fairly straightforward.

To maintain polarisation through the fibre, we place a quarter waveplate and a half waveplate just before the fibre, with the half wave plate closer to the fibre. It is important that no other optics are between these waveplates and the fibre in coupler, as they will introduce some small polarisation offset that experience has shown is hard to account for. The output of the fibre is sent to a polarisation analyser. By stressing the fibre, either mechanically or by applying a temperature gradient, the drift in polarisation becomes apparent. When stressing the fibre, care must be taken not to damage it. By adjusting the preceding waveplates, the oscillation in polarisation can be minimised. The waveplates are then locked in position to prevent further drifts. Experience has shown that some actions, such as adjusting the power balance of beams using a half waveplate and polarising beam splitter further up the beam path, can introduce polarisation drifts even though the polarising beam cube should prevent such drifts. It is assumed that these cubes do not behave ideally, leading to such behaviour. The waveplates for maintaining polarisation through the fibre thus need to be placed as close to the fibre incoupler as possible.

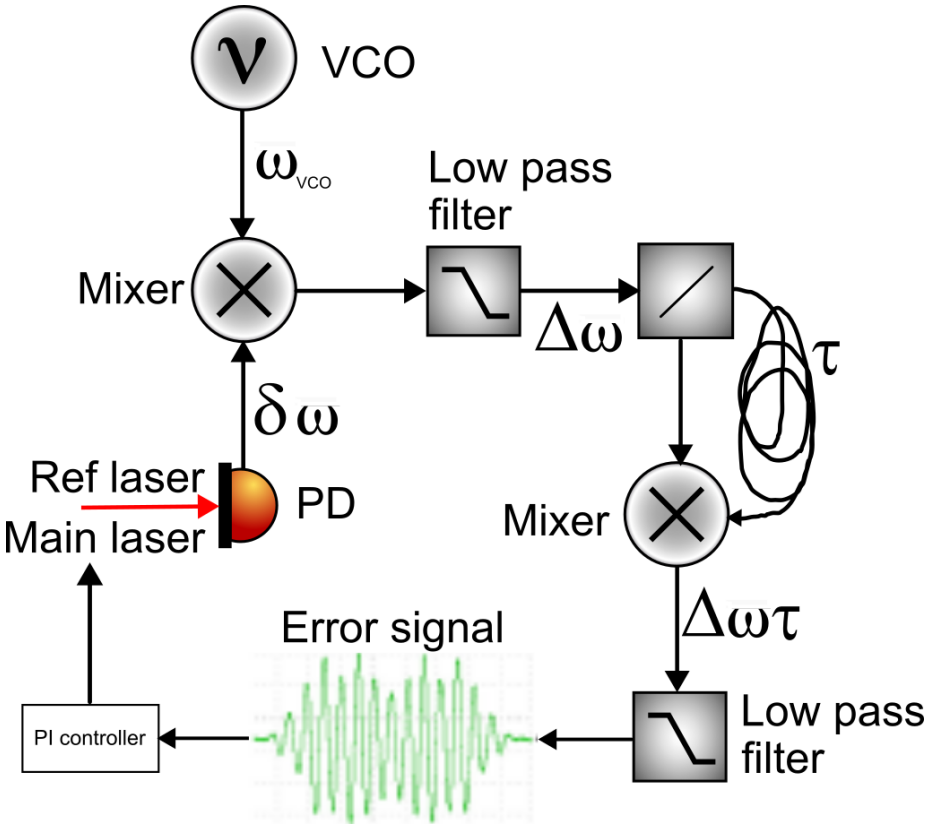

Figure 3.5: The reference and main lasers are overlapped, which creates an interference pattern. Only the frequency component $\delta\omega$ is passed to the mixer, where it combines with ω_{VCO} and then passed through a low pass filter, leaving $\Delta\omega$ as the only frequency component. The signal is then divided and part picks up a phase difference τ. When combined with the mixer, this creates an error signal proportional to $\Delta\omega\tau$. When the error signal is locked to the PI card, th feedback to the main laser ensures that $\Delta\omega\tau$ remains constant, so when ω_{VCO} is adjusted, the frequency of the main laser ω_2 shifts accordingly.

3.2 Absorption imaging

In general we wish to have a good idea of the quality of the atom trap in terms of atom number, density and temperature. There are a few different approaches to extracting this data, but a very common method is absorption imaging. In this process, the cooler beams are switched off and a pulse of resonant light is applied to the MOT, with the expectation that the atom cloud will attenuate the beam. As the shutters take a finite time to close, there is a small time delay between the MOT beams turning off and the first image being taken. This is called the fall time. The result is then measured on a CCD camera. By sending a second beam approximately 0.1 s after the first, the MOT will have been dispersed by absence of the cooler light and so the beam will not be attenuated. By comparing the first and second images, details about the atom cloud can be derived. In general, a third image with no imaging beam is taken to remove any background light from the processed image. Whilst this allows for much information about the atom cloud to be attained, it is a destructive process. In general this is not a problem, however, as the whole process of MOT formation and imaging takes less than 10 seconds. It is rare we require a data rate faster than this.

The atom number of the MOT can be found using the equation shown here [30, 46]

$$N_{atom} = \int -\frac{1}{\sigma_0} ln \frac{I(x,y)}{I_o(x,y)} dxdy, \tag{3.3}$$

where σ_0 is atomic absorption cross section, and I and I_o are the transmitted and initial intensities. The background image is subtracted from both the MOT and no MOT images before the ratio is taken. There are two methods to calculate I and I_o from the raw images. Either the ratio can be done pixel by pixel, with the integral becoming a sum over all the pixels, or the raw images can be fitted to a 2D Gaussian to estimate I and I_o. Once N_{atom} has been found, the density can then be easily found using the atom number and cloud size.

3.3 Temperature measurements

The temperature can be measured using time-of-flight imaging, where the dynamics of the MOT after the cooler beam has been switched off can be used to derive the temperature of the atom cloud. In practise, because the imaging beam is destructive, the experiment is simply repeated for different fall times. As the atom cloud is different for each experiment, repeats are taken for each fall time and an average is taken. This can make temperature measurements more time consuming to make. In general for MOT optimisation, it is the atom number and density that are used.

A simplified model used here to estimate the temperature assumes that the atom cloud remains Gaussian after it is released, and that collisions and

gravity do not affect the shape of the cloud as it expands. Modelling the trap as harmonic with frequency ω, then once the time-of-flight measurements are taken, the variance $\sigma(t)^2$ in the distribution of the atom cloud can be fitted to a quadratic in time t [30, 46]:

$$\sigma(t)^2 = \frac{k_B T}{m} t^2 + \frac{k_B T}{m\omega^2} \tag{3.4}$$

to obtain an estimate of the temperature of the original cloud. This can be shown more clearly in Figure 3.6. The x and y axes are each fitted to a 1D Gaussian, and the standard deviation is plotted for each as a function of time. This can then be fitted to the above equation to find the temperature. This results in each axis producing a different temperature, as shown in Figure 3.6.

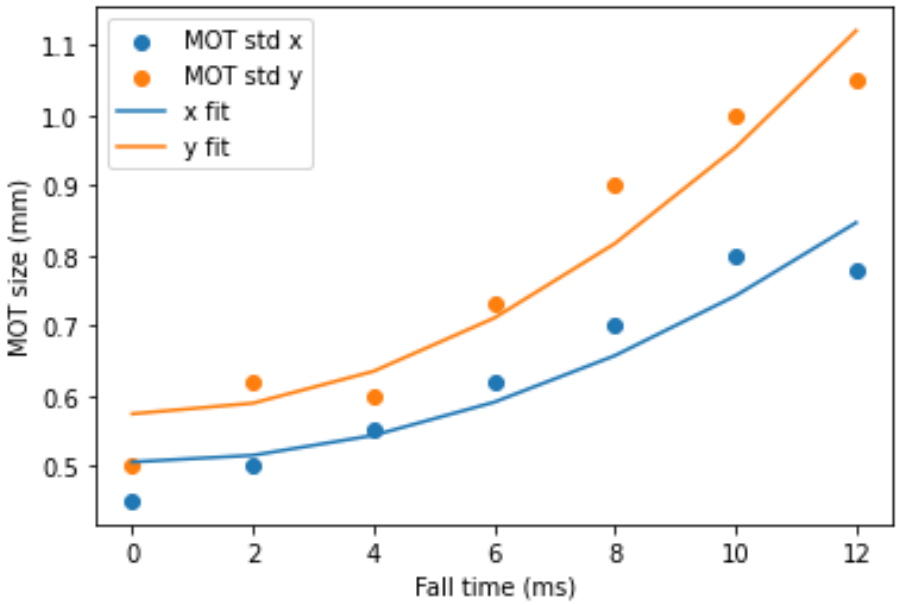

Figure 3.6: Temperature measurement based on time of flight data. The measured std on the x and y axis are fitted to equation 3.4. We find $T_x = 37.9 \pm 6.4 \mu$K and $T_y = 60.7 \pm 8.0 \mu$ K.

Chapter 4

EIT in a waveguide chip

Of considerable interest in recent years has been the development of quantum computing [4], for applications in cryptography [7], database sorting [6], simulation of quantum systems, and others. There are multiple ways to achieve a quantum computer, perhaps the most investigated being using a Rydberg atom array [18]. Our approach involves demonstrating Electromagnetically Induced Transparency (EIT) in a waveguide chip. EIT is the phenomena where the relative absorption of an on resonance beam (called the probe or signal beam) by an atom cloud is controlled by the frequency of a second incident beam (called the control beam). This phenomenon also increases the refractive index of the atom cloud, reducing the group velocity of photons from the probe beam. The theoretical details were discussed in section 2.6.

Previous experiments have used EIT in metamaterials [11], Rydberg atom [12], nanofibres [10] and other systems [13], but our approach instead uses a laser drilled fibre inside a vacuum chamber. The hole itself is shown in Figure 4.4. This hole is perpendicular to the fibre, and caesium atoms are held in a dipole trap loaded from a MOT. This method allows for the photons to be well focused onto a cloud of ultra cold atoms, maximising the coupling efficiency between the atoms and the photons.

This experiment has been continued on from work from previous PhD students, and so can be considered a follow on to [30, 47]. Previous experimental work was on lithium - caesium mixtures [46, 48, 49], before the current experiment on EIT. Given the long history of the experiment, there are many systems carried over, in particular the control system. The principal difference in the setup from [30] is that the chamber has been flipped by 90^o, so that the dipole trap points horizontally into the fibre, rather than vertically upwards. Because of this, the z-axis is on the horizontal axis instead of the vertical axis.

The experiment has been developed under the ErBeStA project, and so is referenced as the ErBeStA experiment. This consists of a vacuum chamber with a bare fibre stripped and attached to a glass plate, which is then suspended inside the vacuum chamber, which is shown in a sketch in Figure 4.1. A MOT of approximately 10^8 Cs atoms is formed close to the fibre, and then a dipole trap

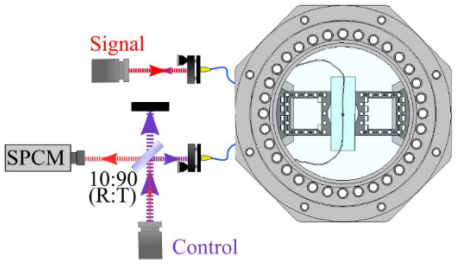

Figure 4.1: Sketch of the wave–guide in the vacuum chamber, with a control and signal beam coupled to the fibre and a SPCM to measure the transmission ratio.

is used to move atoms from the MOT to the hole in the fibre. Light pulses sent down this fibre can then be used to demonstrate EIT in the fibre. To detect these light pulses, a Single Photon Counter Module (SPCM) is on the other side of the fibre. This is shown in Figure 4.2. We would also like to be able to measure the group velocity of the photons inside the atom cloud, which should be much smaller than the speed of light in a vacuum as discussed in section 2.6. To do this, we would need to measure the delay on the SPCM which may only be a few tens of nanoseconds. Shutters are used to control the cooler and repumper timings, whilst AOMs are used as fast switches for imaging, as well as the probe and control beams.

4.1 Experimental Overview

The experiment requires precise timings and control for a variety of parameters such as shutter timings, laser frequencies and magnetic field gradients. This control system is provided by a National Instruments PXIe-8130 controller, which provides 32 digital channels and 12 analog channels. We also use a field programmable gate array to provide a common clock to be used by the control system. The software control system was principally developed by Matthew Jones [49] and Asaf Paris-Mandoki [46]. The digital channels are used to control shutters and Acusto Optical Modulator (AOM) switches, as well as to trigger the cameras and SPCM. The analog channels are used to ramp magnetic fields and control the VCOs for beatlocked lasers.

We have a pair of coils in the anti-Helmholtz configuration which each provide a magnetic field gradient of 10G/cm in the centre of the chamber, which is required to form a MOT as detailed in section 2.3. Additionally, the system includes 3 pairs of offset coils, 1 pair for each axis. These are used to move the MOT around the vacuum chamber to ensure its position with regards to the hole in the fibre is optimal. Details, including simulations of magnetic field strength, can be found in [30]. However, care must be taken because, as mentioned before, the chamber has since been rotated. As such, that work mentions

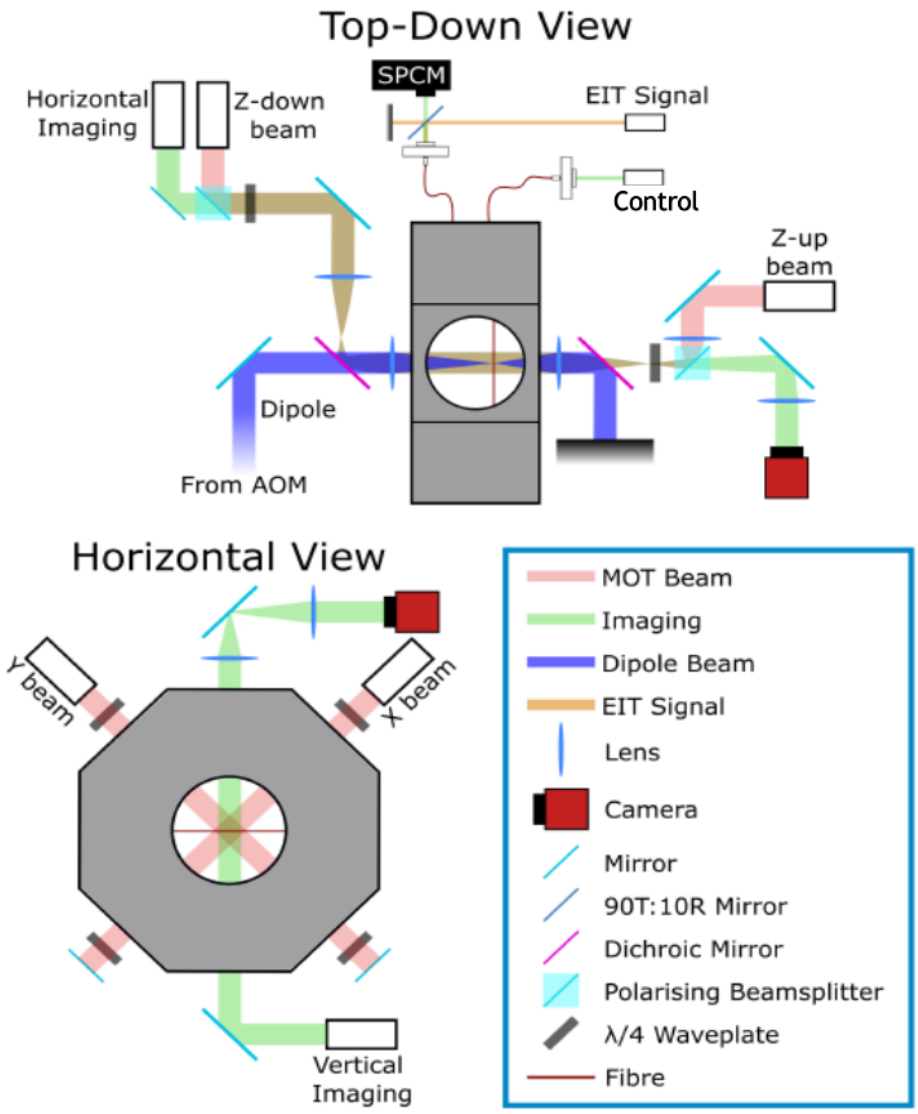

Figure 4.2: The experimental setup of the ErBeStA experiment. The MOT beams (red) trap and cool caesium atoms, before the dipole beam (blue) moves the atoms into the fibre (red line). The EIT signal and control beams are then passed through the fibre and an SPCM is used to measure the transmission ratio. Figure made by Matt Overton.

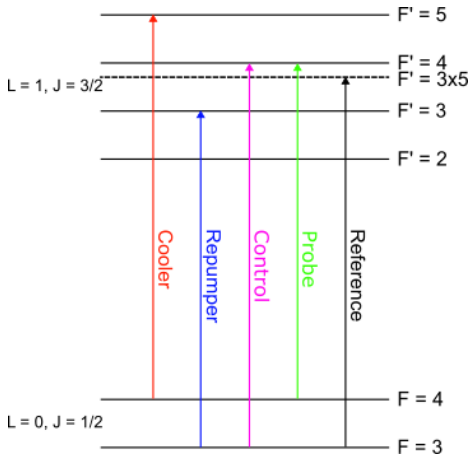

Figure 4.3: Hyperfine structure of ^{133}Cs and the relevant transitions. The cooler, control and probe beams are all beatlocked off the reference laser, which is locked using Doppler free spectroscopy.

the atom cloud being pushed vertically towards the fibre, which is now facing horizontally. Once the coils have moved the atom cloud to the optimal position, the cooler beams then need re-aligning to increase the atom number of the MOT at the new position. It is common that there is a trade off in position, in that the closer the MOT is to the fibre, the worse the MOT becomes. This is attributed to the glass plate scattering light from one of the z axis MOT beams, thus reducing the size of the MOT. The vacuum in the chamber is maintained using an ion pump, which maintains a background pressure of 8×10^{-11} mbar and a pressure of 1.1×10^{-10} mbar with the dispensers on. The caesium dispensers release caesium into the chamber when a current is applied. The more current is applied, the more caesium is released, and thus the shorter the lifetime of the dispensers. We typically supply a current of 3.5 A to the dispensers. Replacing them first requires bringing the chamber to room pressure. Afterwards, the vacuum chamber is then pumped out using a roughing pump and a turbo pumps, and the chamber is baked at approximately 150^oC for a week. Realigning all of the optics takes several more weeks, and during the process care must be taken to avoid damaging the waveguide. As this is a lengthy process, multiple dispensers are replaced a once, which means the dispensers last for several years before needing to be replaced.

As discussed in section 2.3, to create a MOT we require both cooler and repumper light. These are shown in red in Figure 4.2 and the relevant transitions are shown in Figure 4.3. We use the $F = 4 \rightarrow F' = 5$ transition as the cooler and the $F = 3 \rightarrow F' = 3$ transition for the repumper. Whilst the $F' = 5 \rightarrow F = 3$ transition is forbidden under standard selection rules, there is a small probability of a magnetic dipole transition, hence the repumper. The reference laser is locked to the $F = 3 \rightarrow F' = 4 \otimes 5$, whilst the repumper laser is locked to the

$F = 3 \rightarrow F' = 2 \otimes 4$ transition and then an AOM is used to shift the frequency to the correct transition. The cooler beam is beatlocked off the reference laser to shift it to the $(F = 4 \rightarrow F' = 5)$ transition.

To extract data from the experiment, absorption imaging is utilised, as detailed in section 3.2. We use absorption imaging on two different axes, shown in green in Figure 4.2. One is aligned vertically with a magnification of 2, and one is horizontal with a a magnification of 1.5, which is aligned with the dipole beam (blue in Figure 4.2) and one of the horizontal MOT beams (red). The horizontal imaging is used to align the MOT and dipole beam with the hole in the fibre, as shown in Figure 4.11, whilst the vertical imaging system demonstrates that atoms in the dipole trap reach the other side of the fibre when the dipole trap is well aligned, which can be seen in Figure 4.12. Utilising the horizontal imaging to ensure the dipole beam is well overlapped with the hole in the fibre, we can be sure that atoms are passing through the hole in the fibre. The vertical imaging can then confirm this. As the horizontal imaging beam is overlapped with one of the MOT beams, it is not possible to use fluorescence imaging on this imaging system.

A 30 W 1064 nm Nufern tapered amplifier, which is blue in Figure 4.2, is used to form a dipole trap which moves atoms from the MOT to the hole in the fibre. As the beam is far detuned from any atomic transitions, there is no need for frequency stabilisation as required for the other lasers. A 75 mm lens focuses the beam to a 12 μm waist, giving a Rayleigh length of 425 μm. The lens is placed on a translation stage for fine tuning of the focal point. A dichroic mirror is used to overlap the dipole beam with one of the MOT beams.

The waveguide consists of a standard Thorlabs single mode fibre with a laser drilled hole perpendicular to the fibre. Previous work has focused on optimising the shape of the hole, using simulation and experimental testing [30]. This experiment benefits from that work, and the optimal shape was found to be an 'hour glass' shape, where the sides where the light will propagate through curves towards the hole. The new and old fibres are shown in Figure 4.4. This shape helps focus light from the fibre onto the atom cloud and also increases the transmission efficiency compared to the cylindrical shape. This hole obviously reduces the maximum transmission efficiency possible through the fibre, which is empirically found to be 15 percent. Prior to drilling the hole [30], the fibre was stripped of the cladding in the middle, which is not vacuum compatible, and mounted to a glass slide using vacuum compatible UV epoxy. To prevent the glass slide from interfering with the MOT beams, a hole with diameter of 10mm was removed where the fibre is mounted. The glass plate is then suspended inside the chamber.

As discussed in the theory section, EIT is a three – level system requiring two different resonant frequencies. The probe and control beams are aligned anti-parallel through the fibre, as this allows the probe beam to be separated from the control using a 90:10 splitter. The probe beam is then incident on a Single Photon Counter Module (SPCM). The reason for using a SPCM is due to the beam powers involved. The hole is only 30 micrometers across, and so we expect only a few hundred atoms to be trapped in the interaction region at once.

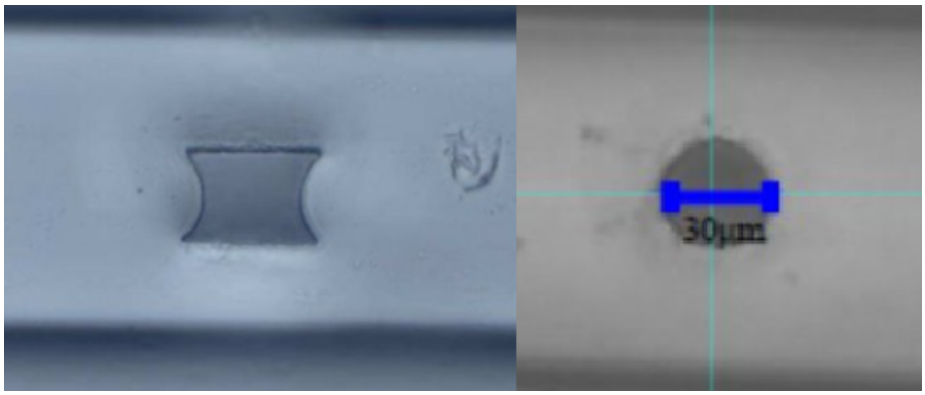

Figure 4.4: Left: New fibre using the 'hour glass' shape. Right: old fibre using a cylindrical shape.

To avoid saturating the atoms, the probe beam is roughly 2 picowatts. This requires using a SPCM to accurately detect these extremely small powers and to show EIT in the fibre. The probe beam is stabilised to the $F = 4 \rightarrow F' = 4$ transition and the control is resonant to the $F = 3 \rightarrow F' = 4$ transition. During my work on the experiment, the probe was beatlock off the reference laser, and we used a different reference laser, stabilised to the $F = 3 \rightarrow F' = 4$ transition, to beatlock the control. Currently, these lasers are both beatlocked off the reference laser, as this ensures the probe and control beams are phase locked relative to each other.

A significant problem encountered for demonstrating EIT in the waveguide chip is that the optimisation process is complex with many parameters. This is further complicated by the fact that it can not be broken down into smaller steps that can be optimised individually. The beam alignments and other parameters which produce the highest density MOT will not necessarily provide the highest density dipole trap, and the highest density dipole trap will not necessarily provide the most number of atoms trapped in the fibre.

4.2 MOT formation

Forming a MOT inside the chamber is complicated by the presence of the waveguide chip. The fibre partially obscures one of the MOT beam axes, and so instead of using a retro-reflective mirror, we use two separate beams and adjust the power balance between them. This also allows us to adjust the position of the MOT relative to the chip, by also adjusting the alignment of the other MOT beams and the offset coils. This becomes important when trying to optimise the number of atoms trapped inside the fibre.

To get the timings of the shutters correct, we used photodiodes connected to an oscilloscope to ensure the MOT beams turned on and off again together. For

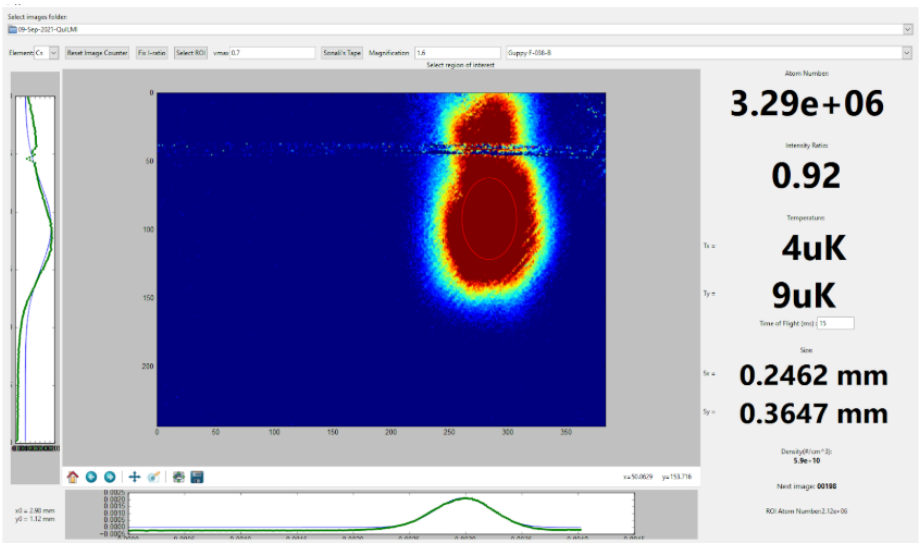

Figure 4.5: MOT aligned close to the hole in the fibre.[1]

the dipole trap to move atoms from the MOT to the hole in the fibre, we need to ensure the MOT was over the hole. Figure 4.5 shows the MOT formed close to the fibre, viewed using the horizontal imaging system. The core of the fibre is also visible. The vertical imaging is used to ensure atoms are clearly passing through the hole in the fibre, as the MOT is generally loaded so far away from the fibre that it is outside the field of view of the vertical imaging system.

Initially, we will use the $F = 4 \rightarrow F' = 5$ transition for fibre absorption measurements, as the transition is stronger. To demonstrate this, Figure 4.6 shows the MOT imaged with the imaging beam on the $F = 4 \rightarrow F' = 4$ transition. The difference in interaction strength is clear, which is why we start with the stronger $F = 4 \rightarrow F' = 5$ transition.

In order to maximise the number of atoms in the hole, we need to consider the MOT size, density and position, as well as considering the dipole beam and its alignment to the hole in the fibre. The process involves adjusting the MOT loading parameters such as cooler frequency, MOT beam alignment and coil current to find the 'best' MOT. This requires ensuring the MOT has a good atom number ($\approx 10^7$), good density ($\approx 10^{10}$ atoms/cm^3) and low temperature ($< 100\mu K$), whilst also overlapped with the hole in the fibre and formed ≈ 1 cm from the waveguide. An optimal MOT is shown in Figure 4.7. To increase the atom density, after loading the MOT the cooler beams are detuned by 15

[1]The red oval shows the fitting region. For scale, the fibre itself is 100 μm across. The graphs on the bottom and left hand side show the fitting on each axis. On the right is the atom number, intensity ratio ($\frac{I(x,y)}{I_o(x,y)}$ in the fitted region), temperature measurements and std on the fitted Gaussian. The temperature measurements here should be ignored, as they are derived from only a single fall time instead of a time of flight measurement.

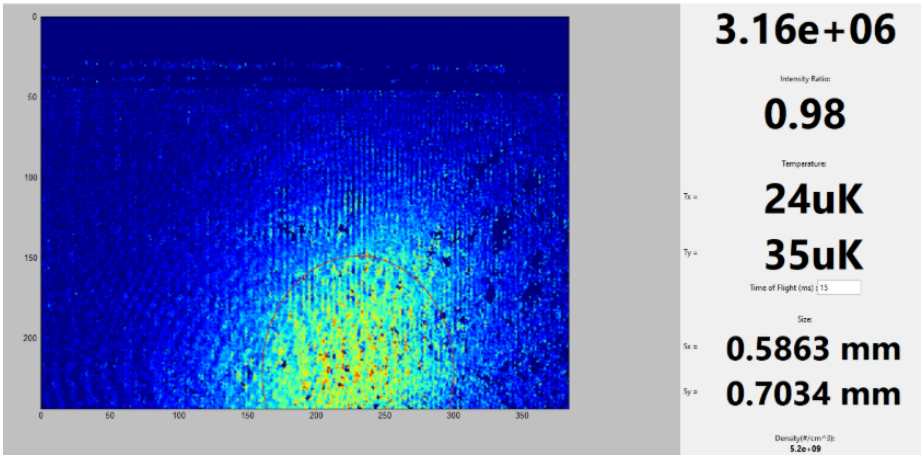

Figure 4.6: MOT viewed on the $F = 4 \rightarrow F' = 4$ transition, as seen on the vertical imaging.[1]

MHz to reduce light induced collisional losses. Again there is a trade off in how long this process lasts between atom number and atom density. Typically, this cooling process lasts for about 20μs before the dipole beam is switched on.

A significant improvement came when we noted that the dispensers had nearly run out, requiring a replacement. Running the dispensers at a higher current significantly improves atom number, but also reduces the lifetime of the dispensers. A MOT this large does cause difficulties with temperature measurements, as the field of view is too small to see the expanding MOT after a certain fall time. As the vertical imaging cannot see the MOT, and the horizontal imaging is overlapped with the dipole beam and one of the MOT beams, altering the imaging system to correct this would be a lengthy process. Such large MOT compared to the field of view can lead to weird temperature measurements as shown in Figure 4.8. The measured standard deviations plateau after roughly 7ms because the field of view is too small to see the MOT cloud expanding after this point. This leads to poor fitting to the expected expansion rate, given by Equation 3.4, and so an incorrect temperature measurement. This can be partially compensated by reducing the MOT load time or dispenser current when taking temperature measurements, which is easier than changing the magnification of the imaging system. This does mean, however, the temperature measurements refer to a deliberately smaller MOT than the one we actually use. More details on how the temperature of a MOT is measured using time-of-flight measurements are given in section 3.3. Overall, though, having too large a MOT is a nice problem to have.

The vertical imaging cannot be used for time of flight temperature measurements, as when released the atom cloud would fall out of focus of the imaging system. Instead, the vertical imaging is used to ensure that the dipole beam is well aligned to the hole by observing atoms on the other side of the fibre. This

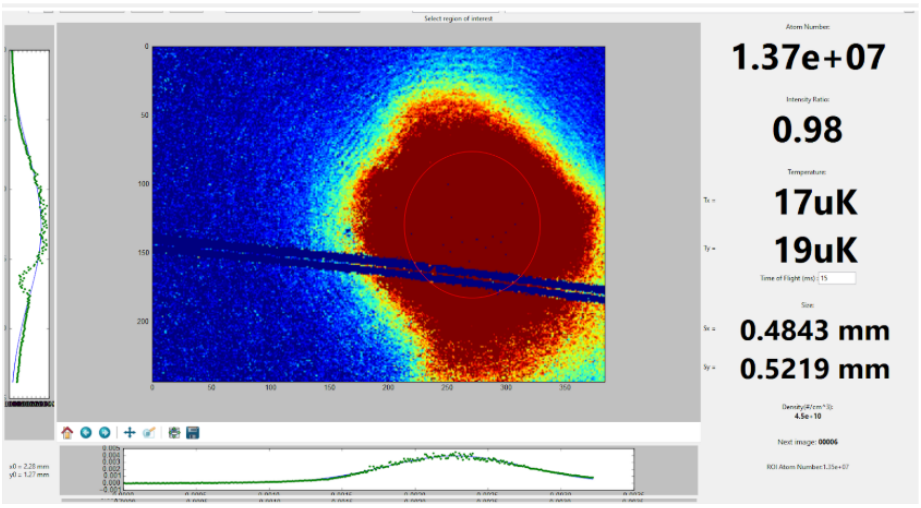

Figure 4.7: A larger, optimal MOT close to the fibre hole.[1]

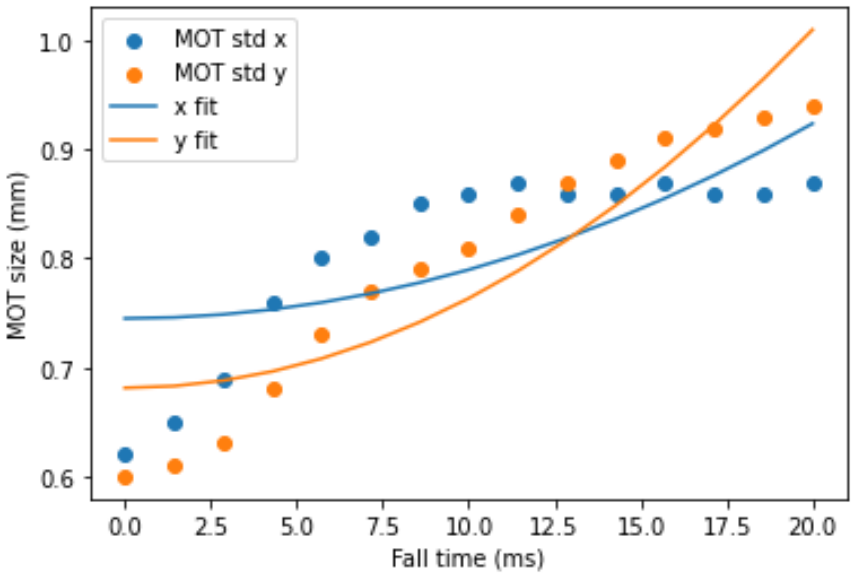

Figure 4.8: A temperature measurement of a large MOT. The field of view is too small to see the MOT expansion properly, leading to a poor fit. The temperature measurement given is thus unreliable. The CCD used is a Guppy F-038-B. This has an asymmetry in pixel number on each axis (384 x 244), which explains the different height for each plateau.

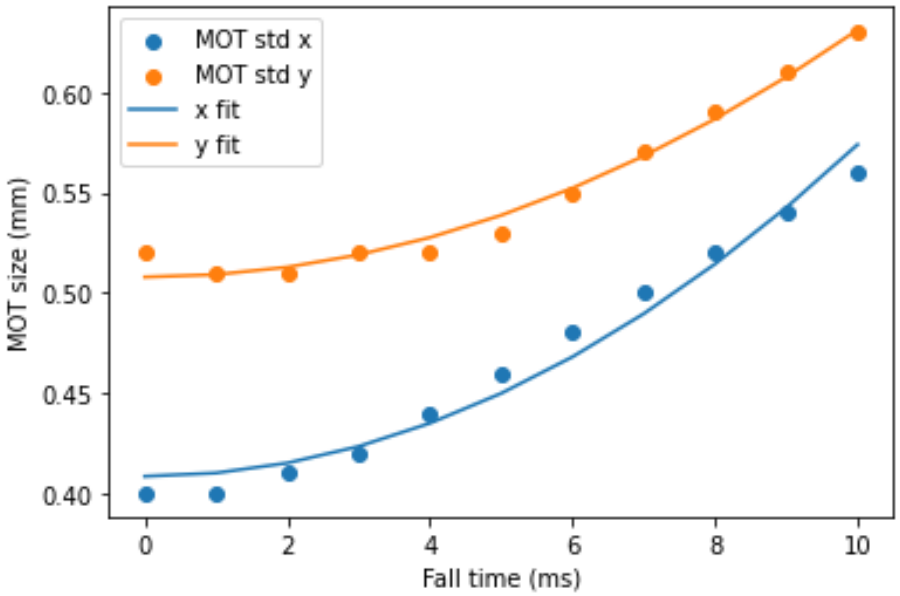

Figure 4.9: The expansion of the MOT cloud with fall time fits well to the expected curve given by equation 3.4, giving confidence in the temperature measurement. $T_x = 26.4 \pm 1.4\mu K$ and $T_y = 19.7 \pm 0.9\mu K$.

will be discussed in more detail in the following sections.

After considerable optimisation, we have reached a MOT temperature of $< 25\mu K$, shown in Figure 4.9. With the MOT now optimised, the atoms can be transferred to the dipole trap.

4.3 Dipole Trap

To transfer atoms from the MOT to the hole in the fibre, we use a dipole trap. By gradually reducing the trap depth of the dipole trap, we can simultaneously evaporatively cool the atoms. We also want to use the offset coils to compress the MOT and improve the efficiency at which atom are loaded into the dipole trap. In order to do this, after forming the MOT, we ramp the horizontal coils to push the atom cloud towards the waveguide chip. Simultaneously, we use a 30W 1064nm laser to capture the atoms in a dipole trap. This prevents the atoms from moving radially, and instead the atoms are drawn towards the focus point of the dipole trap. The focus of this laser is adjusted to where the hole in the fibre is, by using a 75mm lens mounted on a translation stage. After 40μs of loading time for the dipole trap, the cooler beams are detuned off resonance to allow the atoms to leave the MOT region and because the MOT light stimulates collisional losses in the dipole trap. More details on dipole traps can be found

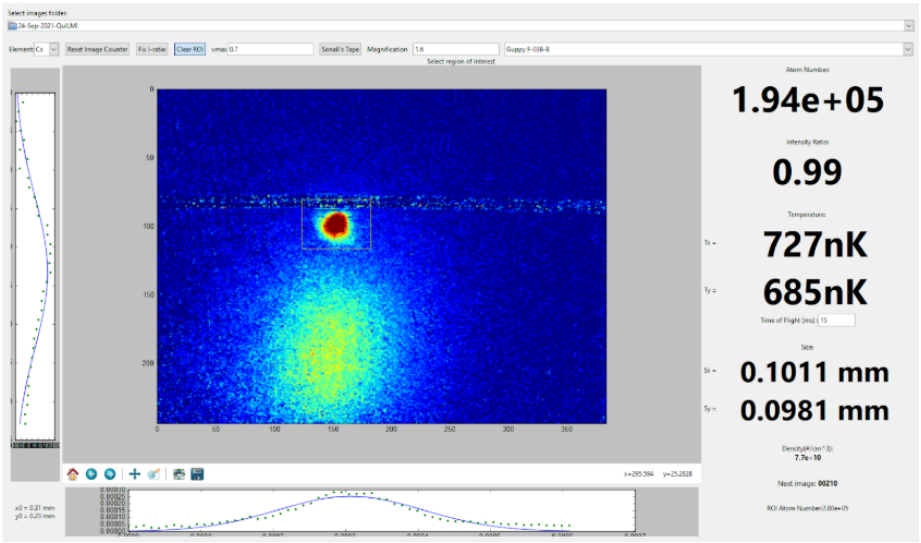

Figure 4.10: The dipole trap is formed below the fibre for easier imaging. The MOT beams have been detuned off resonance, so the MOT cloud can be seen falling due to gravity.[1]

in section 2.5. Evaporative cooling reduces the atom temperature further.

The beam waist is approximately $\omega = 50$ mm in diameter before the final $f = 75$ mm lens. The beam waist of the dipole trap itself is approximately 12 μm and has a Rayleigh length of 425 μm. This Rayleigh length is larger than the radius of the fibre, and there is no axial confinement except the dipole trap. As such, we expect atoms to oscillate in and out of the fibre along the beam depending on the trap depth and the temperature of the atoms.

To achieve fast on/off switching the beam is focused through an AOM, which is placed at the centre of a telescope. Care needs to be taken that the beam profile remains Gaussian, as this is key to the performance of the dipole trap. To prevent the AOM from overheating, a shutter is placed before the AOM. This shutter uses a mirror to reflect the beam into a copper beam dump when the dipole beam is not needed. The shutter only opens for less than a second when needed, and then the AOM can be used for fast switching.

Aligning the dipole beam is potentially challenging, as we need to ensure it is simultaneously well aligned to the MOT and the hole in the fibre. To ensure the dipole trap is well aligned, we can temporarily form the trap below the fibre so it is clearer on the camera, as shown in Figure 4.10.

When we have a dipole trap well aligned to the MOT and a density $\approx 10^{10}$ atoms/cm^3, we can then proceed to align it to the hole. This can be done by reducing the dipole beam power and looking directly at the beam on the camera, without forming a MOT. The hole causes a distinctive interference pattern on the beam, which is easier to see if the translation stage is temporarily adjusted

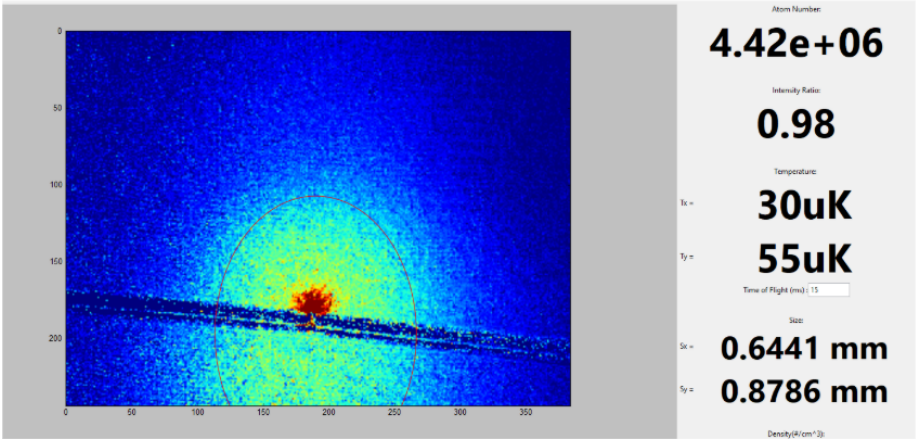

Figure 4.11: The dipole trap aligned with the hole in the fibre, as seen on the horizontal imaging.[1]

to make the beam appear bigger on the camera. The points at which the beam hit the sides of the hole are very apparent, and so we can place the beam in between the walls of the hole. Once we are satisfied it is aligned to the hole, the translation stage is adjusted to make the beam appear as small as possible, so that the dipole beam is focused at the fibre. The horizontal imaging of the dipole trap is shown in Figure 4.11.

We can then switch to the vertical imaging to ensure that atoms in the dipole trap have successfully been transported through the hole, as shown in Figure 4.12. Atoms can be seen on the other side of the fibre from the MOT, implying that the atoms have successfully traversed through the hole in the fibre. It is possible that atoms can go over or under the fibre as well, which would create a false positive. Another confirmation can be done by measuring the lifetime of the dipole trap when the beam is focused in the hole. When well aligned to the hole, the dipole trap is not disturbed and so there is no reduction in lifetime. By slightly adjusting the alignment of the dipole beam, the trap will then hit the fibre, significantly reducing the measure dipole trap lifetime. Care must be taken that the dipole beam is not impacting the fibre for too long, however, as the high powers can damage the inner surface of the hole which would then reduce the transmission efficiency through the fibre.

Ideally, we would like to be able to adjust the position of the focus of the dipole trap in sequence so that we can first form the dipole trap at the position of the MOT and then move the atoms towards the fibre. This however, would require either a fine controlled motor on the translation stage or using a lens with an adjustable focal length, so instead we tune the focusing using a manual translation stage in between data collection measurements to find the optimal point.

Once we are confident that atoms are entering the hole in the fibre, we can

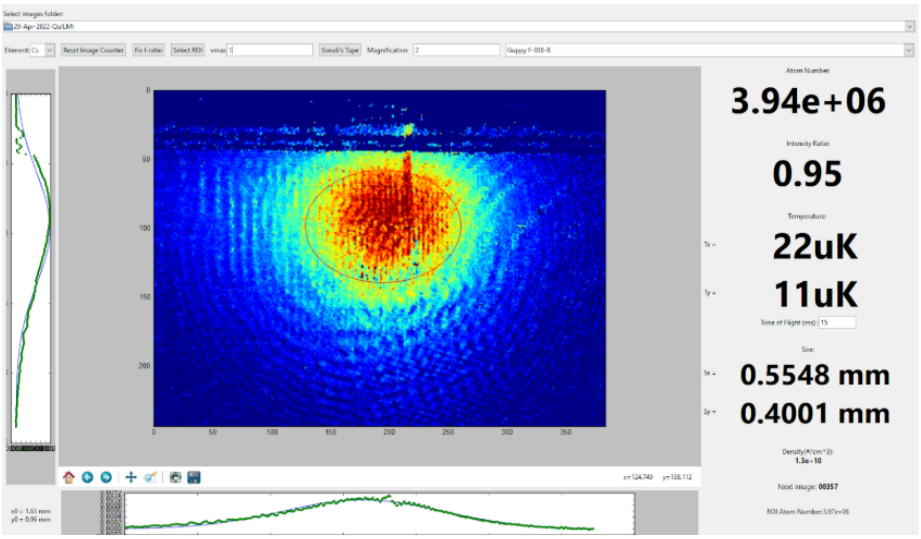

Figure 4.12: The dipole trap on the vertical camera. Atoms are clearly visible behind the fibre. Note that the offset coils have been ramped to push the atom cloud towards the fibre, which is why it is visible here.[1]

then re-optimise the MOT to further improve the dipole trap and the amount of atoms that get pushed into the hole in the fibre. There are many parameters that relate to optimising the dipole loading such as the position of the MOT and the ramping speed and timing of the offset coils. We have already mentioned the trade off involved in how close to the waveguide the MOT is formed. This trade off requires finding the best MOT for fibre absorption, and so once the MOT is roughly optimal, we need to retune all of the MOT parameters such as beam alignment. For optimal absorption through the fibre, care needs to be taken when optimising the z position of the MOT, such that the MOT is still well overlapped with the dipole trap. Any shift in the x or y axis would lead to a weaker dipole trap, which makes it difficult to find the optimal position along the z axis.

At this point, we need to ensure that atoms are in the hole by looking at absorption through the fibre. The interaction region in the waveguide, where light from the fibre are aligned to atom in the hole, is approximately $590\mu^3$. We can also see if the dipole trap is aligned through the hole by sending a light pulse through the fibre when taking an image. This would excite atoms inside the hole out of the trap, which makes it easier to see if atoms are in the hole. We also need to ensure no dipole light gets coupled into the fibre via the hole. Whilst the relative amount will be very small, the dipole beam is roughly 10^{13} times more powerful than the probe, so even a tiny relative amount will overwhelm the probe light. If the dipole beam hits the fibre, it will heat the fibre up, causing thermal photons to be released which will hit the SPCM. This could

also damage the fibre, reducing transmission. Previous work has considered using optical pumping of the atoms to the $F = 3$ state to reduce collisional losses whilst in the dipole trap. For further reading on this, see [30].

4.4 Fibre absorption

To check that atoms are successfully trapped in the hole, a 10-microsecond laser pulse of approximately 10 pW is sent through the fibre onto the SPCM. A binary counter is used to record the pulses out of the SPCM and return the total number of counts into an arduino. Initially, we use the $F = 4 \rightarrow F' = 5$ transition, as this is a stronger transition than the $F = 4 \rightarrow F' = 4$ transition that we will finally use for EIT. This is why we tested the relative strengths using the MOT in Figure 4.6. The dipole trap is then released, and another laser pulse is sent through 100ms after the first, well after all of the atoms have been dispersed. To remove background noise and other sources of light such as dipole light scatter, a laser line filter is placed before the SPCM to block out unwanted light. Significant amounts of physical shielding are placed, and counts with no laser beams on are measured to ensure this background light is removed. We then record a background measurement b of the experiment without probe light, and subtract this from the two measurements in each cycle. The ratio r between the atom a and no atom n shots can then be calculated as $r = \frac{n-b}{a-b}$. Another effect to be account for is bleaching of the SPCM, wherein the incoming rate of photons is higher than can be measured by the SPCM. To account for this, the transmission ratio is also measured with the coils off so that there are no atoms in the fibre. By dividing the transmission ratio by this factor, we ensure that any difference between the atom and no atom shots is due only to the atoms themselves. Due to the low number of photons used, there is significant photon shot noise, which follows a Poisson distribution with a signal to noise ratio proportional to the square root of the number of photons. As we cannot use higher powers without saturating the atoms, to improve the signal this process is repeated a number of times, usually 30 for testing and upto 100 for final data collection. The average of these shots is calculated, and this ratio can be used to estimate the number of atoms in the fibre. Usually a transmission ratio of 20 to 30 percent is expected for the $F = 4 \rightarrow F' = 5$ transmission, and a ratio of 50 percent for the $F = 4 \rightarrow F' = 5$. Ratios better than this have been measured, as the data shown in Figure 4.13 has an average transmission ratio of only 7 percent.

Once a transmission ratio through the fibre has been observed, we can again re-optimise a significant number of variables relating to MOT formation, coil ramping and the alignment of the dipole trap, this time in order to maximise the transmission ratio. We have already discussed needing to re-optimise the parameters for the dipole trap, and the parameters will also need to be adjusted to optimise the EIT signal once found. After considerable optimisation, the initial MOT is formed of roughly 10^8 atoms, approximately 10^5 atoms are loaded into the dipole trap, whilst on the order of 10^2 atoms are actually held in the

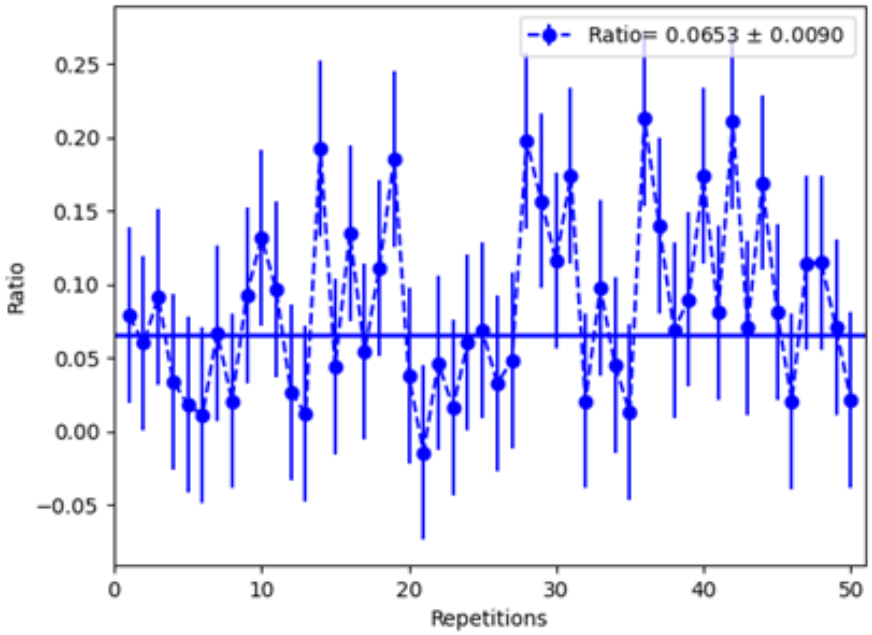

Figure 4.13: 50 different transmission ratios between atom and no atom shots, which average to $6.5 \pm 0.9\%$.

waveguide, owing to the small volume of the hole in the fibre. Evaporative cooling accounts for a considerable amount of this loss, but the limit on how many atoms can be held in the waveguide depends on the atom density, and thus the temperature. Additional evaporative cooling can thus increase the atom density and therefore the number of atoms inside the waveguide. Evaporative cooling of the atoms will also reduce Doppler broadening of the EIT signal. We also wish to avoid magnetic broadening of the EIT signal, and so the magnetic fields are ramped down whilst the dipole trap is transporting atoms into the hole. Note that it does not ramp to zero as there are background fields, such as from the nearby ion pump, that we wish to counteract. Again, there is significant complexity in finding the optimal parameters.

Using the Beer - Lambert law, assuming minimal atom saturation, then the Optical Density [30] is given by

$$Abs = 1 - \exp(-OD), \tag{4.1}$$

from which we can calculate the atom number for the data shown in Figure 4.13 using

$$OD = \frac{N\sigma_0}{A}. \tag{4.2}$$

This assumes that the atom density is the same throughout the interaction region, which is generally applicable as the beam waist of the dipole beam ($\approx 12\mu m$) is large compared to the diameter of the probe beam ($\approx 5\mu m$)A. From this we can estimate that there are approximately 365 atoms inside the hole, using the $F = 4 \rightarrow F' = 5$ transition. This is a significant improvement to that found in [30].

A primary concern is magnetic broadening, because ramping down the coils can take a significant amount of time (≈5ms) due to induction currents in the coil. We want to test if we can hold the atoms in the interaction region long enough for the coils to ramp down, before measuring the absorption ratio. To test this, the absorption ratio is measured for a range of hold times of the dipole trap and is fitted to [30]

$$Abs(t) = 1 - \exp\left(-\frac{\sigma_0 N_0}{A}\exp(-t/\tau)\right). \tag{4.3}$$

This assumes the atom number decays exponentially in time with lifetime τ. The results are shown in Figure 4.14

We can examine the effect of magnetic and thermal broadening by seeing how the transmission ratio varies with probe frequency, and comparing the linewidth with the expected natural linewidth of the transition. Figure 4.15 shows the transmission ratio as a function of probe frequency. This is fitted to a Lorentzian curve with a linewidth of 6.25 ± 0.89MHz, whilst 4.16 shows magnetic broadening due to the offset coils left on, increasing the linewidth by 18% to 7.38 ± 0.43. Leaving the coils at the current used for forming the MOT creates a magnetic field gradient of approximately 20 G/cm. This implies

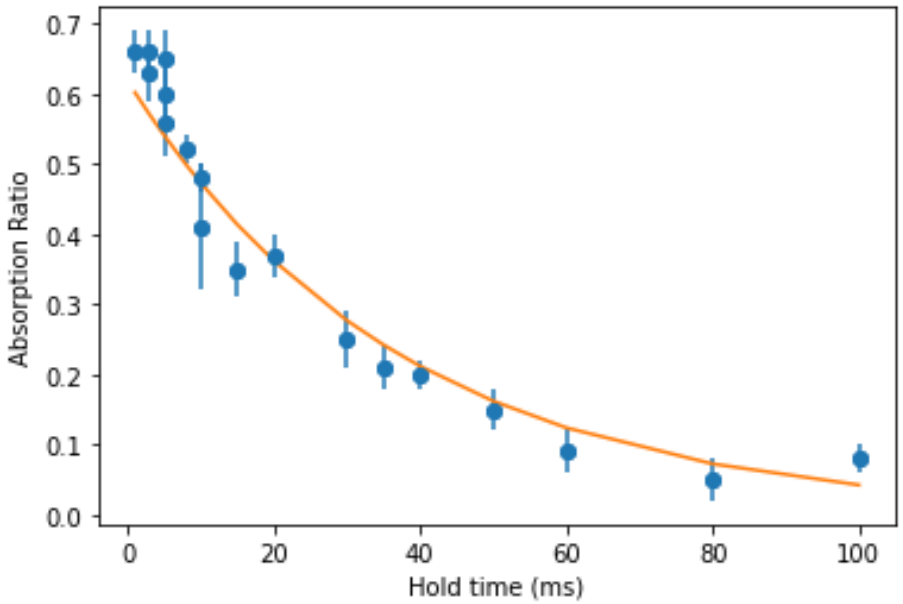

Figure 4.14: Absorption ratio plotted against the dipole trap hold time. Data is fitted to equation 4.3 from [30]. Lifetime is $26 \pm 2\mu$s.

the fibre is non-polarisation maintaining, as this magnetic broadening requires circularly polarised light, whilst the light going into the fibre is linearly polarised. We already know that the fibre is non-polarisation maintaining, so this is not unexpected. These graphs are taken with 5ms hold time in the trap, which seems sufficient to remove most of the magnetic broadening. This is a good result, as the lifetime of the dipole trap in the fibre is more than five times the time taken for the coils to ramp down.

The linewidth measured in Figure 4.15 is slightly larger than the natural linewidth [26], suggesting there is still some broadening due to either excessive probe power, or the atom cloud is insufficiently cool. It is also possible that the magnetic field has not entirely vanished at this hold time. The absorption ratio as a function of the detuning δ can be found using

$$Abs = 1 - \exp\left(\frac{-OD}{1 + 4(\frac{\delta}{\Gamma})^2}\right). \tag{4.4}$$

Fitting this equation to the data in Figure 4.15 provides the optical depth This can can be used in equation 4.2 to estimate that there are 170 +/- 70 atoms in the hole. This is very different to the value estimated from a single absorption shot earlier, but 7 percent transmission is unusually low and the result derived from the linewidth relies on a far greater number of data points. 170 atoms is thus likely to be closer to the true number, and is approximately

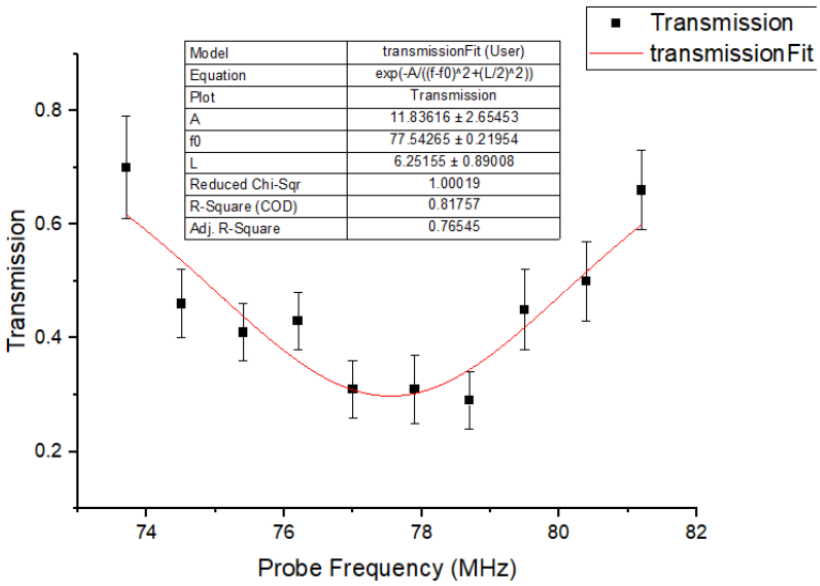

Figure 4.15: How the transmission ratio varies with probe frequency. Table shows equation and parameters used for fitting.

the number we are expecting, though the relative error is very high.

We also want to avoid saturating the atoms, which would reduce the absorption ratio. To examine the region of interest, we took repeated absorption ratio measurements for increasing probe power. There is a significant gap in data between 200 and 300 photon counts as a filter had to be changed to adjust the laser intensity. The result is shown in Figure 4.17. We see that atom saturation starts to occur at above 200 photons. This is important value to optimise to allow for a faster rate of data collection. Optimising the number of atoms in the hole allows for higher powers to be used for absorption measurements without saturating the atoms. This increases the signal to noise ratio, and thus reduces the amount of repeats needed to estimate the absorption ratio. After demonstrating we have sufficient atoms in the hole with a good transmission ratio, we can now look for EIT in the fibre.

4.5 EIT

Finding an EIT signal in the fibre proved a significant challenge, due to the small number of atoms and significant amount of noise made it fairly easy for background noise to be mistaken for a signal, which then took time to resolve. It is thus easier to see EIT in the MOT than in the fibre because of the large number of atoms and greater beam powers. This would help confirm that the probe and control frequencies were roughly correct to use for EIT in the fibre.

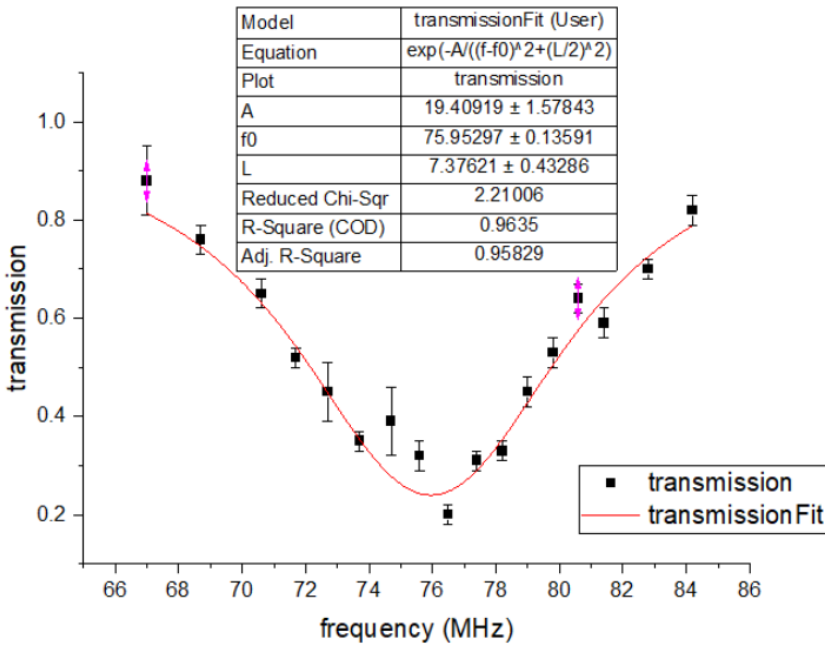

Figure 4.16: Transmission ratio as function of probe frequency with a magnetic field. Table shows equation and parameters used for fitting.

The frequencies for EIT in the MOT and for the fibre are expected to be close, but will differ due to differences in magnetic field and other conditions. The MOT encompasses a significantly larger volume than the hole in the fibre, and so the magnetic field gradient in particular will differ far more in the MOT than in the hole. However, it provides a good starting point and helps narrow the frequency parameter space.

To do this, the apparent atom number from absorption imaging is used to estimate the transparency. To specify, the actual number of atoms in the MOT is not affected by the probe and control frequencies, only the apparent number on the imaging. To add the control beam, the filters are removed and the MOT was moved close to the fibre, as the control beam disperses out the hole in the fibre. This explains why the MOT atom number is lower ($\approx 2 \times 10^6$ atoms). First the control frequency was varied, and a clear drop in apparent atom number is measured for a control frequency of approximately 126MHz, as shown in Figure 4.18. The 'probe' in this case is the imaging beam itself, and not the beam through the fibre. We can then fix the control frequency at this point and scan the imaging frequency, shown in Figure 4.19.

The EIT signal is significantly weaker when scanning the probe frequency, but there appears to be a weak transparency peak at 123MHz. These can then be used as the inital values for looking for EIT in the fibre. Initially, to find the EIT peak the control beam frequency was set to 126MHz and a scan of the probe

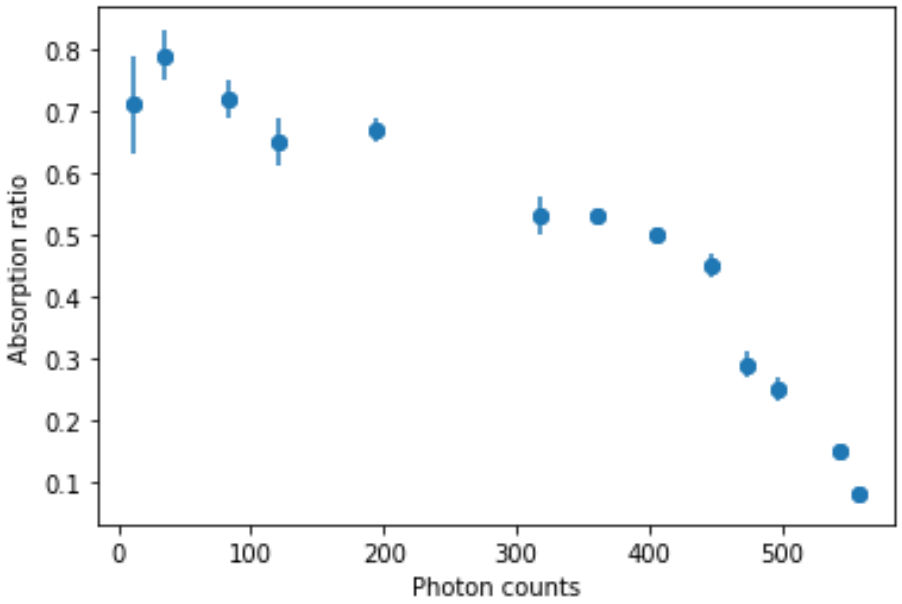

Figure 4.17: Absorption ratio falls for photon counts above 200.

beam frequency was taken. Significant repeats were needed to detect the signal, and we also experimented with leaving the magnetic field on. This would induce magnetic broadening of the EIT peak, and whilst this would reduce the size of the EIT signal it would also spread it further in frequency space, potentially making it easier to detect. Finally, a weak signal was found, as shown in Figure 4.20. Once a weak signal has been detected, it can then be optimised using the methods discussed in the previous sections. If the control frequency is not precisely on resonance, the EIT peak will be shifted away from the centre of the valley, as shown in Figure 4.21.

We thus needed to scan the control frequency to centre the EIT peak in order to optimise the transparency ratio i.e. the difference in transmission with and without the control beam. Figure 4.22 shows the optimal control frequency to be apporixmately 105MHz. After considerable optimisation of the MOT and dipole trap parameters, the EIT signal was significantly improved, as shown in Figure 4.23. The EIT peak is more centralised in the absorption valley, and the increase in transmission ratio with the control beam on resonance is much larger. This data is fitted to the imaginary part of Equation 2.23, from which the real part of the susceptibility can be calculated, as shown in Figure 4.24.

From this we can calculate the photon group velocity in the atom cloud to be approximately 500m/s. This will lead to time delay of ≈55ns, as the photons are slowed whilst in the atom cloud. This is a very short delay, despite the significant reduction in the photon velocity, as the hole is only 30 micrometers

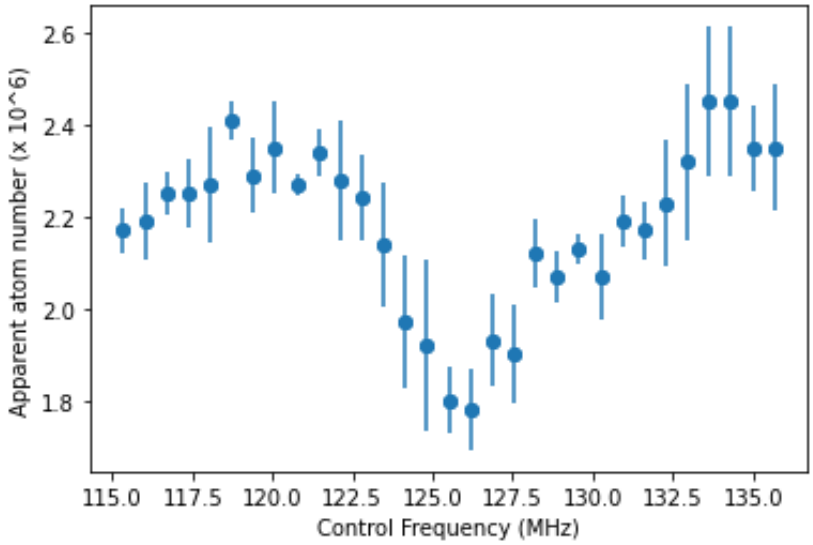

Figure 4.18: Apparent atom number plotted against control frequency. The imaging beam has a notable transparency peak through the MOT when the control frequency is $\approx$ 126MHz.

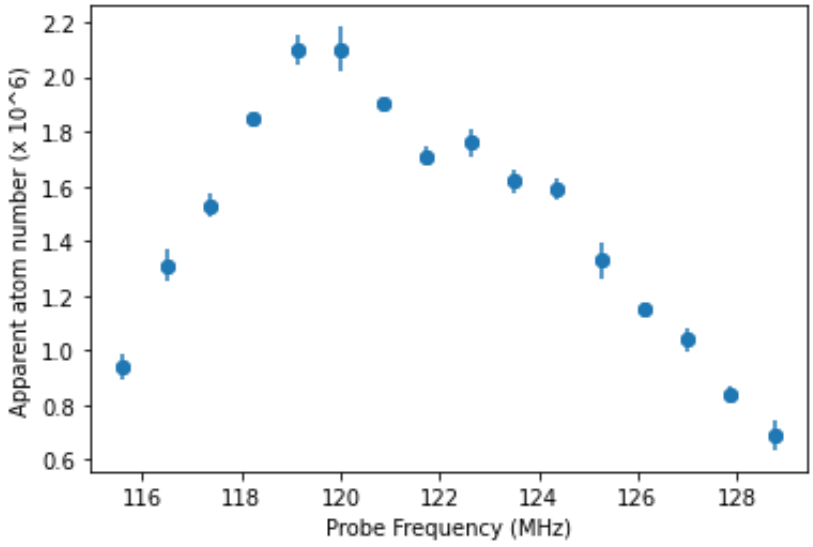

Figure 4.19: Apparent atom number plotted against probe frequency. The EIT peak is significantly weaker than in Figure 4.18, but there appears to be a transparency peak for a probe frequency of 123MHz.

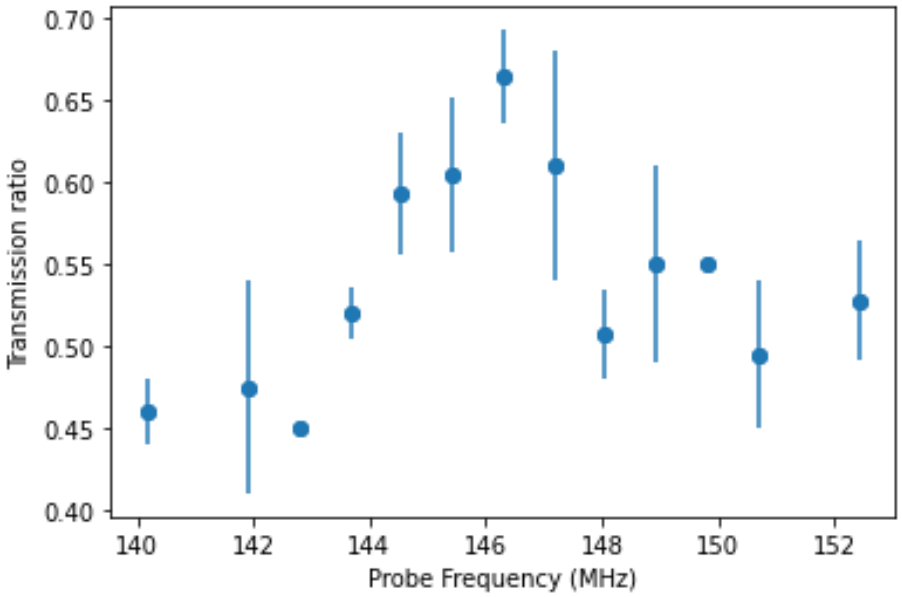

Figure 4.20: Transmission ratio plotted as a function of probe frequency. There is a weak initial signal of EIT in the fibre.

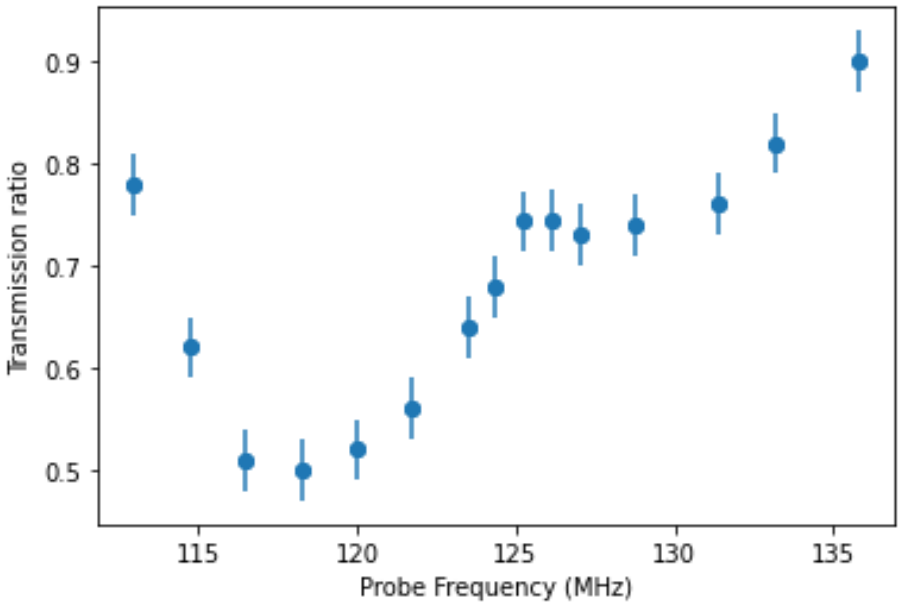

Figure 4.21: The EIT peak has been shifted by a difference in the control frequency. This also reduces the size of the EIT peak.

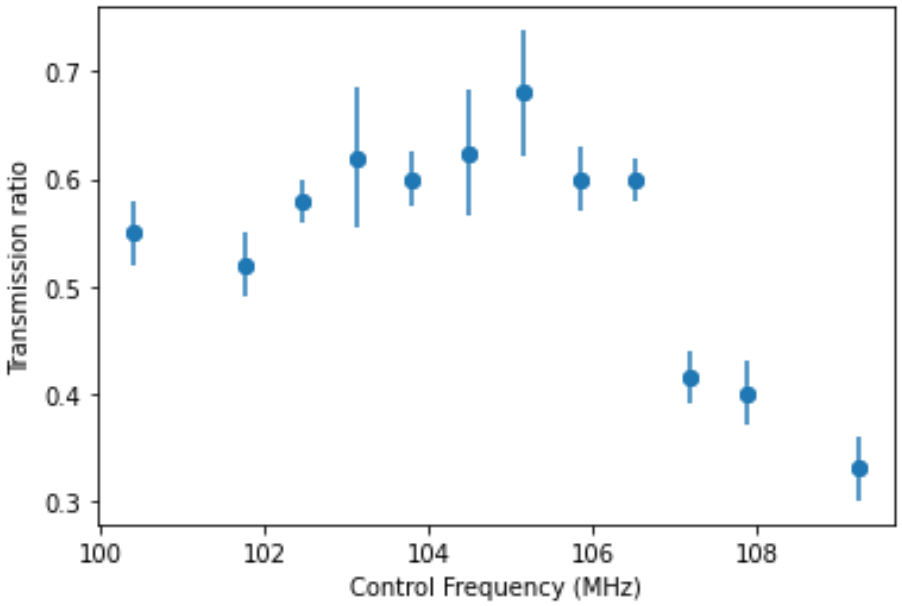

Figure 4.22: Transmission ratio vs control frequency. The data has significant uncertainty, but an optimal value appears to be setting the control frequency to 105MHz.

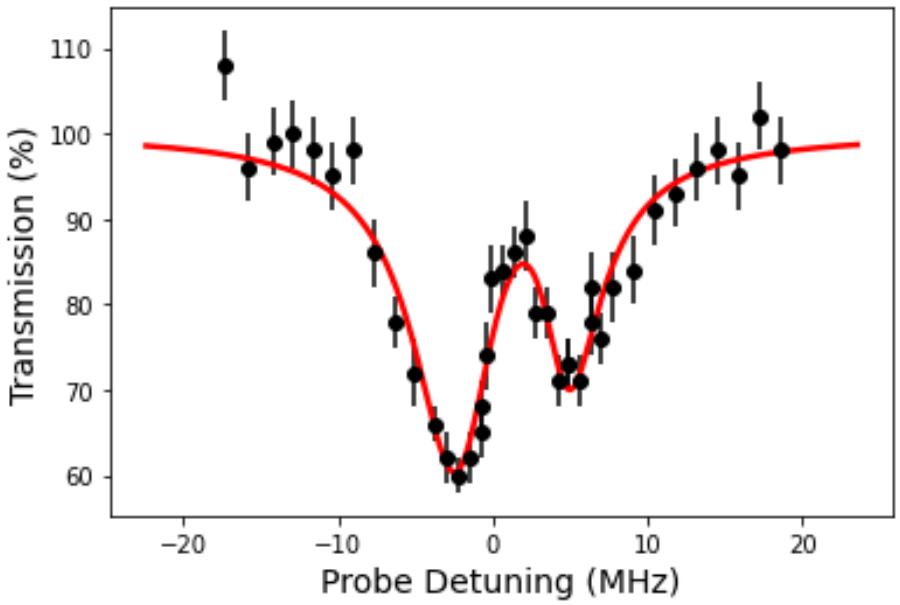

Figure 4.23: The black dots show the transmission ratio against the probe detuning. The red line is the fitted to the imaginary part of the susceptibility, given by Equation 2.23, from which the photon group velocity can be estimated.

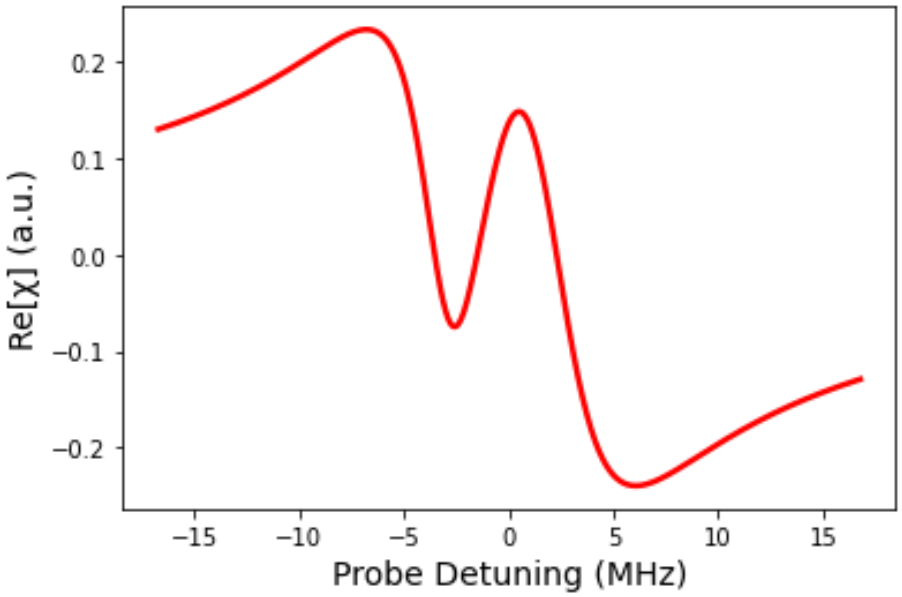

Figure 4.24: The real part of the susceptibility as a function of the probe detuning, derived from the data in Figure 4.23.

wide. Detecting the photon delay directly is a significant challenge. This is the current focus of the project carried on by another PhD student Matt Overton. The intention is to implement a setup that can measure this delay directly from the SPCM, and to further reduce the photon group velocity to make it easier to detect the delay.

4.6 Release and Recapture

Taking absorption experiments is lengthy, owing to the large number of repeats per absorption measurement. Plotting absorption vs frequency graphs is even more time consuming, and especially so when taking data on EIT in the fibre. Depending on number of repeats and how many points in frequency space are required, it can take over an hour. If data is taken over several days, then overnight drifts can make it difficult to repeat data, sometimes requiring work to fix laser stability issues etc. We would like a way to increase data collection rate. A potential method involves release and recapture. The principle idea is that after turning off the cooler beams for the dipole trap, then if turned back on sufficiently quickly then the atom cloud has not entirely dispersed. The hope is that this allows for recapturing of some if not most of the atoms, significantly increasing the loading rate. This could potentially allow for a significant reduction in the experimental cycle time, as forming the MOT takes

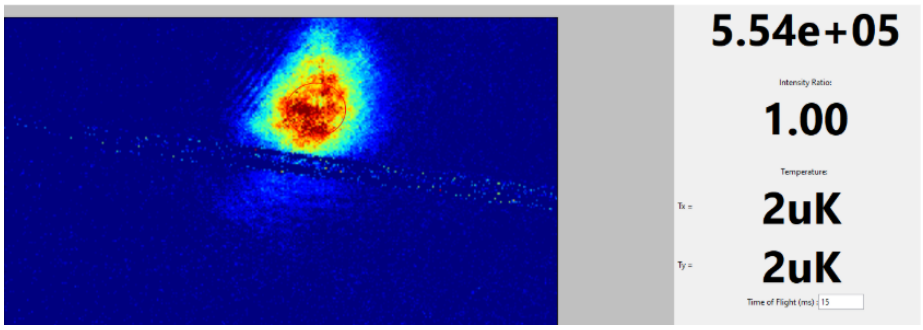

Figure 4.25: Initial release/recapture MOT.

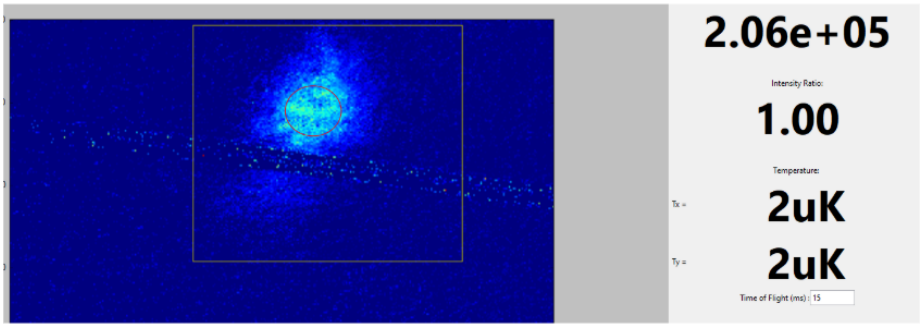

Figure 4.26: The MOT after 10 release/recapture cycles.

roughly 5s and is generally the longest part of the experiment. This could potentially be done with the dipole trap too, entirely bypassing MOT formation and allowing for much faster collection of fibre absorption data.

To test this idea, we first started looking at the MOT atom number after a number a release/recapture cycles, to see what fraction of released atoms could be recaptured, and trying to estimate the possible reduction in load time as a result. With a load time of 0.25s and a fall time of 25ms, the initial MOT is shown in Figure 4.25, and after 10 release/recapture cycles, the MOT is shown in Figure 4.26. We also looked at how the time between release and recapture affected the recapture efficiency. For a MOT with an initial atom number of 1.1×10^6, the atom number after 1 release/recapture cycle was measured, for a range of gap times as shown in Figure 4.27.

The efficiency of the recapture falls significantly after 35ms, which imposes restrictions on how long we can evaporatively cool the atoms. This could then broaden the EIT signal if the atoms are too hot, reducing the SNR. We also examined applying this method to the Dipole trap on horizontal axis. The initial trap is shown in Figure 4.28, and after 5 cycles, the Dipole Trap was imaged again, shown in Figure 4.29.

The measured atom number is approximately 10-15 percent less. This

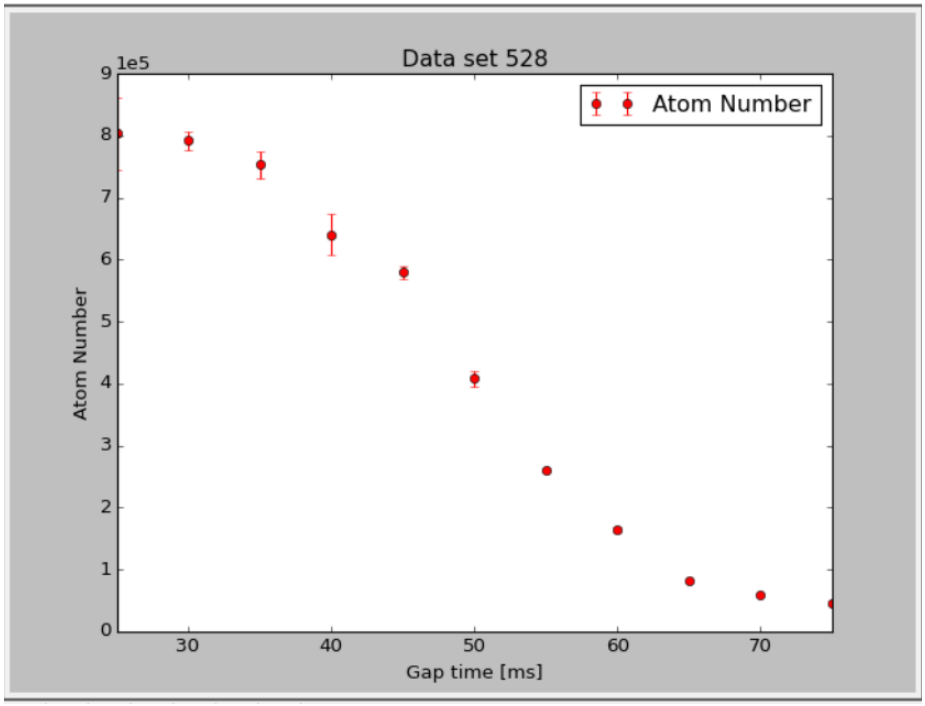

Figure 4.27: The atom number after 1 release/recapture cycle. The x axis is the gap time, which is how long the cooler beams are turned off for before implementing the recapture.

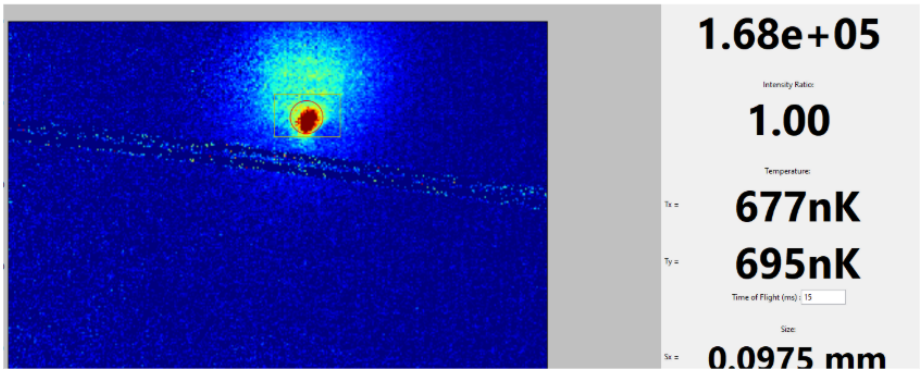

Figure 4.28: The Dipole Trap as seen on the horizontal imaging, before the release/recapture cycle.[1]

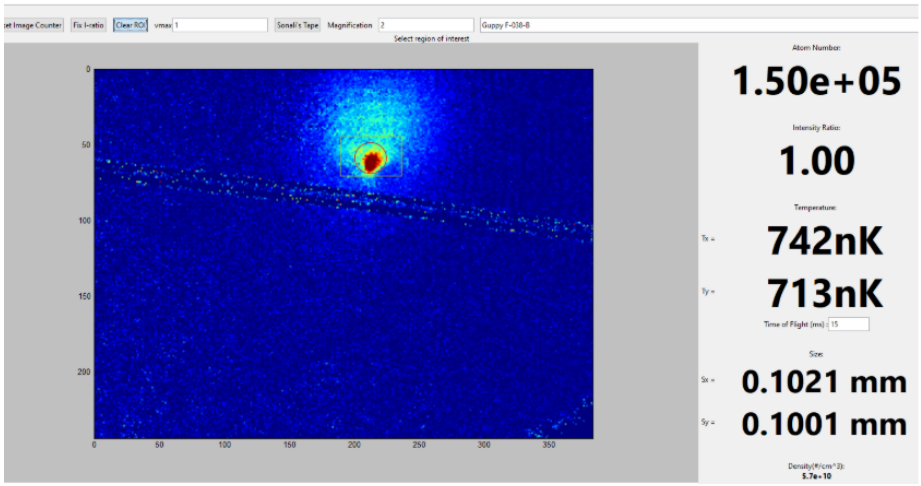

Figure 4.29: The Dipole Trap after 5 release/recapture cycles.

method is not currently implemented for two reasons. First is that the push phase moves the atom cloud away from the point it is formed, making the recapture method less efficient. Second is that significant improvements to the MOT has reduced the load time from 10s to 2s, and the improved absorption signal allows us to use only 40 repetitions per absorption measurement, rather than 100. This significantly reduces the time needed to collect EIT data and thus makes the recapture method less necessary. As such only a limited amount of time was dedicated to examining this technique.

We also examined the possibility of using Raman transitions for reducing the number of 2-body collisions in the dipole trap. One of the problems experienced with this experiment is the small number of atoms we can trap inside the interaction region at once. As we cannot change the size of the interaction region, we would instead like to increase the atom density. One way to do this is to introduce another beam 2nm blue detuned from the cooler transition. This is far enough away from any relevant transitions that laser stabilisation is not required. It has been shown [50] that such a beam excites atoms close to colliding into a repulsive molecular potentials, which suppress the inelastic collisions which result in 2 body losses. This would also increase the efficiency at which atoms are transferred from the MOT to the dipole trap, as during the dipole trap loading phase the MOT beams are left on as this improves the loading efficiency. However, these MOT beams also encourage two body losses, limiting the loading efficiency. If this additional detuned beam allows for an increased dipole loading efficiency, this could allow for a reduced loading time. We have already discussed our desire for an increased data collection rate and methods we have used to achieve it. This could also offer further improvements. Future work could therefore implement this in order to achieve a greater optical depth and further reduce the photon group velocity.

4.7 Conclusion and Outlook

We have successfully demonstrated EIT in the fibre, which is the primary aim of the experiment, and estimated the group velocity of the photons in the atom cloud and thus the expected photon delay. We have also examined the effect of magnetic broadening on the EIT signal and demonstrated how the EIT peak can be shifted around the absorption valley by shifting the control frequency. The immediate next step is to attempt to measure the photon delay through the fibre directly. This requires being able to reliably detect time delays in the SPCM signal to within tens of ns, a considerable challenge. This can be made easier by trying to increase the optical depth of the atom cloud inside the fibre, and so further reduce the photon group velocity. This can be achieved by further optimisation of the experimental parameters, and potentially utilising new lasers to pump the atoms into the $F = 3$ state whilst in the dipole trap and using Raman transitions to reduce collisional losses. Both of these would allow for an increased atom density inside the interaction region in the fibre. We have also examined using a release and recapture method to increase the data collection rate, which may be useful to implement in the future.

Chapter 5

Multi–frequency MOTs

It is of considerable interest to develop and improve techniques currently used in cold and ultracold atom experiments because of their wide range of applications. We have already mentioned how a variety of cold atom sensors and experiments are used in medical brain imaging [51], gravimeters [20, 21], quantum computers [4], and so on. There have also been proposals to use cold atom clouds to test certain theories of quantum gravity [2] and spontaneous wavefunction collapse [22]. In general, the usefulness and sensitivity of these devices is strongly dependent on the number of atoms that can be trapped and cooled. Any techniques that can increase the scale of these atom clouds will thus have significant implications for a wide range of fields.

Using wider beams is the simplest method of increasing the size of these atom traps, but this requires significantly more powerful lasers which are either expensive or simply unavailable for some frequencies. Many applications also have requirements for portability and miniaturisation, which makes using such lasers unattractive. We thus seek to demonstrate alternative methods to increase the size of these atom clouds.

Our primary idea is to add additional frequencies red-shifted from the primary trapping beam, in order to address a wider range of atom velocities. Previous work on dual frequency MOTs have demonstrated a three to fivefold increase in steady state atom number [23, 24]. We intend to develop this further by adding additional frequencies to trap a larger range of atom velocity classes. To do this, we want to create a frequency comb with a spacing of approximately 5 MHz, roughly the linewidth of the laser. It is extremely important that we have no light which is blue shifted relative to the primary trapping beam, as this would instead heat the atoms as discussed in the theoretical section. For this demonstration, we use ^{85}Rb due to the relative cheapness and stability of lasers at the relevant wavelengths. The upper limit for the velocity class of atoms addressed by the cooling beam is [31]

$$\nu_c = \sqrt{\frac{\hbar k D \Gamma}{m}}, \tag{5.1}$$

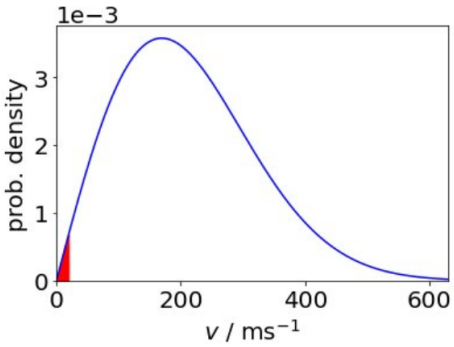

Figure 5.1: 1D velocity distribution of ^{85}Rb at 300K. The red shaded region highlights atoms for which $\nu < 20\text{ms}^{-1}$. Figure made by Ben Hopton.

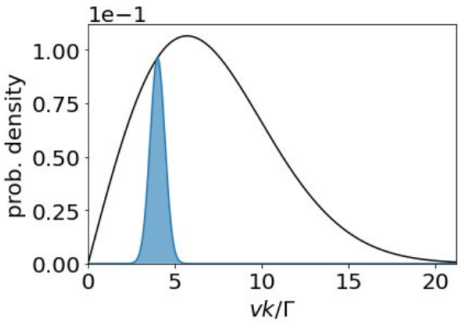

Figure 5.2: The pale blue region shows the atoms addressed by a beam 4Γ detuned from resonance and with linewidth Γ. Figure made by Ben Hopton.

where D is the diameter of the cooling beam. In general, the cooling beams in a MOT will only address a very small fraction of the total available thermal atom cloud. Figure 5.1 shows the thermal distribution of room temperature rubidium, and the small proportion, shown in red, which can be addressed for a reasonable $\nu_c = 20\text{ms}^{-1}$. Figure 5.2 shows the atoms addressed by a beam of linewidth Γ detuned by 4Γ. This region is appreciably bigger than the red shaded region in Figure 5.1, but still far from all the available atom velocities have been addressed, as clearly seen by all of the white area under the graph. Additionally, atoms addressed by this beam will lose thermal velocity and thus fall out of the range of atom thermal velocities being addressed.

If we instead look at multiple frequencies detuned by the linewidth Γ, then the range of atom velocities addressed increases significantly, as shown in Figure 5.3. Any atoms captured by the more detuned beams will slow down, and smoothly transition into the velocity capture range of another frequency beam. This process continues until the atom is cooled and trapped in a MOT.

We have focused on the velocity class of atoms addressed because the atom

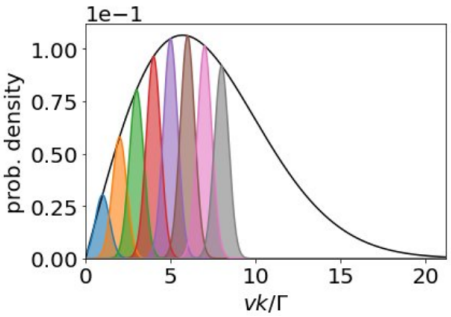

Figure 5.3: 8 beams, each detuned by the linewidth Γ, address a significant portion of the available atom velocities. Figure made by Ben Hopton.

loading rate for a MOT scales proportional to ν_c^4 [52]. Thus, this suggests multi frequency beams can lead to a very significant change in the loading rate. An increase by a factor of 1000 is not unreasonable, given the favorable scaling factor. The MOT size will not increase by anywhere near this amount, as collisional losses will also increase significantly. However, a factor of 10 in atom size might be expected. To reduce collisional losses, we aim to implement beam shaping to form ring shape, instead of a standard Gaussian beam. This reduces light intensity at the centre of the MOT, and so reduces collisonal losses. As the beam intensity is stronger on the edges, any atoms leaving the trap are address where the beam has the highest intensity, and so is pushed back towards the centre of the trap. Additionally, once the MOT has been loaded using multi frequency light, we then switch to a single frequency beam. As the atoms have been cooled down by this point, only a single frequency beam is needed to address all of the atoms.

5.1 Frequency Comb

This section will describe how we generate the desired frequency comb seen in Figure 5.3. We will want to be able to adjust the frequency difference between each tooth, hereon called the tooth spacing, as well as the ratio in amplitudes between successive teeth, called the tooth ratio. There are a few methods for creating the frequency comb we desire [53, 54], but our method involves shifting the output laser of a Tapered Amplifier (TA) chip with a pair of Opto Electonics MT122 - A1 - IR Acousto Optical Modulators (AOMs) which is then overlapped with the seeding light to the TA. We pick the 1st order beam from the first AOM and the –1st order beam from the second AOM. By ensuring that the driving frequency of the second AOM is never smaller than that of the first, we ensure that no blue shifted light is present. Each AOM is rated for 110 MHZ, and the driving frequency of each can be changed by roughly 10 percent in either direction before significantly affecting the coupling efficiency. Thus, by changing the driving frequency of each AOM separately, we can achieve any frequency

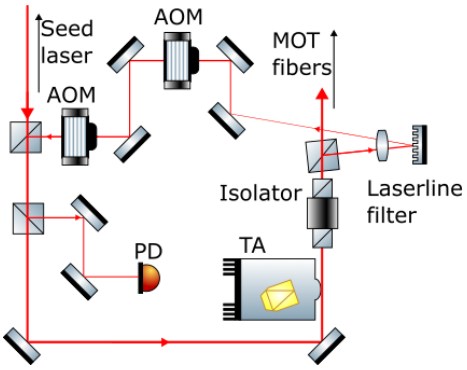

Figure 5.4: Light from the repumper and/or cooler laser enters the TA and is amplified. The TA output is split, with some going towards the MOT fibres and some reflected onto a laserline filter, which only reflects frequency at the seed frequency. This is then passed through two AOMs and so picks up a frequency shift equal to the difference in driving frequencies of the two AOMs. This light is then overlapped with the seed beam. There is also a pick off for seed light onto a photodiode, which is used to trip the TA and block the seed light if the seed power is too high.

comb spacing up to $\approx$ 22MHz. To protect the TA from excessive seed light, a small portion of the seed beam is incident on a photodiode, which sets the interlock to trip should the measured Voltage exceed a certain amount. This is shown in Figure 5.4.

We use a combination of cooler light locked to the $F = 3 \rightarrow F' = 4$ transition and repumper light locked to the $F = 2 \rightarrow F' = 3$ transition. This is because we want both the cooler and repumper to be multi-frequency, in order to maximise the effectiveness of the cooler beams. Part of the optimisation process is finding the ratio between the cooler and repumper seed power that maximises the atom number. The cooler seed input is beat locked off of a reference beam, which in turn is locked using Doppler free spectroscopy to the $F = 3 \rightarrow F' = 2 \otimes 4$ transition. Owing to the weak spectroscopy signal of the ^{85}Rb repumper transition, this laser is instead locked using DAVLL, as mentioned in the section on laser stability. We use DFBs for the repumper and reference lasers, and a Toptica 110 TA for the cooler. An overview on all of the laser locking methods used here is presented in section 3.1.

For absorption imaging, we take reference light on the $F = 3 \rightarrow F' = 2 \otimes 4$ transition and pass it through a 90MHz AOM which shifts the frequency onto the $F = 3 \rightarrow F' = 4$ transition. Whilst this method is simple and avoids needing a separate imaging laser, it does raise a problem. To find the optimal imaging frequency, the driving frequency to the AOM is adjusted. This, however, adjusts the alignment of the beam out of the AOM, which thus reduces the coupling efficiency into the fibre. To account for this, we increase the VCO level in the driver for the AOM, increasing the coupling efficiency through the AOM.

As such, we start with suboptimal coupling through the AOM and optimal coupling through the fibre before finding the optimal imaging frequency. We have calibrated this so that overall there is no change in power out of the imaging fibre when adjusting the imaging frequency.

When self seeding the TA, a notable problem is ensuring that none of the Amplified Spontaneous Emission (ASE) is coupled into the self seeding. This is because the ASE has a linewidth of approximately 10nm, and thus not only prevents forming a set frequency comb but will also introduce significant amounts of blue detuned light, which will heat up atoms in the MOT. A few different methods were attempted to remove the ASE without compromising the seeded light. Initially we used a holographic grating, usually used in ECDLs, which was placed in the beam so that the reflected beam passes through the AOMs. Such gratings have a very strong dependence on frequency for the reflection angle, and so can be used to remove all the unwanted ASE light. The frequency dependence is not so strong that it will prevent the additional frequency teeth from coupling back into the TA, which is important to ensure. The self seeding light is also passed through an iris to ensure that only light aligned with the seeded beam can pass through to overlap with the seeding light. This reduces the amount of ASE sent to through the self seeding loop by a factor of 80. Unfortunately this proved insufficient as the seeded loop was too inefficient for what we wanted. We thus replaced the grating with a laser line filter to remove the ASE. We also experimented with using a fibre to take the seeded light and overlap it with the seeding light, as this would hopefully prevent the dispersive ASE coupling into the fibre, leaving only the seeded light. However, this resulted in the frequency comb appearing as a sinc function, likely due to non-linearities in the fibre. With the laser line filter in place, the ASE was removed and so the fibre was no longer necessary. The problems caused by the fibre are shown more clearly in the next section.

Another potential problem is if the frequency comb is spread over a significant frequency range, then it may appear blue detuned to a lower transition frequency. For example, the cooler beam for this experiment is locked to the $F = 3 \rightarrow F' = 4$ transition. There is a 120MHz separation between the $F' = 4$ state and the $F' = 3$ state. Thus if the frequency comb is spread over > 80MHz, then the lowest frequency of the comb will start to appear blue detuned from the $F = 3 \rightarrow F' = 3$ transition. As mentioned before, this will lead to unwanted heating of the atom cloud.

To solve this problem, we use a vapour cell as a frequency dependent saturable absorber. Alignment through the cell is not critical, and so it is easy enough to add to the system. For the fundamental frequency, the power is significant (≈ 100mW) and so will not be appreciably attenuated by the cell. For the lower frequency teeth, the power is much reduced, and so the attenuation becomes significant. Modelling the effect of the saturable absorber is non trivial, as the desired teeth spacing is comparable to the linewidth of the laser. Thus, one frequency tooth can excite a velocity class of atoms and thus render the atoms 'invisible' to the nearest frequency spacing. As we then amplify the output and send it back through the cell, the overall effect on the frequency comb

becomes considerable. We would like to simply place a cutoff below which there would be no teeth, but this is unrealistic. Instead, there will be a significant attenuation of any frequency below the saturation limit of the vapour cell. Part of our experiment is to find the optimum frequency for this cutoff. This has not yet been implemented, as we are still experimenting with only a few frequencies, and so the mentioned problem has not yet been noted. When we do experiment with additional frequencies, then implementing this step will be important.

At the current stage, we have not yet found the optimal frequency comb to use, and this remains a significant area of experimentation. Whilst the current setup has demonstrated an increase in atom loading rate, we intend to make further adjustments as necessary.

5.2 Fabry - Perot Interferometer

To measure the resulting frequency distribution, we use a SA30 Thorlabs scanning Fabry – Perot (F - P) Interferometer, with a finesse exceeding 1500 and a theoretical resolution below 1 MHz. We can thus compare the frequency spectrum of our beam with the resulting MOT to optimise atom number, density and temperature. Due to the method of creating the frequency comb, we expect to see an exponential decay in power for each tooth of the comb, as each 'loop' will in theory result in the same attenuation. The Fabry Perot scanning interferemeter is a key apparatus used to measure the frequency distribution of the light. The cavity consists of two mirrors with reflectance $> 99.9\%$ placed 50mm apart, with one of the mirrors mounted on a piezo to allow the length of the cavity to be fine-tuned. The high reflectivity of the mirrors mean a well aligned input beam will travel many round trips before leaving the cavity. Standing waves will form due to constructive interference if the length of the cavity is an integer multiple half the wavelength. All other wavelengths destructively interfere and so do not form such standing waves. In this case we have a special case of cavity where the radii of curvature of the two mirrors are both equal to the separation of the mirrors, d, called a confocal cavity. The laser must be aligned to the cavity, first by observing the spatial modes. For a confocal cavity, and assuming the incident beam is Gaussian, only frequencies satisfying

$$\nu_{qmn} = \frac{c}{2d}\left(q + \frac{m+n+1}{2}\right) \tag{5.2}$$

can exist inside the cavity [55], with all others destructively interfering. Here, q, m and n are the mode numbers, and all take non-negative integers, and c is the speed of light. These represent the spatial modes, and the first few orders are shown in Figure 5.5. The frequency difference between repeated fundamental modes is the Free Spectral Range (FSR). Our interferometer has a FSR of 1.5 GHz, more than sufficient to observe the frequency comb we wish to create.

To use the Fabry - Perot correctly, the incident beam must first be aligned so that only the fundamental order spatial mode is maximised, with all other orders suppressed. The Fabry – Perot interferometer is placed on a breadboard

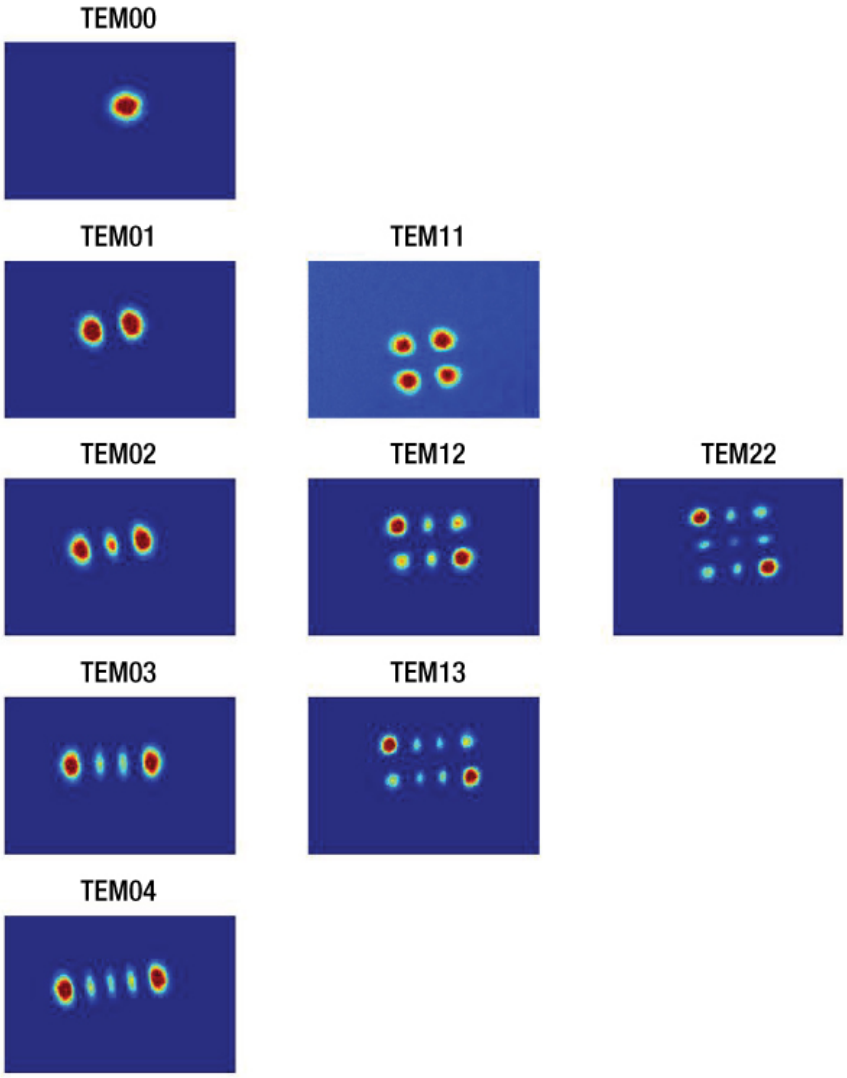

Figure 5.5: Fundamental and higher order spatial modes of a Fabry - Perot Interferometer. Taken from [56].

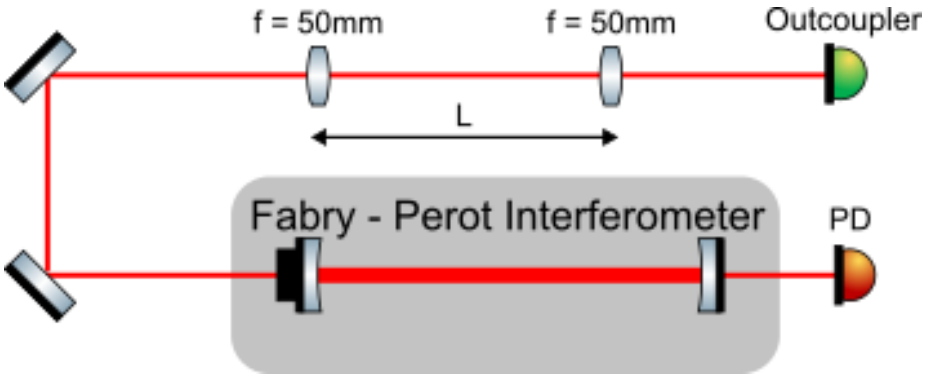

Figure 5.6: A simple diagram showing the set up of the Fabry - Perot cavity.

along with the fibre out coupler, a pair of lenses each with a focal length of 50mm and the pair of alignment mirrors. A diagram of the set up is shown in Figure 5.6. Placing the Fabry - Perot on a breadboard allows us to move the setup where we want to without needing to realign the Fabry – Perot each time. We use two lenses instead of one so that the focal length of the compound lens can be fine tuned by adjusting the distance L between the two lenses. The focal length of a compound lens system can be calculated using

$$\frac{1}{f} = \frac{1}{f_1} + \frac{1}{f_2} - \frac{L}{f_1 f_2}. \tag{5.3}$$

In our case, $f_1 = f_2 = 50\text{mm}$, so the equation simplifies to

$$f = \frac{2500}{100 - L}. \tag{5.4}$$

The Fabry - Perot cavity itself is mounted on a translation stage, so that its distance from the lens system can be fine tuned. The two lens are cage mounted to the out coupler, to ensure the beam travels through the centre of the lens. The first lens can be moved along the cage system to change the distance between the lenses, and the second lens is bolted to the breadboard.

To align the beam onto the Fabry - Perot, first the centre of the Fabry - Perot is marked and then the interferometer was removed. The distance between the two lenses is then adjusted so that the beam was focused at the point marked. The Fabry - Perot is then put back on a translation stage. An infrared camera is placed behind the cavity and the laser alignment, translation stage and L are adjusted such that only the fundamental spatial mode is visible. Then, the camera is replaced by a photodiode connected to an oscilloscope. The alignment, translation stage and distance L are then further tuned to suppress all higher order modes. A neat trick is to split the output of the Fabry - Perot onto two different channels on the oscilloscope, each on a different voltage scaling. This allows both the fundamental and higher order modes to be viewed simultaneously. The mirrors and the distance between the lenses are adjusted to

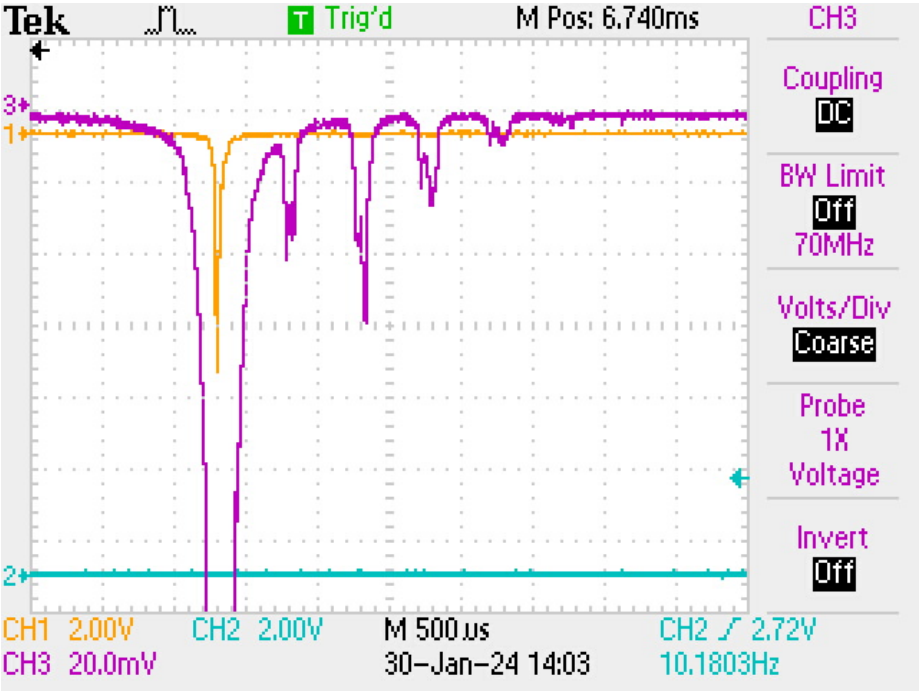

Figure 5.7: Yellow shows the full frequency spectrum, with only the fundamental spatial mode visible, whilst purple is zoomed in on the vertical axis by a factor of a hundred, allowing for the higher order spatial modes to be seen. This allows for a clear comparison between the fundamental and higher order modes. The 2^{nd} order is $< 1\%$ of the fundamental order.

minimise the ratio between the higher order modes and the fundamental mode. We have been able to reduce this ratio to 1%. Figure 5.7 shows this. The yellow line shows the fundamental mode clearly, but the higher order modes are not visible. The purple line is the yellow line scaled up by a factor of 100 so that the fundamental and higher order modes could be seen simultaneously, and the ratio between them maximised. The FWHM of the fundamental mode is 3MHz, which provides a resolution slightly higher than specified, but still small enough for our purposes. With the Fabry - Perot now well aligned, we can characterise the frequency comb, shown in Figure 5.8.

The initial frequency comb, before tweaking the self seeding loop, showed a few problems. The tooth ratio is poor, and there is a strange 'bump' in the intensity for the 8th and 9th teeth. A naive approach is to try to fit a sinc function, shown in the red dotted line, but this provides a poor fit. It is possible this is due to the grating, as the alignment is frequency dependant, and it is also possible the side frequencies are poorly coupled through the fibre. We also see a blue detuned peak in the frequency comb, but on further examination

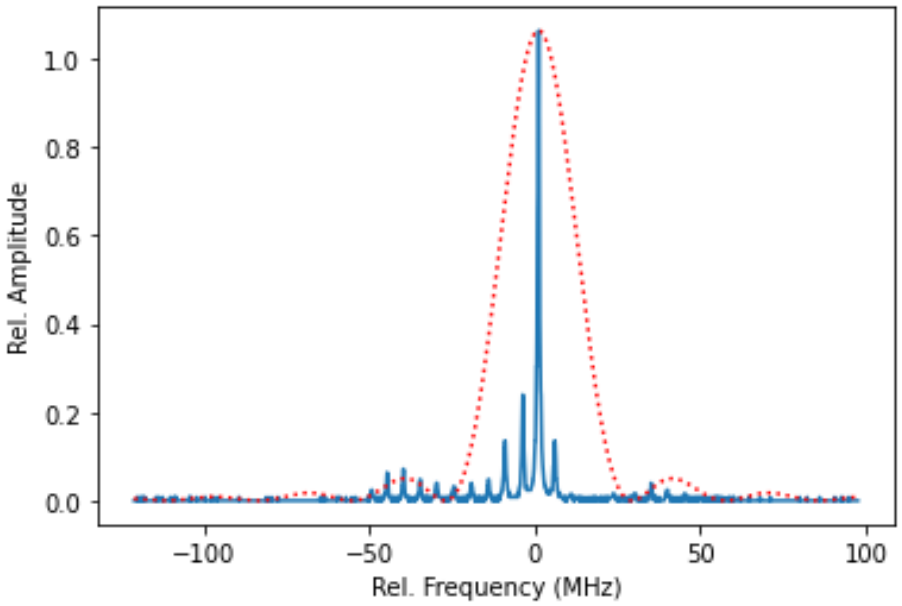

Figure 5.8: The initial frequency comb. Here we are only interested in the relative frequencies of the higher order modes compared to the fundamental. The tooth spacing is 5MHz and the dotted line is a sinc function.

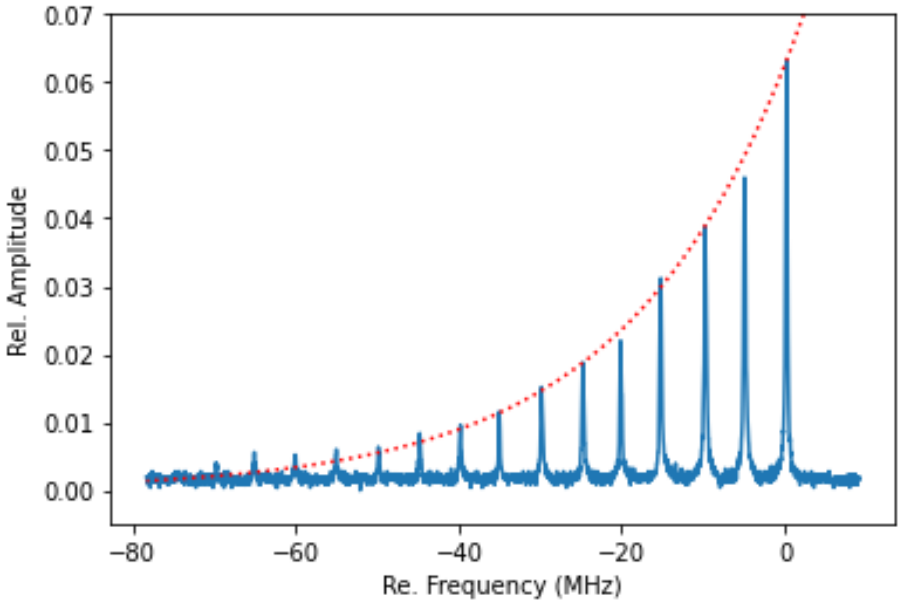

Figure 5.9: A frequency comb generated without a fibre or grating. The red dotted line is an exponential decay curved fitted to the maximum intensity of each frequency tooth.

by looking at the light just after the AOM does not reveal any blue detuned light. We also saw a strange 'mirror' effect when using just 1 AOM, where there appeared to be a slightly weaker reflection of the red detuned teeth on the blue detuned side. We believe this to be some artifact of the Fabry - Perot, as the frequency comb generator had no means of generating blue detuned light.

Unfortunately, we could not find anyone else who had a similar problem, and so the cause of the effect is still unknown. This did prompt a redesign of our frequency comb generator, mainly by removing both the grating and the fibre, and instead relying on a frequency filter. We also adjusted the alignment of the beam through the self seeding loop. It took a significant amount of time to find a self seeding setup that produced the desired frequency comb, but after a while, we managed to generate a frequency comb that showed the expected exponential decay, as shown in Figure 5.9. This suggests either the fibre or the grating was the source of the problem, and in the future we should rely solely on the frequency filter to remove the ASE. Great care also needs to be taken when aligning the self seeding loop to ensure the optimal frequency comb is generated.

5.3 TA output analysis

Whilst using the TA for multi–frequency comb generation, we have noticed that the output is lower than expected when seeding with multiple frequencies. The phenomenon has also been noticed when using the TA to amplify the cooler and repumper light simultaneously, which we would like to do in order to achieve high enough power in the repumper beam. This section will cover in detail these results, the conclusion we can draw from them, and how this will effect our experimental approach.

Firstly, we examine the cooler and repumper seeding the TA independently. Figure 5.10 shows the measured power output of TA for either cooler or repumper. The data was collected as part of a greater analysis of the TA, and so the repumper and cooler seed powers were scanned simultaneously, explaining the repeats shown in Figure 5.10. However, for this data, the beam not being examined was blocked, and so there is only cooler or repumper in the seed, not both.

We see that the repumper appears to couple much more efficiently to the TA than the cooler, particularly at low powers. For example, with the repumper seed at 4 mW we measure an output of 220 mW, compared to the cooler at 5 mW seed power produces only 180 mW of TA output. This suggests that the beam alignment, polarisation or beam shape is sub-optimal for the cooler seed. We also see that at about 20 mW of cooler seed, the TA output starts to saturate. This data was taken at a TA current of 1 A. The TA can take 5 A current and 50 mW of seed before being damaged, so it is likely that at higher currents the saturation limited for the seed power will be higher. At the moment, we are still experimenting with the TA, and so deliberately limiting the TA current to avoid risk of damaging the TA. At the low dispenser currents

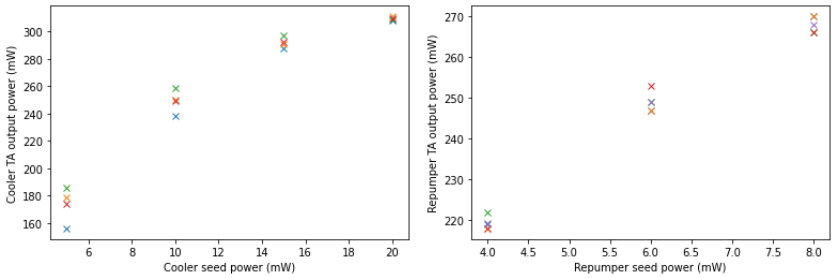

Figure 5.10: The measured power out of the TA solely with cooler seed (left) or repumper seed (right). Different coloured crosses correspond to repeated measurements.

we are using, the cooler power for atom trapping also saturates at ≈ 40 mW, and so excess cooler power will simply induce greater collisional losses. When we are happy with the TA and the multi–frequency generation, we will progress to higher currents and beam powers.

For now, we simply want to examine how the TA behaves when seeded with multiple frequencies. Figure 5.11 shows the measured and expected powers out of the TA when simultaneously seeded with the cooler and repumper beams of varying powers. The expected values were calculated by summing the individual TA output powers for the cooler and repumper shown in Figure 5.10. This naive approach will ignore saturation effects of the TA, but it is quickly apparent that that this alone cannot explain the results. We see that for all cooler and repumper powers considered, the measured output is only $\approx 60\%$ of the expected output from Figure 5.10. This is true even at low powers, below the point at which saturation effects should become apparent. Consider, for example, the result on the far left, for a cooler seed power of 5 mW and a repumper seed power of 4 mW. The cooler results in Figure 5.10 show that a total of 9 mW of seed power is well below the saturation point, and yet the measured output power is only 68.8% of the expected output. This is actually the closest between the expected and measured results. At the highest repumper and cooler seed power, the ratio between the measured and expected power output falls to 55.8%, indicating that at higher powers the TA does start to saturate, as expected.

We would also be able to find to composition of the TA output when seeded by cooler and repumper light together. The Fabry - Perot is used to measure the frequency spectrum of the output. By measuring the area between the Fabry - Perot signal and the x axis, we can estimate the power in the cooler and repumper transitions in the output of the TA. First, we divide the area under the graph by the measured output from a power meter, for the cooler and repumper separately. The data is then normalised to the first data point, to show the relative measured intensities on the Fabry - Perot and the power

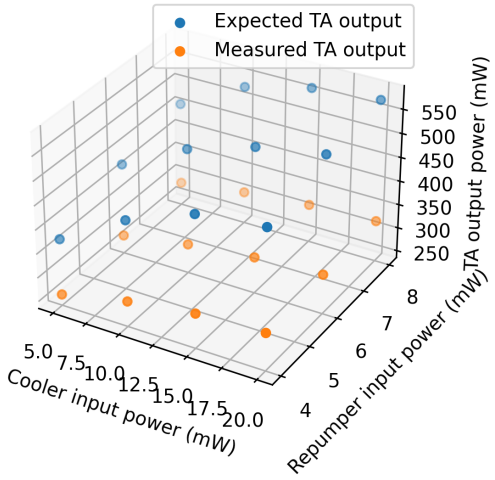

Figure 5.11: The measured (orange) and expected (blue) power output of the TA, as a function of cooler and repumper seed power. The expected values are calculated by summing the outputs of the individual cooler and repumper seed powers from Figure 5.10.

meter. This is shown in Figure 5.12, for both the cooler and repumper.

Unfortunately, there seems to be little agreement between the measured power output of the TA and the area under the graph given by the F - P. We would expect the ratio to remain constant across the seed power for both the cooler and repumper. The cooler results are even stranger in that the repeated measurements do not agree, as they do for the repumper. It is possible that the Fabry - Perot is simply not optimally aligned, as Figure 5.10 shows the TA behaves reliably for repeated seed powers. The repumper data is more reliable, as can be seen, but the sudden increase in intensity on the Fabry - Perot compared to the TA output for 8 mW of seed power is also unexpected. This would suggest the coupling to the Fabry - Perot in changing for different seed powers, or different power outputs of the TA.

When we consider seeding the TA with cooler and repumper simulaneously, the results are shown in Figure 5.13. Here we again divide the area under the graph for the cooler and repumper frequencies by the total output of the TA, as the power meter cannot measure power as a function of frequency. This time we are scanning the cooler and repumper seed powers together. Again, the ratio between the two strongly depends on the seed power.

These results suggest that there is also something about the F - P that we do not fully understand, as we would expect that the area under the graph on the Fabry - Perot should correspond with the total beam power. However, one point to note is that the measured intensity of one of the frequencies on the Fabry -

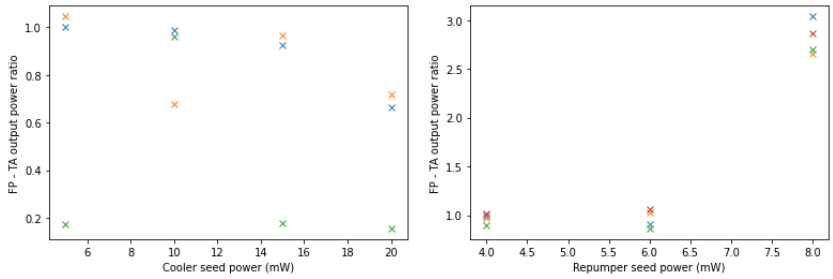

Figure 5.12: Comparison of the measured TA output and F - P measurement for only cooler seed (left) and only repumper seed (right). Different colour crosses indicate repeated measurements.

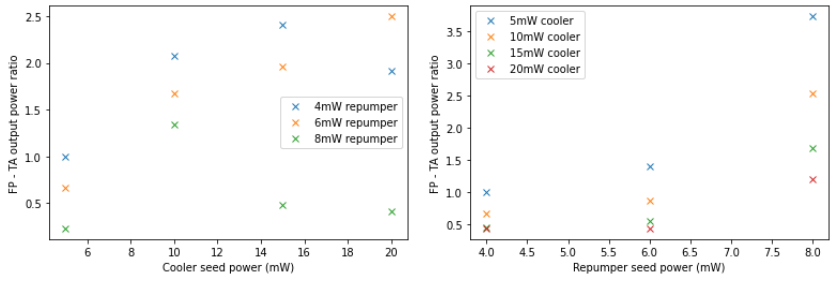

Figure 5.13: Comparison of the measured TA output and F - P measurement for the cooler (left) and repumper (right) with both cooler and repumper seed. Legend shows amount of seed power in beam not on x axis.

Perot falls when more light of other frequency is present. For example, consider the measured repumper intensity (right in Figure 5.13). The ratio between the Fabry - Perot and the TA falls for higher cooler powers for all repumper seed powers. It was noticed when taking the data that the area under the graph for a given frequency fell when more of the other frequency was present, whilst adding more power of either frequency would increase the output of the TA.

This analysis has provided some insight into how the TA behaves with multi–frequency seed. This will not necessarily mean the TA will exhibit similar behaviour when self seeding, as the maximum frequency difference in the case will be less than 100 MHz, compared to over 3 GHz difference between the cooler and repumper frequencies. Future work will examine the behaviour of the TA and the Fabry - Perot in more detail by also considering higher TA currents, as it is possible the TA is not seeding correctly. We will still attempt to use the multi–frequency comb we have developed to improve the MOT loading rate and steady state atom number, as we will discuss in the next section.

5.4 Multi–frequency MOT

Having created the desired frequency comb, we then sought to use this to increase the atom number of the MOT. Unfortunately, this did not lead to an immediate improvement in loading time or steady state atom number. A significant amount of time was spent adjusting the self seeding loop alignment, the ratio of power sent to the MOT vs sent back through the seeding loop, and the ratio between the cooler and repumper power in the seed beam. Eventually, a small improvement in loading rate was measured, as shown in Figure 5.14. The improvement is more noticeable in the loading rate, as expected, with the multi frequency MOT showing a 18% increase in atom number at 5 seconds. The improvement is less noticeable in the steady state atom number, as the difference narrows to almost within the uncertainty at a load time of 15 seconds. This is a promising start, but not the improvement we are hoping for. Further tuning of the frequency comb is thus necessary.

These data was taken with just a multi frequency cooler beam, whilst the repumper was single frequency at 16mW for both data sets. The frequency comb that resulted in this improvement is shown in Figure 5.15. This is an unusual spectrum, with what appears to be blue detuned light relative to the fundamental frequency. It is possible that the comb has been shifted so that there is no blue detuned light relative to the atomic transition, as the Fabry - Perot only shows the frequency distribution, and not the absolute frequency of each tooth. This suggests there is much work to be done before the optimal frequency comb is developed.

The tooth spacing is 4 MHz, and the cooler power was 80 mW for the single frequency and 75 mW for the multi frequency. This suggests there is still something about the self seeding loop we don't understand, as directing power back into the seed should increase the TA output to more than compensate for the power diverted to the seed, but this is not the case. Still, despite the

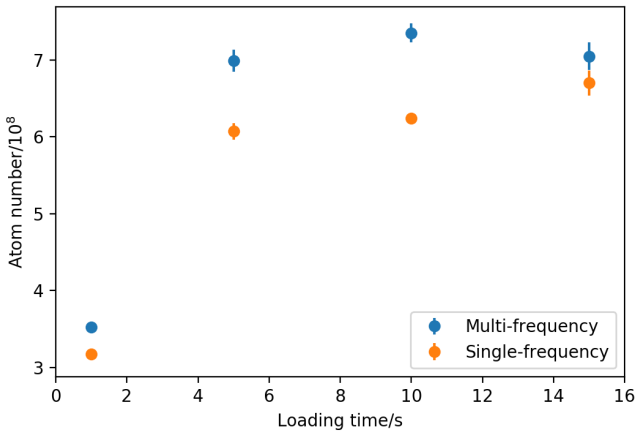

Figure 5.14: The atom number of the MOT for different loading times, for both single and multi frequency cooler beams.

reduced cooler power, a notable increase in atom number was measured. The dispensers were set to 3.4A. This is not the optimal current for maximum atom number, but at the moment we are working with lower dispenser currents to prevent them from burning out too quickly. When we have found the optimal frequency comb, we can then increase the dispenser current to try and maximise the atom number of the MOT.

We have also begun implementing a 'dark spot' MOT, to reduce collisional losses. These losses are caused by atoms colliding whilst at least one is in an excited state. During the collision, the atom de-excites and the energy is converted to kinetic energy, which gives the atom enough energy to leave the trap. To create a dark spot MOT, a small blockage is placed in the centre of the repumper beam to reduce the light intensity at the centre of the MOT. This should reduce the light induced collisional losses, whilst the light intensity at the edges of the MOT remains the same to prevent atoms from leaving the MOT. We block the repumper as this beam is already saturated, and so a reduction in beam power will not effect the MOT significantly.

We are currently experimenting with the best approach, by altering the size of the blockage and also combining this ring beam with a standard Gaussian beam with reduced beam power. Over long distances, diffraction of the light will reduce the efficiency of the ring beams as light diffracts back towards the centre. We are also examining how best to combine this approach with the use of multi frequency light, and whether the single frequency beam should also be ring shaped. Another approach is to red detune the repumper so that it is only on resonance with the hot, room temperature atoms and not the atoms trapped in the MOT. This would act like a dark spot MOT, in that light induced collisional losses would be suppressed, whilst the MOT could still be loaded and

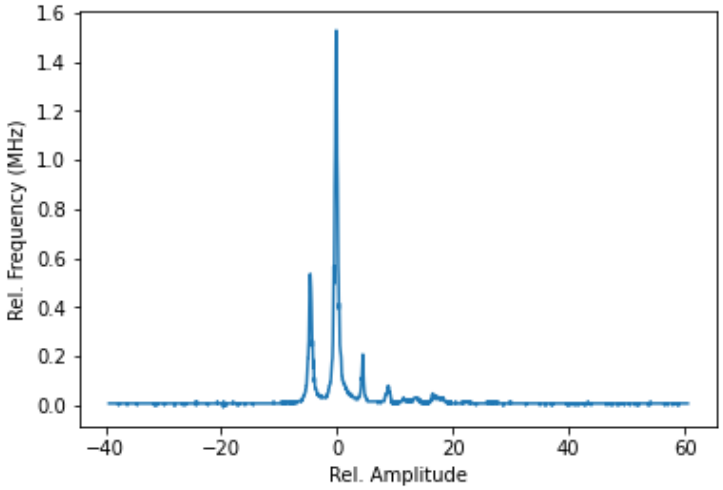

Figure 5.15: Frequency comb used for the cooler light in for the multi frequency MOT in Figure 5.14.

atoms cooled. Any cool atoms leaving the MOT would be shifted onto resonance with the repumper by the magnetic fields. The advantage of this method over a standard dark spot MOT is that it is simpler to implement, requiring only a change in the repumper frequency and no additional optics or beam shaping. Further work will examine how useful this technique is.

5.5 Concluding Remarks

The project as it currently stands is still in the process of significant change and experimentation with regards to the setup, and here we have only covered what has been tested so far. There remains significant work to be done to demonstrate the full capability of a multi frequency MOT, but we have already shown a 20 % improvement in loading rate. Further experimentation will be done in generating the frequency comb, as well as timings for the single frequency beam.

Once the atoms have been trapped and cooled down, then all the atoms will have a similar velocity and so only one frequency of light is needed. When we have loaded the multi–frequency MOT, we will then use only a single frequency beam to hold the MOT, at which point we can introduce a molasses stage.

We have already mentioned that previous papers have shown that the extra frequency components increase the rate of two body losses, and so during the molasses stage the beam from the TA will be blocked with a shutter, whilst another shutter will open which will allow light from the Toptica and repumper, which initially seed the TA, directly into the chamber as the single frequency light.

Chapter 6

Additional Projects

This section discusses additional projects not already mentioned in previous sections. These are smaller in scope and thus are collected together in a single chapter. Where relevant I have highlighted my own contributions to these projects, and despite their smaller size they are included for interest and completeness. In general these projects seek to make cold atom experiments more viable outside of the lab by offering methods for improved stability against noise or by reducing the size of various systems, thus improving portability. There has already been a significant amount of work done in the field [57–60].

First we consider dual frequency locking, a method which exploits optical pumping effects to improve the feedback for laser stabilisation, thus improving frequency stabilisation. At the same time, it also reduces the components needed for locking multiple lasers. Details can be found in [61].

The second section looks at using additive manufacturing, more commonly called 3D printing, to produce a vapour cell. The benefits are improved flexibility and reduced costs compared to standard methods, enabling smaller cells with novel shapes to be manufactured. These cells were manufactured in the engineering department, and were passed to us for testing. The paper can be found here [62].

The third project involves coating 3D printed surfaces with passive pumping getter material in order to improve the passive pumping rate. This is of interest because some applications, such as satellite based cold atom experiments, have strong limitations on size and weight. Active pumping for vacuum systems are both large and power consuming, as well as requiring cooling systems. Passive pumping can thus offer significant reductions in size, weight and power requirements. By altering the surfaces which are then coated, the intention is to increase the effective surface area of these passive pumps and thus increase the passive pumping rate.

6.1 Dual frequency locking

Many applications require accurate laser locking with minimal noise or changes in frequency. This process was detailed in section 3.1 and is fundamental to many cold atom experiments [63–65]. This is particularly important in situations outside of the lab, where there will be significantly higher noise levels and a desire for mobility puts a premium on size and weight [20, 21, 66–69]. This might, for example, lead to a reduction in the size of vapour cells, which reduces the optical depth and thus the feedback to the laser. What is required is a way to reduce the number of optical elements needed whilst also increasing the feedback to the laser. One potential method which we examine here is the use of dual frequency locking.

6.1.1 Motivation and Apparatus

When building cold atom experiments, in general the lasers are locked to cycling transitions. For experiments using ^{133}Cs, for example, the cooler laser can be locked to the $F = 4 \rightarrow F' = 5$ transition of the D_2 line. Atoms in the $F = 4$ state absorb the light and get excited to the $F' = 5$ state, shown in figure 6.1(b). These atoms usually de-excite back to the $F = 4$ state, releasing a photon, and so the cycle continues. However, the atoms will occasionally decay to the $F = 3$ state via non-direct pathways. Atoms in this state cannot absorb the cooler light, and so will reduce the spectroscopy signal. We have already discussed that to prevent this, we add 'repumper' light on the $F = 3 \rightarrow F' = 4$ transition. This pumps the atoms back into the cycling transition, improving the absorption of the cooler beam. This also means that the presence of the cooler light will improve absorption of the repumper light for exactly the same reason. When working with a MOT, this improvement in repumper absorption is usually not relevant, but it is important when seeking to improve the spectroscopy signal and thus the feedback and so improve laser stability.

What is needed, therefore, are two lasers locked to different transitions, and we know that the presence of the repumper improves the absorption of the cooler and visa versa [1]. Thus, it makes sense to try to lock the two at the same time. To do so, two linearly polarised beams with orthogonal polarisation axes are overlapped at a polarising beam splitter (PBS). As the polarisation axes are orthogonal, there is minimal interference between the two lasers. It also allows the two lasers to be overlapped and split using polarising beam splitters. By overlapping the two beams, we take advantage of the fact that the repumper increases the absorption of the cooler light by the atoms, which increases the signal strength. Simultaneously, we are also only using one vapour cell, so the system is smaller. The overlapped beams are then passed through a vapour cell, before the two lasers are separated with a PBS and aligned to separate photodiodes, so that the cooler and repumper signals are separated. The setup is shown in Figure 6.1, along with the transitions used for ^{133}Cs and ^{85}Rb.

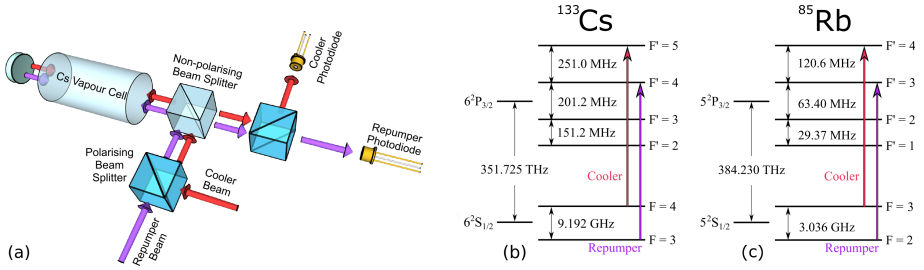

Figure 6.1: a) Experimental setup for dual frequency locking b) Laser transitions used for Cs c) Relevant transitions for Rb.

6.1.2 Dual Frequency Spectroscopy

An example of the improvement obtained using this method can be shown by examining the repumper spectroscopy of ^{133}Cs. Figure 6.2 shows spectroscopy of ^{133}Cs about the repumper transition, where the frequency is relative to the $F = 3 \rightarrow F' = 4$ transition. The dual frequency data is taken with another laser 365MHz below the $F = 4 \rightarrow F' = 5$ on the ^{133}Cs D_2 line. As can clearly be seen, the sub-Doppler features are far stronger when the cooler light is present.

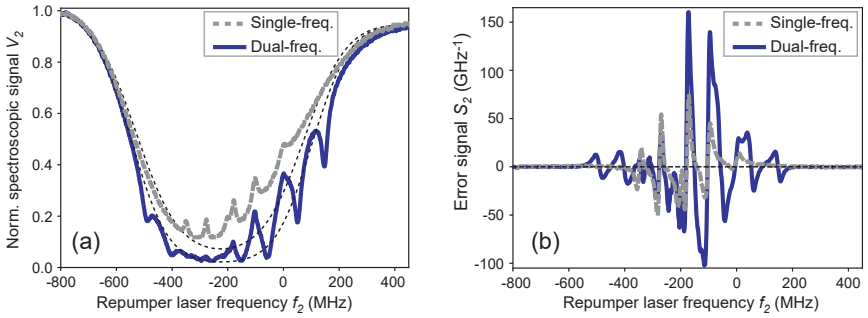

Figure 6.2: a) Output of the Cs repumper photodiode, both with and without cooler light. b) Calculated error signal from a. Frequencies are taken relative to the $F = 3 \rightarrow F' = 4$ transition. The black dashed lines are the Doppler valleys without sub-Doppler features.

To calculate the error signal, first the spectroscopy is normalised against the Doppler valley (black dashed lines in Figure 6.2a) leaving only the sub Doppler features. This is then differentiated with respect to the laser frequency to find the error signal. We see that the error signal is 'sharper', meaning a larger gradient where the errors signal passes through zero, which as explained in section 3.1.1 are generally used as the 'lock points' for the laser. There are also more of these lock points for the dual frequency data, spread over a larger frequency range, demonstrating greater flexibility over which frequency to lock the laser to. A similar procedure is used with ^{85}Rb, as shown in Figure 6.3.

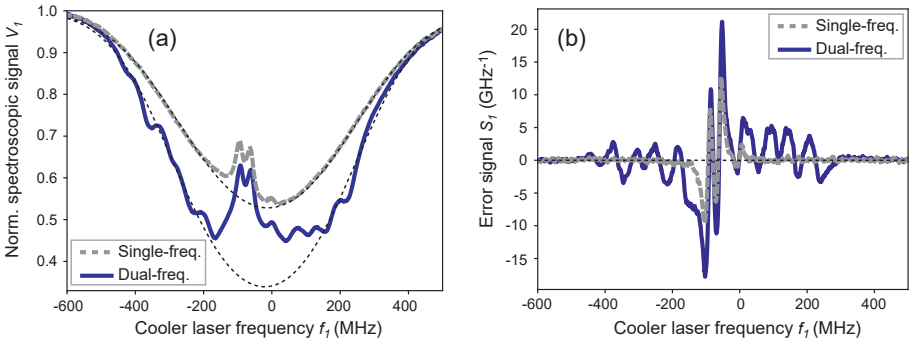

Figure 6.3: a) Output of the Rb cooler photodiode, with and without repumper light on the $F = 2 \rightarrow F' = 3$ transition. b) Error signal calculated from a. Frequencies are taken relative to the $F = 3 \rightarrow F' = 4$ transition.

A more general, but complex, picture can be obtained by plotting the voltage outputs of the cooler and repumper photodiodes against the frequencies of both lasers. Data was taken using a Borosilicate Thorlabs vapour cell at 298 K. The beam diameters are 1.25 mm for both, with 0.14 mW cooler light and 0.23 mW repumper light. Using ^{133}Cs, a colour map depicting this can be shown in Figure 6.4a and Figure 6.5b. Data was taken by simultaneously ramping the current supply to both laser diodes and the voltage supply to the piezoelectric transducers to control the alignment of the diffraction grating which control the feedback for both ECDLs. This results in simultaneously scanning both frequencies, so that data is taken along a diagonal line in Figures 6.4a and Figure 6.5a, hence the grey triangles where no data was taken. Figure 6.2 is simply a slice through Figure 6.5 a with the cooler laser 365MHz below the $F = 4 \rightarrow F' = 5$ transition. The overall features in the graph can be explained by the following model. The absorption of light by the atoms is enhanced when each laser is at the cooler and repumper transition respectively. For slopes with a positive gradient, this is where the lasers are co-propagating and have a fixed frequency difference, as the lasers are both Doppler shifted by the same amount as they address atoms with the same velocity. Along the slope, the two lasers address different velocity groups, and so again the lasers are shifted by the same amount, although different to the previous velocity group. For slopes with negative gradient, the effect is the same but for counter propagating lasers. There are multiple slopes as there are multiple closed cycles, for example to either $F' = 3$ or $F' = 4$. A simplified model using the optical Bloch equations along with a rate equation model is used to find the steady state populations of ^{133}Cs, from which the expected absorption can be derived. This theoretical model is shown in Figure 6.4b and Figure 6.5b. A more thorough explanation of the model with a derivation can be found in [61]. Preliminary data for ^{85}Rb is shown in Figure 6.6. The theoretical model was not applied for Rubidium as the Caesium data seemed more interesting, and so was the focus of our efforts.

The overarching conclusions would be the same, however.

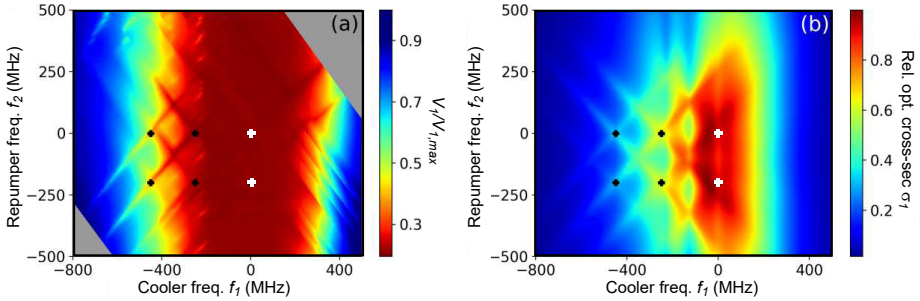

Figure 6.4: a) Output of the ^{133}Cs cooler photodiode, as a function of the cooler and repumper frequencies. Cooler frequencies are taken relative to the $F = 4 \rightarrow F' = 5$ transition, and repumper frequencies are taken relative to the $F = 3 \rightarrow F' = 4$ transition. b) Rate equation model output. The '+' symbol represents points where both lasers are on transition with stationary atoms. White pluses are cycling transitions that do not influence the absorption of the other laser.

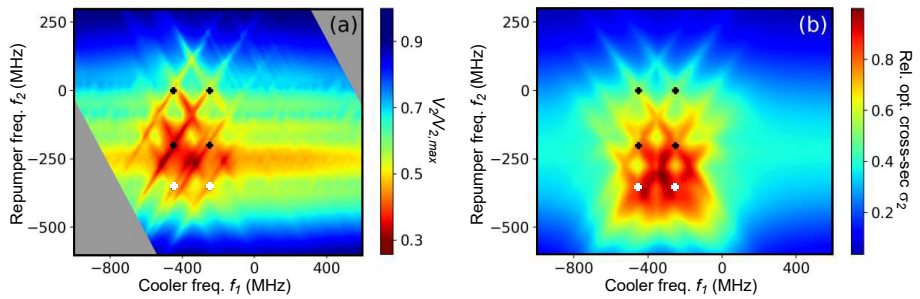

Figure 6.5: a) Output of the ^{133}Cs repumper photodiode, as a function of the cooler and repumper frequencies. b) Rate equation model output

Locking the lasers to analyse the frequency stabilisation is not trivial, as in general the lockpoint of each laser is influenced by the frequency of the other. As such, the lasers must be simultaneously locked, and care must be taken when taking spectroscopy data. It is significantly easier to lock the lasers when this interdependence is not present, and it is possible to find points where the error signal is independent of the frequency of the other laser, i.e.

$$\frac{\partial^2 V_1}{\partial f_1 \partial f_2} = \frac{\partial^2 V_2}{\partial f_1 \partial f_2} = 0. \tag{6.1}$$

For this condition it is sufficient, but not necessary, to have a maxima or minima for the photodiode outputs at the same frequency. These points are marked by black pluses in Figures 6.4 and 6.5.

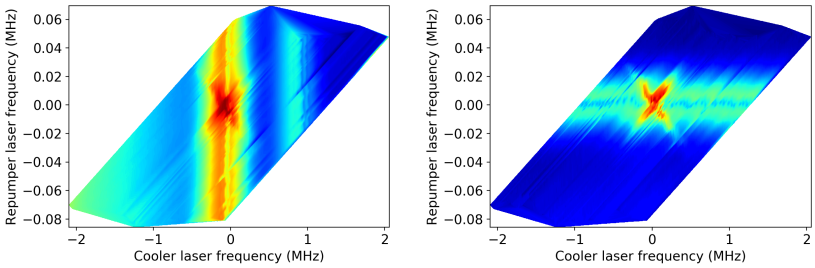

Figure 6.6: Left: Output of the cooler photodiode using dual frequency Rubidium. Right: Output of the repumper photodiode using dual frequency Rubidium.

6.1.3 Laser Stability Analysis

To demonstrate the applicability of this method for improved laser stabilisation, we compare the frequency deviation over a range of time scales for both single and dual frequency locked lasers. For this purpose we use Rubidium, as the repumper signal is notoriously poor, and so a significant improvement would be greatly welcome. For dual frequency locking we use the ^{85}Rb $F = 2 \rightarrow F' = 3$ and $F = 3 \rightarrow F' = 3$ transition. This is compared with locking to the $F = 3 \rightarrow F' = 4$ transition and the $F = 2 \rightarrow F = 2 \otimes 3$ transition. The exact same laser frequencies cannot be used, as the required lock points are not present in standard Doppler free spectroscopy.

Each laser is then locked, first without and then with the other laser locked, and the error signal is measured each time for a period of 20 minutes. We then calculate the Allan deviation of the error signal, and can compare the stability of the frequencies of each laser by examining the respective error signals of the repumper and cooler lasers using single frequency and dual frequency locking, to show the relative improvement gained from using dual frequency locking.

To calculate the Allan deviation, the error signal is recorded over a period of approximately 20 minutes. We use such a long measure time compared to the time scales examined due to the data collection rate of the Arduino, and the desire to average over 1 second time intervals requires data significantly longer than this time period. This was recorded using an Arduino and a circuitused to scale the voltage and add or subtract an offset. This is because the Arduino reads an input between a 0-3.3 V and returns a value between 0-1023. The error signal must therefore be scaled to maximise the range of the Arduino reading without clipping at either end.

This output is then divided into segments, and the average of the squares of the differences between segment averages is then calculated. This value is the divided by two and the square root is taken to find the Allan deviation. The segment length is varied to find the Allan deviation for different averaging times. Specifically, if the error signal as a function of time is $x(t)$, then first it is divided evenly into N regions in time space each of length τ, and the average

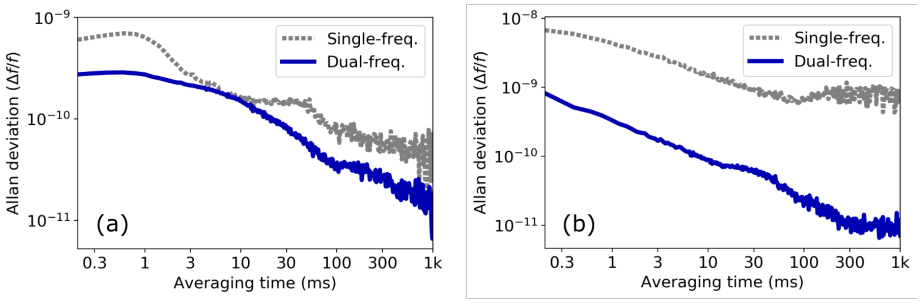

Figure 6.7: a) Allan deviation for the cooler photodiode. b) Allan deviation for the repumper photodiode.

y is calculated for each region. The Allan deviation is then [70]

$$\sigma(\tau) = \sqrt{\frac{N}{N-1}\left(\frac{\sum(y^2)}{N} - \left(\frac{\sum y}{N}\right)^2\right)}, \tag{6.2}$$

where the summation is over all the y values for each region. The Allan deviation as a function of τ can thus be calculated and plotted for the error signals for the dual frequency and single frequency cases, allowing for a direct comparison of frequency stability.

Some calibration factors also needed to be accounted for. The gradient of the error signal about the lock point is needed to be measured in V/MHz, which could be done by comparing to the spectroscopy. This is because we wanted to measure the relative deviation of the error signal, which means we need to normalise for the size of the error signal. We also needed to find the factor for the measurement on the Arduino reading vs the input voltage, which was done by inputting a known linear ramp and comparing to the Arduino measurement, which gives the relative scaling and offset.

The Allan deviations are given in Figure 6.7. It is important to note that the Allan deviation is a measure of the total stability of the laser frequency, and so other noise sources such as temperature fluctuations and electronic noise, are also accounted for. At some average times, these noise sources will dominate, which explains why the Allan deviations are roughly the same for several averaging times. The cooler and repumper lasers also employ distinct hardware, the former being an ECDL and the latter a DFB laser. Thus, the different Allan deviation profiles for the two lasers is to be expected. There will also be limitations imposed by the laser feedback electronics.

We see that for all averaging times the dual frequency method is at least as good as the standard single frequency approach, and indeed is appreciably better for locking the cooler laser for most time scales. Only the cooler for averaging times between 3 and 10 seconds does not see an improvement, but for all other timescales considered the Allan deviation is notably smaller for the dual frequency case, indicating a greater laser stability. The difference is

even more pronounced for the repumper laser, seeing an order of magnitude improvement for nearly all time scales considered. The improvement will likely be better again for the other Alkali metals not studied here, such as Lithium [71], as the upper manifold of the D2 line is poorly resolved. This means that there is no 'cycling transition' for these species, and so optical pumping out of dark states will significantly improve the feedback signal. It is also possible to combine the two photodiode signals in such a way so that the feedback to each laser is, to first order, independent of the frequency of the other laser. This allows for a much wider range of lock points considered here, where we only focused on points where Equation 6.1 is satisfied. Further details can be found in the appendix of [61], and the full paper can be found in the appendix of this thesis.

6.2 3D printed vapour cells

Vapour cells are needed for a range of cold atom experiments for laser stabilisation methods, as discussed in section 3.1, as well as sensors using atom photon interactions [5, 72]. A particular application is use in Spin Exchange Relaxation Free (SERF) magnetometers [73–75], which require measuring the dependence of energy levels of an alkali gas, such as Caesium, on the surrounding magnetic field. The Zeeman shift, and thus the scalar magnetic field, can be measured from the relative absorption of an incoming laser.

Such a system requires a vapour cell to hold the alkali gas. Some applications require the cell to be small in shape [76–79], whilst still requiring resistance to reactive alkali gases. Such cells are usually gas blown, which can be expensive and places restrictions on the shape and size of the cell that can be used. We have previously mentioned that reducing size whilst not sacrificing stability is an important consideration when transferring cold atom techniques from the lab to real world applications. As such, an alternative method examined here is using 3D printing via stereo-lithography, the first 3D printed vapour cell in the world. The vapour cell was designed and manufactured by in the engineering department and passed to us for testing its capabilities and to what extent it could be used in cold atom experiments. 3D printed vapour cells could replace glass blown cells particularly in applications which require small or unusual shapes, where the flexibility of 3D printing can offer the most benefits [80–84].

6.2.1 Spectroscopy

The development of the vapour cell was an iterative process, wherein the engineering department would manufacture the cell and then pass it to us for testing. Feedback provided by our tests allow for the rapid development in the optical quality of the cell, to the point it could be used for laser locking. The final cell had a transmission ratio $> 90\%$ with no Rb vapour at 780 nm. The 'walls' of the cell are only 1 mm thick. Such a small thickness improves the optical quality of the cell, but tests need to be made to ensure that leaks are

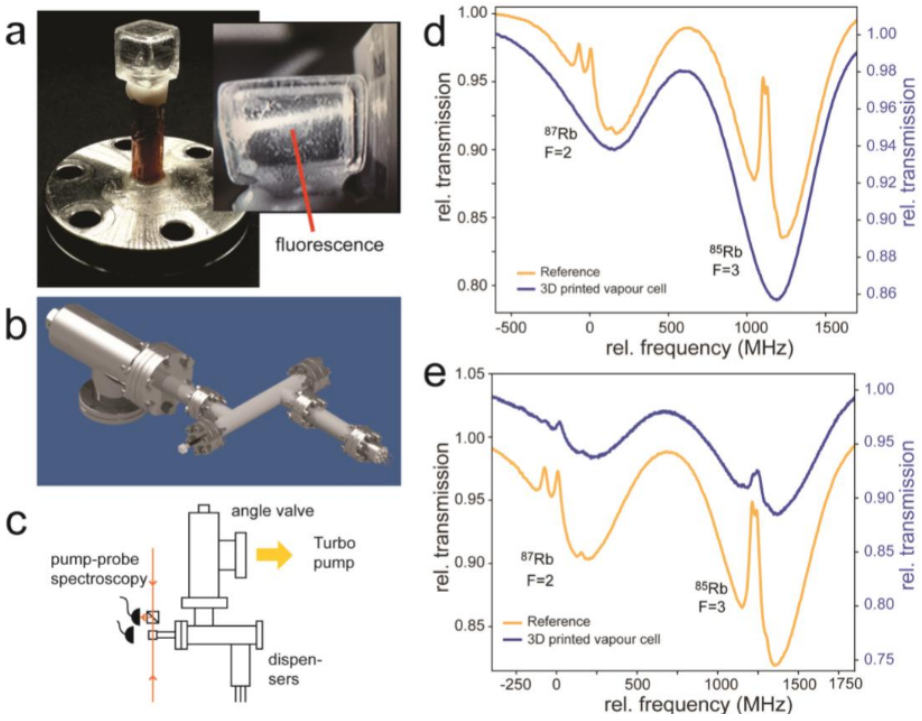

Figure 6.8: a) Vapour cell mounted on copper tube, with fluorescence shown in the inset. b) CAD model of the vacuum system. c) Diagram showing the vapour cell mounted on the vacuum system and the laser set up for Doppler free spectroscopy. d) Single beam spectroscopy through the vapour cell. Reference is vertically offset by 0.02 for clarity. e) Doppler free spectroscopy through the vapour cell. Reference is vertically offset by -0.05 for clarity.

not caused from the thinness of the wall. Details of the manufacturing process are shown here [62] and in the appendix. There are a few different ways to test the quality and usefulness of the cell. The most obvious way of testing the quality of these cells was if these cells could be used in Doppler free spectroscopy locking. The method has already been discussed in section 3.1, and we will use a similar setup as in Figure 3.1, but replacing the standard vapour cell with the printed vapour cell.

To test the cell in this way, we needed to pump out the air inside the cell and replace it with Rubidium. The vapour cell was attached to a copper flange, using UV curing glue, which in turn was attached to a vacuum system shown in 6.8a-c. A turbo pump and 24h bake out at 150 Celsius allowed a pressure of 2×10^{-9} mbar to be achieved. Rubidium dispensers were then activated to fill the cell with Rubidium. These dispensers consist of a Rubidium alloy that releases Rubidium vapour when a 3A current is passed through the dispensers. The dispensers were also left at a high temperature to encourage the Rubidium to migrate to the cell, where the temperature, and thus pressure, was lower. Alternative filling methods are also possible [85, 86]. The cell showed no sign of degradation from exposure to high temperature Rubidium vapour, an important quality. This demonstrates the cell is vacuum compatible despite the thin cell wall, and is capable of storing high temperature alkali vapour, which would apply to any cell manufactured using this method. We can thus infer that a 3D printed cell of virtually any design would thus also have these two key properties.

Initially, a beam with a diameter of 1.25 mm and power 0.06 mW was sent longitudinally along the vacuum chamber, as this exposed the beam to a greater amount of Rubidium. This was to ensure that Rubidium was entering the cell as expected. Spectroscopy from this beam demonstrated that Rubidium was present, but most of this would be in the vacuum chamber and thus not a true test of the vapour cell itself. Then, two counter propagating beams were aligned through the cell to allow for Doppler free spectroscopy, as shown in Figure 6.8c. The probe beam has a power rating of roughly 0.06 mW, and the pump beam 0.3 mW. To measure the spectroscopy signal, we used a Thorlabs DET10 amplified photodiode to measure the beam intensity after the cell. The small powers reflect the small amount of Rubidium trapped in the vapour cell and the short optical path length. The resulting spectroscopy from both one and two beams, and that achieved with a standard 75mm Thorlabs vapour cell, is shown in 6.8d and 6.8e. Doppler free spectroscopy is clearly shown in the blue line in Figure 6.8e. It must be noted that the vapour cell is significantly smaller than the standard vapour cell (7mm vs 75mm), so the weaker spectroscopy does not necessarily reflect the optical properties of the 3D printed vapour cell.

6.2.2 Laser Stability

The laser was then locked using Doppler free spectroscopy locking, as explained in section 3.1.1, using the ^{85}Rb $F = 3 \rightarrow F' = 3 \otimes 4$ crossover transition. The Allan deviation of the error signal was calculated using the method explained in the dual frequency locking section, in order to measure the stability of the system

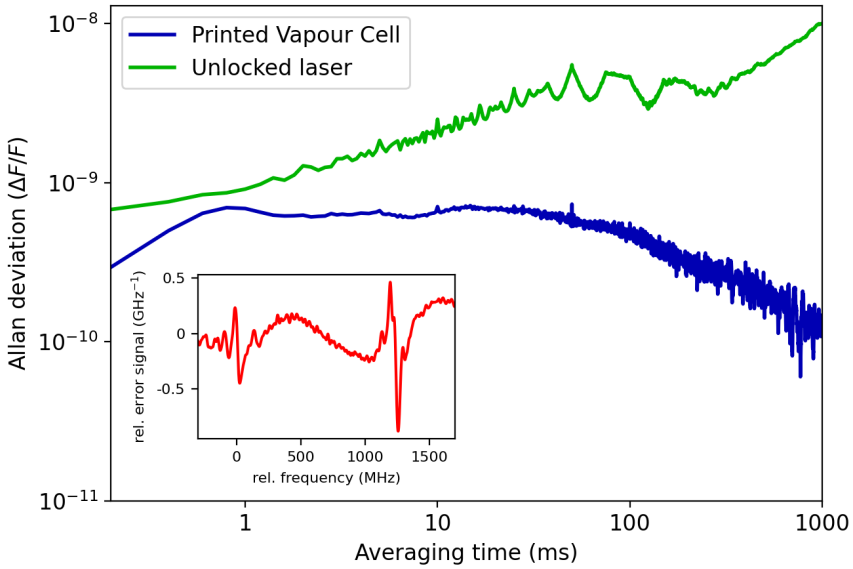

Figure 6.9: The Allan deviation for a range of time scales for both an unlocked laser (Green) and a laser locked using the vapour cell (Blue). The error signal is shown in the inset.

and compare it to a laser locked using a normal cell, as well as compared to the natural stability of the laser itself. Figure 6.9 shows the Allan deviation of the laser locked using the vapour cell, compared to an unlocked laser. A considerable improvement in laser stability is shown across all time scales, approaching 2 orders of magnitude for time scales $\approx$ 1s.

We also seek to compare the printed vapour cell to the standard vapour cell. The laser is again locked to the ^{85}Rb $F = 3 \rightarrow F' = 3 \otimes 4$ crossover transition, using both vapour cells, and the resulting Allan deviations are shown in 6.10. To take into account the differing optical lengths of the two vapour cells, we implement a scaling factor. As each of the cells has a wall thickness $\approx$ 1 mm, the Allan deviation for the standard vapour cell is divided by a factor of $\frac{73}{5} = 14.6$.

Locking the laser using the printed vapour cell offers a clear improvement in frequency stability, compared to the inherent stability of the laser itself. The Allan deviation will measure all sources of noise in the laser locking system, including electronic noise and temperature drifts, and yet the laser is still more stable across a range of time scales from 0.1 ms to 1 s. This suggests the improvement in frequency stability from laser locking is significant enough to account for these extra sources of noise. The fact that the improvement is not the same across all time scales is to be expected, as different noise sources will

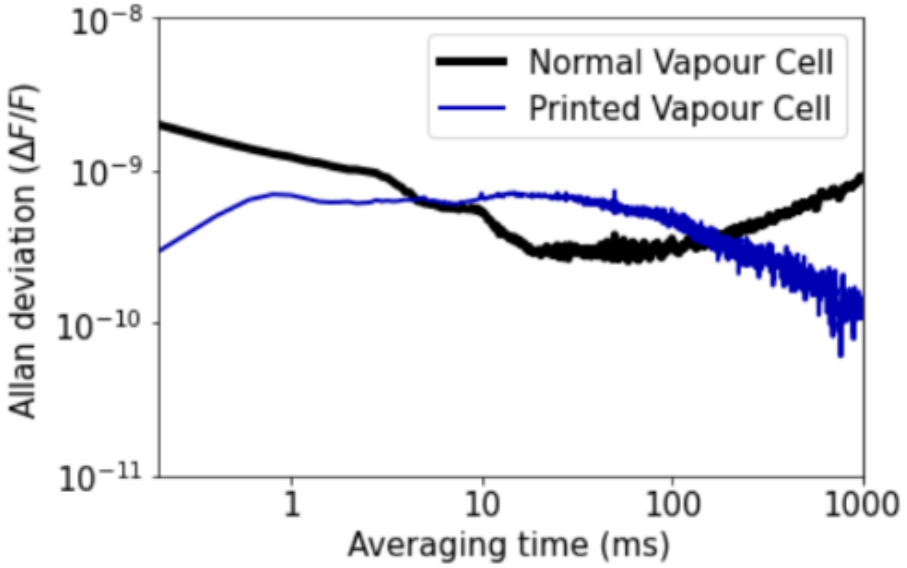

Figure 6.10: Allan deviation of a laser locked to a standard cell (Black) and the 3D printed cell (Blue).

dominate at different time scales. Noise from temperature drifts are expected to dominate at far longer time scales when compared to electronic noise, for example. Laser locking will not account for all of these sources equally, and so there will be difference in improvement for different time scales. Despite this, there is an improvement for all time scales. Even compared to the standard cell, when normalised against optical path length the 3D printed cell is better for a range of time scales. This indicates that the printed vapour cell can indeed be used for applications such as laser locking. The next step would be implementing an experiment using the cell, such as testing the sensitivity of an atomic clock or a magnetometer that uses a 3D printed cell. For comparison, standard SERF magnetometers have demonstrated sensitivities of 5 fT/Hz$^{1/2}$ [19].

6.2.3 Polarisation Analysis

We also sought to characterise the polarisation and optical quality of the cell. This is particularly important in magnetometers and magnetoencephalography, as the strength of the Zeeman effect depends on the polarisation of light considered. A CCD camera was used to view the beam profile with and without the cell, as shown in Figure 6.11a. The beam profile is disturbed only a little, and more along the y - axis than the x - axis, which is along the grain of the cell. This suggests the direction of printing has an effect. To measure the effect of the cell on light polarisation, laser light was shone through a half waveplate onto a polarisation analyser, which measured the azimuth and ellipticity of the light as

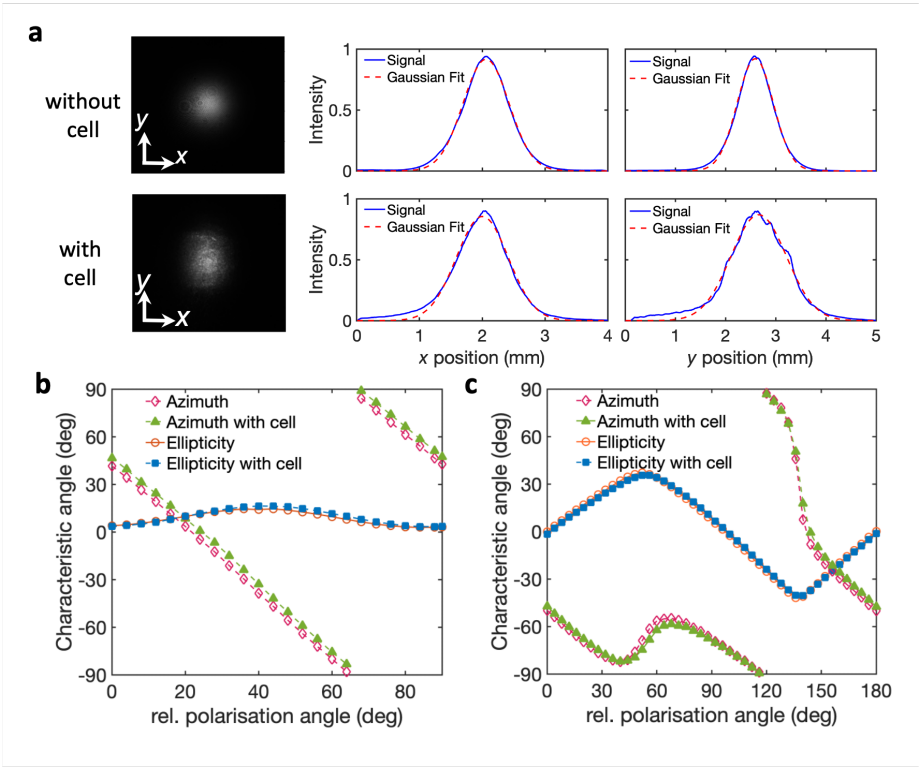

Figure 6.11: a) Effect of the cell on the beam profile. A 780nm beam with a power of 1.2mW was the initial beam, and the output fit a Gaussian shape. This suggests that whilst the cell causes the beam to become divergent, it has only a small effect on the beam profile. b) Effect of the polarisation of the cell on linearly polarised light, compared to no cell. c) Effect of the polarisation of the cell on circularly polarised light, compared to no cell.

the waveplate was rotated. Then the cell was placed between the waveplate and the polarisation analyser, and the data was retaken. The results are shown in Figure 6.11b. This was then repeated using a quarter waveplate instead of a half waveplate, and the data is shown in Figure 6.11c. This was also compared to using a glass plate instead of the vapour cell, shown in Figure 6.12. This data demonstrates that overall the cell has a negligible effect on the polarisation, within the resolution of the polarisation analyser. It was noticed, however, that the cell caused the light to become significantly dispersive afterwards, either due to the roughness of the surface of the cell or some slight curvature of the cell walls creating a lensing effect. This may not be such a big problem as the application intend for a very small optical path length. When taking data for frequency stability and polarisation analysis, the cell was placed very close to the photodiode/polarisation analyser. This could be the focus of future work.

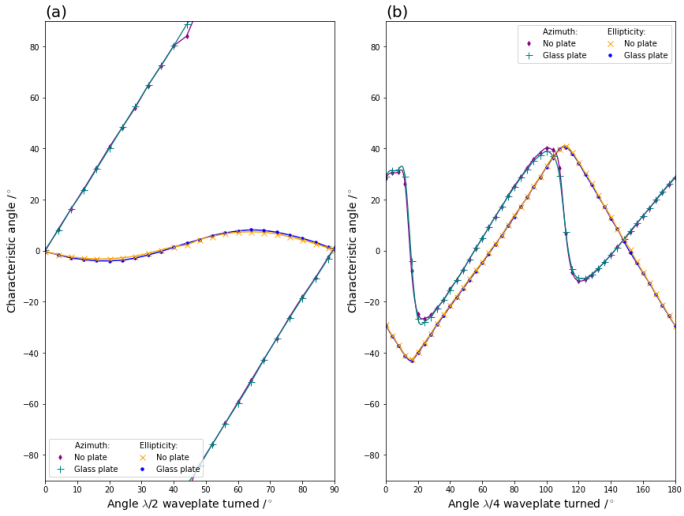

Figure 6.12: a) Linearly polarised light, with and without the glass plate. b) Circularly polarised light, with and without the glass plate.

6.2.4 Conclusion

We have thus demonstrated that a 3D printed cell can be used for laser stabilisation, achieving comparable laser stability to a standard vapour cell of the same length. Thus, the advantages of 3D printing in cost and flexibility can be applied to vapour cells for use on Quantum Technologies. Whilst we have noticed that the surface quality of these cell is rather poor, and that the laser is very dispersive after leaving the cell, the cell is currently useful for certain applications despite imposing restrictions on the layout of the spectroscopy system. Whilst this may not be a significant problem, as applications desire a minimal size and optical path length in any case, it could be the focus of future work. This also highlights a desire to test the cell in other applications, such as its usefulness in a SERF magnetometer. Future work could also examine changing the thickness of the cell wall, and attempting to apply the apparent lensing effect in order to focus the light onto a given detector.

6.3 Surface pump designs

The various applications of cold atom experiments that we have covered so far all require very low pressures ($10^{-9} - 10^{-10}$ mbar), which in general require bulky and power consuming active pumping methods, such as roughing pumps, turbo pumps and ion pumps [87]. For some applications, such as satellite sensors [88], there are significant restrictions on size and power consumption. A potential solution is to use passive 'getter' pumps [89], a chemically reactive material which binds particles in the chamber. This surface pumping is usually insuffient

for the required pressures, and must be activated by baking at high temperatures ($\approx$280^{o}C). Here we examine the pumping rate of this getter material which is used to coat a variety of 3D printed shapes. These shapes have fine details which are difficult to build with standard manufacturing techniques, but are relatively easy to construct using additive manufacturing. Such getter pumps are already in use in some quantum technology applications [90, 91], and so further development of their capabilities will increase their applicability.

The idea is that these 3D printed shapes not only have a larger surface area, they also increase the likely hood that a particle which does not initially react with the material and instead bounces off, will then quickly collide with another section of getter material. This increases the probability of the particle reacting with the getter material, and thus increases the pumping rate. This second effect is particularly important as maximising the number of collisions between the atoms and the getter material is desired. 3D printing a shape which maximises the likely hood of a rebounding particle to collide with another section of the getter material will likely provide the greatest passive pumping rate. Some atomic species are notoriously difficult to pump, such as Helium. Ion pumping is less effective due to Helium's high ionisation energy, its small inertial mass makes turbopumping difficult and its low reactivity with most chemical compounds make getter pumps ineffective. Helium is particularly problematic because it can pass through glass windows in the chamber. Hydrogen is another problematic species. If a 3D printed surface can increase the number of collisions these species have with the getter material, then the pumping rate will increase appreciably.

6.3.1 3D printed surface design

There are a few constraints for these surface coated pumps. The principle method of coating is to use evaporative coating from a single source. To ensure ensure effective coating across the entire surface, therefore, we require there to be direct line of sight from every point on the surface to the inside of the vacuum chamber, with no overhangs. Excessively acute angles can also lead to suboptimal coating, and care must be taken to avoid the formation of air pockets inside the 3D printed layer. These air pockets will greatly reduce the effectiveness of any vacuum pumping method, active or passive. There are also limits to the resolution of the manufacturing process.

We also wish to simulate various designs to reduce the number of samples that need testing, To ease the computational difficulties, we consider only a design made of repeated unit cells with no path for particle to move directly between the cells. Particles can only move from one cell to another via the chamber. If the probability of sticking between an atom of a given species and the getter material is defined as P, then the probability of sticking after n collisions is $1-(1-P)^n$. The atomic species most difficult to remove in this way, and thus those we wish to focus on, will have $P << 1$. Examples of such species are Hydrogen and Helium [92]. For this constraint, the total probability of sticking simplifies to nP. Simulations thus focus on calculating

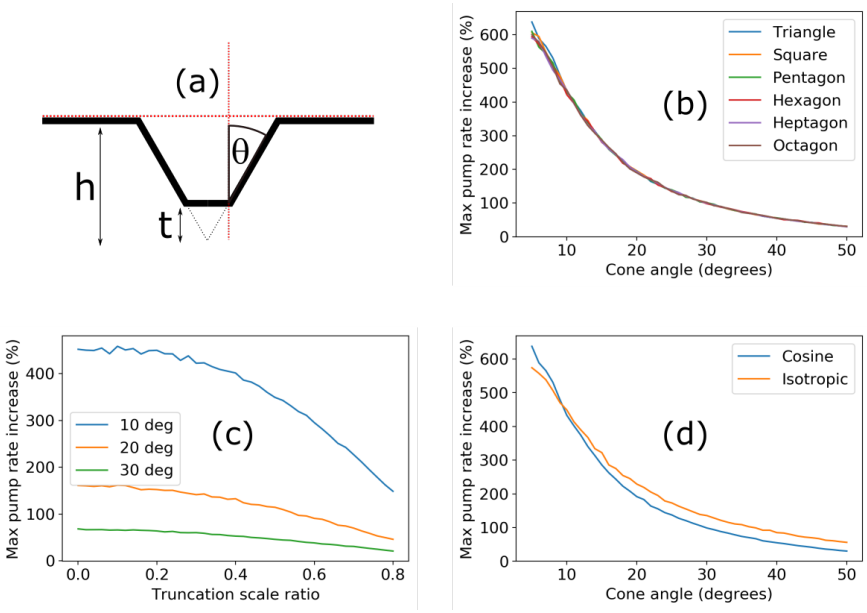

Figure 6.13: a) Shows the design being considered, with h, t and θ being varied. b) Shows the pumping rate for a variety of shapes, and that the shape is irrelevant for the pumping rate. c) Shows the dependence of the pumping rate on θ. d) Examines the difference for a cosine reflection distribution and an isotropic one.

the expectation value of n, given the distribution of angles and velocities of atoms colliding with the getter material. This is repeated for a range of printed designs. The results of these simulations are shown in Figure 6.13

Figure 6.13b shows the shape of the indent is irrelevant, and so we will use a triangular shape for ease of manufacture. Figure 6.13c shows that the angle θ is critical to the effectiveness of the pump. Manufacturing limitations and a desire to prevent air pockets forming in the corner means θ is limited to 20^o. The truncation scale ratio is given by t/h. Figure 6.13d examines the effect of the distribution of angles of atoms that are reflected from the surface. 3D printing introduces some surface roughness to the design, which will effect how the atoms reflect of the surface. To model this, simulations are taken assuming a cosine distribution, which would model a perfectly smooth getter material, and an isotropic distribution, which would occur if the local roughness was such that the atoms are reflected at a random angle. These are the two extreme possibilities with regards to the relevance of the local roughness, and so it is expected the true result will be somewhere in between.

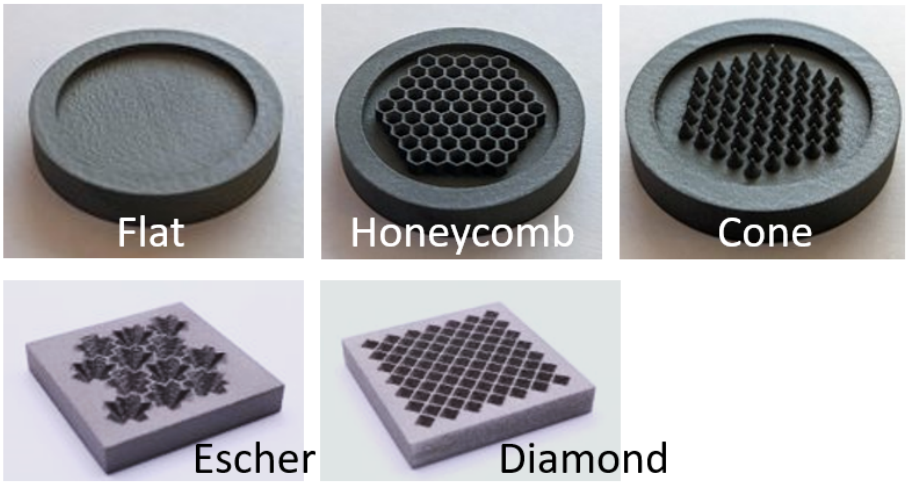

Figure 6.14: The 3D printed samples used for testing. The first three samples are the ones tested, with the other two demonstrating the more complex designs possible.

6.3.2 Pumping rate measurements

From these simulations, 3 different printed designs were tested: flat, to use as a background, as well as a honeycomb shape and a hexagonal array of cones to form a 'spikey' surface. These surfaces were evaporatively coated with a V-Zr-Ti Non Evaporable Getter (NEG) coating. The samples are shown in 6.14. Additionally, a flat stainless steel flange with no NEG coating was also tested, to be used as the baseline which the other samples could be referenced to.

To take data on the effectiveness of these samples, we placed each sample inside a vacuum chamber and turbopumped the chamber, shown in Figure 6.15. A Pfeiffer IKR 270 Compact Cold Cathode Gauge was used to measure the pressure to ensure there were no leaks at this stage. The chamber was then baked at 150^o for 3 days, to remove dirt and moisture inside the vacuum chamber, and then the temperature was again increased to 280^o and held at this temperature for 2 days to activate the NEG. This activation of the NEG must be done for the NEG to work properly. The temperature was then slowly decreased until it reached room temperature. Throughout this process, care is taken to avoid heating or cooling the chamber too quickly, as otherwise the expanding and contracting metal could cause leaks to form. At this point, the pressure had fallen to $\approx 10^{-9}$ mbar.

The pressure gauge was then read into a Python script, and the valve between the sample and the pump was then closed. Closing the valve kicked off a significant amount of particles inside the chamber, so the effectiveness of each sample could be compared by seeing how quickly the pressure fell for each sam-

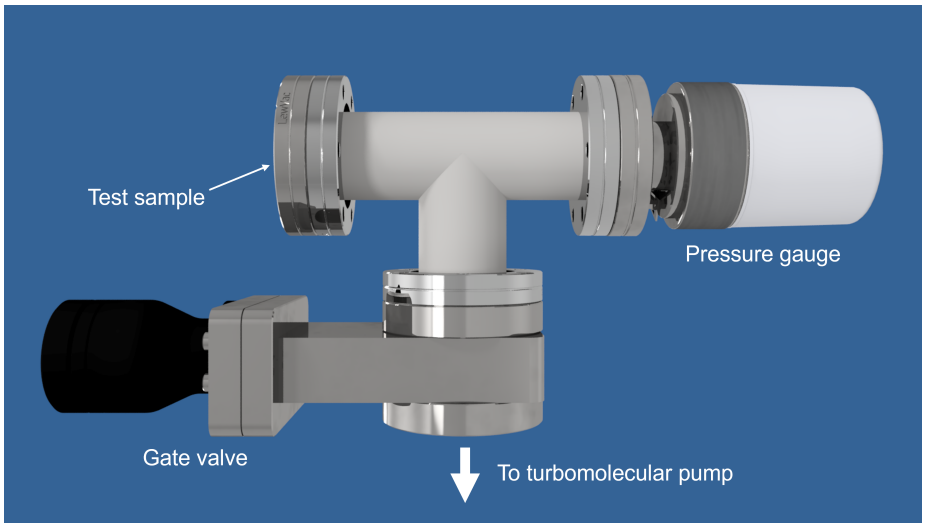

Figure 6.15: Setup used to test the pumping rate of the sample. The valve is closed before each measurement is taken.

ple. The pressure was recorded for a twelve hour period over night, to ensure there were no temperature changes from people being in the room. The pressure gauge has several different pressure regimes, wherein different measurement methods are used. This can clearly be seen in Figure 6.16 as the data for all samples undergoes a sudden pressure drop at $\approx 5 \times 10^{-6}$ mbar, indicating that at this pressure the measurement method changes.

As a result of these factors, the first step to process the data is to offset all the data such that for all samples, $t = 0$ when the pressure falls below 10^{-5} mbar. Then, the gradient of each sample was measured for each pressure value (instead of time), so that the pumping rate as a function of pressure could be calculated. Finally, the pumping rate as a function of pressure for the flat uncoated sample is subtracted from all other data sets. This removes all other sources of outgassing, ensuring that any remaining pumping is due to the NEG. Each data set is then fitted to a linear plot, so that the relative pumping rates for each sample can be compared. This is shown in Figure 6.17. For clarity, the data shown has been smoothed with a rolling average, but all calculations are done without this.

By comparing the gradients of the spikey and honeycomb samples to the flat NEG coated sample, we can find the relative improvement of the printed samples over the flat sample. We find the relative gradients are - spikey: 2.964 ± 0.087 (blue) and 3.061 ± 0.089 (purple); and honeycomb: 2.269 ± 0.073 (green). The two spikey samples both show a relative gradient of 3, within the measurement error. This matches remarkably well with the theoretical predictions in Figure 6.13, which predicted a maximum pumping rate increase of 200% for $\theta = 20^o$. Whilst this suggests that the spikey is approximately the best possible according

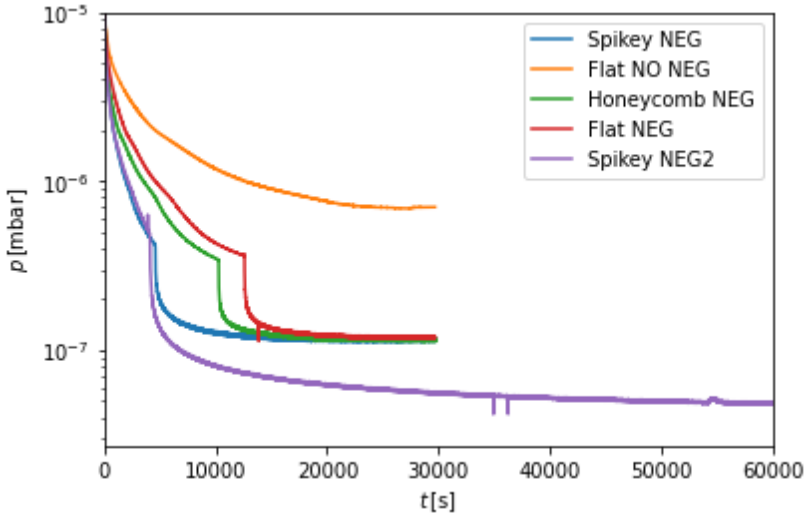

Figure 6.16: Raw data of the measured pressure of each sample over time. The drop in pressure at $\approx 5 \times 10^{-6}$ mbar is where the pressure gauge changes measurement methods.

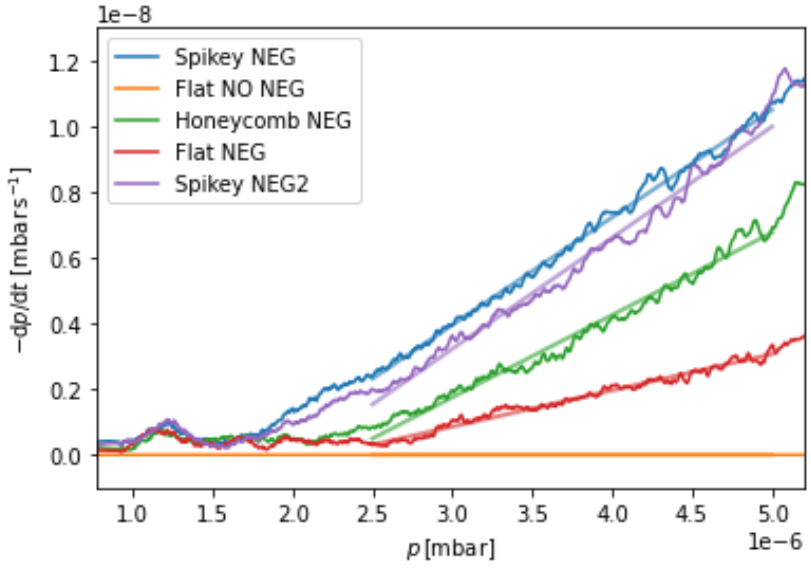

Figure 6.17: Calculated outgassing rate as a function of vacuum pressure for each sample.

to these simulations, the simulations are limited to shapes that use a repeating unit cell. It is therefore possible that even greater improvements are possible for more esoteric shapes, such as the Escher design in Figure 6.14.

6.4 Concluding remarks

These projects have demonstrated techniques aimed towards the wider deployment of quantum technologies. We have shown how dual frequency locking allows for greater laser frequency stability using fewer optical components, offering distinct advantages for cold atom applications outside of lab conditions. Developing a circuit that can separate the frequency dependence of the output diodes will make this far easier to use for general applications. 3D printed vapour cells offer many advantages in applications where small or unorthodox vapour cell design is necessary, such as magnetoencephalography. By demonstrating the applicability of such novel cells for laser frequency stabilisation, the door is open to new designs of magnetometers which take advantage of the flexibility of these cells. Finally, having demonstrated the improvement offered by coating 3D printed designs with NEGs, we propose that a 3D printed chamber which incorporated this would potentially allow for long term vacuum stability without the need for active pumping methods.

Chapter 7

Conclusion and Outlook

Over the course of the five projects I have worked on during my PhD, there have been a range of different techniques applied in order to achieve the desired results. Whilst there are a common set of methods for certain things, such as for laser frequency stability, the range of projects often had very different requirements. There is very little in common in the specific details of each project, but all of them had the general goal of further development of Quantum Technologies.

The ErBeStA experiment for demonstrated EIT in a waveguide chip is by far the most complex of the experiments, and the only one with significant work and data collection before I started. Whilst the majority of the experiment was thus already built beforehand, during my time on the project significant parts did need rebuilding, in particular with regards to laser stability. This experiment is very much a work in progress, as since I left the experiment there has been a direct measurement of the photon delay inside the atom cloud, measured to be approximately 15 ns. Beyond this, there is a desire to further improve the EIT signal by reducing noise and sources of broadening, and also attempting to further reduce the photon group velocity. Additionally, this experiment has been used to investigate Bayesian meteorology techniques to reduce uncertainty in the measurement of optical depth.

For the multi–frequency experiment, progress remains fairly quick (for a cold atoms experiment). We have demonstrated a multi–frequency MOT with an improved atom number, although the improvement is not yet a good as we would like. We are hopeful that further tweaks to the frequency comb generator will yield the desired increase in atom number. We also see a significant improvement in loading rate, as expected. Next steps are to use axicons to create a dark spot MOT to reduce collisional losses in order to see the maximum improvement from the multi–frequency light. In the long term, we also intend to introduce a Dipole Trap in order to use evaporative cooling to create a BEC, which could be used to test various theories of quantum gravity. This latter aim will likely require a new chamber with more powerful lasers, so that a larger beam diameter can be used to trap even higher atom numbers.

The smaller projects were far less time consuming to complete and done so whilst also working on the multi–frequency MOT experiment. Work was done on these experiments when time permitted on the multi frequency experiment, such as when a given process only required one person. The dual frequency experiment was particularly time consuming for data collection, as whilst the experiment did not require our direct involvement during data collection, being largely automated, we could not work on the optical bench during this as it would effect the results of the stability measurement. Whilst this project did demonstrate an improvement in laser stability whilst reducing the amount of optical components, the process of simultaneous laser locking is tedious and generally requires two people to ensure the lasers are locked simultaneously. Thus we do not use this technique in the rest of our experiments. If the error signals for the two lasers could be separated using electronic processing, then it would make the process easier to implement.

The 3D printed vapour cell was more successful as the cell was successfully used in laser stabilisation despite a significantly smaller optical path length. The 3D printed cell thus did not disrupt the laser significantly enough to effect the laser locking feedback loop. There is currently the hope of implementing a commercial application soon, and in the meantime the aim is to further improve the optical quality of the cell by refining the manufacturing process, as well as testing novel vapour cell shapes.

The NEG coated 3D printed surfaces demonstrated a three-fold increase in pumping rate compared to a flat coated surface, proving that the benefit of this approach is significant. The next step will be to test whether a vacuum chamber can be pumed sufficiently by these NEGs to demonstrate a MOT. The best approach would be to additively manufacture a specialised vacuum chamber with the inside covered in cones. The inside surface could be then coated with the NEG, and used to test the vacuum stability using only these passive pumps. Active pumping systems would still be needed to reduce the pressure sufficiently that the NEGs could be activated. The chamber could also have heating tubes throughout the structure, through which hot air could be blown to ensure the NEGs were activated.

In conclusion the wide range of projects I have worked on have given me significant insight into a variety of experimental techniques in the field of cold atom physics and their applications towards the development of Quantum Technologies. The smaller project are, by their nature, likely to be implemented more quickly in other applications, in particularly where size and weight are at a premium. The surface passive pumps are already planned to be used on satellite based cold atom experiments and sensors, whilst the 3D printed cells are likely to be used in improved magnetoencephalography sensors. The larger projects are still in the development and data collection phase, but both experiments have already produced promising results. Demonstrating EIT in a wave–guide chip would open up development of quantum computers using Dipole arrays to hold multiple Dipole traps with either a single or multiple fibres, the architecture of which would depend on the desired application. This setup is far easier to scale up than current approached based on Rydberg atoms. For the multi

frequency MOT, success would allow for significantly more precise cold atom sensors, which would not only have implications for fields that currently rely on cold atom sensors, but also make these sensors useful for new applications, such as tests of fundamental physics.

Bibliography

[1]E. Raab, M. Prentiss, A. Cable, S. Chu, and D. E. Pritchard, "Trapping of neutral sodium atoms with radiation pressure", Phys. Rev. Lett. **59**, 2631 (1987).

[2]R. Howl, N. Cooper, and L. Hackermüller, "Gravitationally-induced entanglement in cold atoms", arXiv 2304.00734, 10.48550/arXiv.2304.00734 (2023).

[3]M. Fleischhaur, A. Imamoglu, and J. Marangos, "Electromagnetically induced transparency: optics in coherent media", Rev. Mod. Phys. **77** (2005).

[4]I. Beterov, "Quantum computers based on cold atoms", Springer **56**, 317–324 (2021).

[5]H. Haffner, C. Roos, and R. Blatt, "Quantum computing with trapped ions", Physics Reports **469**, 155–203 (2008).

[6]M. Nielsen and I. Chuang, *Quantum computation and quantum information, 2nd edition* (Cambridge University Press, 2010).

[7]M. Amico, Z. H. Saleem, and M. Kumph, "Experimental study of shor's factoring algorithm using the ibm q experience", Physical Review A **100**, 10.1103/physreva.100.012305 (2019).

[8]G. Lepert, M. Trupke, M. J. Hartmann, M. B. Plenio, and E. A. Hinds, "Arrays of waveguide-coupled optical cavities that interact strongly with atoms", New Journal of Physics 13, 113002, 10.1088/1367-2630/13/11/113002 (2011).

[9]J. Lee, D. H. Park, S. Mittal, M. Dagenais, and S. L. Rolston, "Integrated optical dipole trap for cold neutral atoms with an optical waveguide coupler", New Journal of Physics 15, 043010, 10.1088/1367-2630/15/4/043010 (2013).

[10]R. Kumar, V. Gokhroo, and N. C. Síle, "Multi-level cascaded electromagnetically induced transparency in cold atoms using an optical nanofibre interface", New Journal of Physics, 17(12), 10.1088/1367-2630/17/12/123012 (2015).

[11]W. Liu, H. Li, C. Li, J. Ding, Y. Luo, W. Wu, M. Guo, W. Hong, and L. Huang, "Simultaneous realization of electromagnetically induced transparency and electromagnetically induced reflectance in a metasurface", Opt. Express **29**, 12580–12589 (2021).

[12]M. Han, H. Hao, X. Song, Z. Yin, M. Parniak, Z. Jia, and Y. Peng, "Microwave electrometry with bichromatic electromagnetically induced transparency in rydberg atoms", EPJ Quantum Technology, 10, 28., https://doi.org/10.1140/epjqt/s40507-023-00184-z (2023).

[13]W. Li, D. Viscor, S. Hofferberth, and I. Lesanovsky, "Electromagnetically induced transparency in an entangled medium", Phys. Rev. Lett. **112**, 243601 (2014).

[14]M. Bajcsy, S. Hofferberth, V. Balic, T. Peyronel, M. Hafezi, A. S. Zibrov, V. Vuletic, and M. D. Lukin, "Efficient all-optical switching using slow light within a hollow fiber", Phys. Rev. Lett. **102**, 203902 (2009).

[15]M. J. Renn, D. Montgomery, D. Z. A. O. Vdovin, C. E. Wieman, and E. A. Cornell, "Laser-guided atoms in hollow-core optical fibers", Phys. Rev. Lett. **75** (1995).

[16]M. Kohnen, M. Succo, P. G. Petrov, R. A. Nyman, M. Trupke, and E. A. Hinds, "An array of integrated atom-photon junctions", Nature Photonics 5, 35–38, 10.1038/nphoton.2010.255 (2010).

[17]D. Fahey and M. Noel, "Excitation of rydberg states in rubidium with near infrared diode lasers", Optics Express **19**, 17002 (2011).

[18]S. R. Cohen and J. D. Thompson, "Quantum computing with circular rydberg atoms", eng, PRX quantum **2**, 030322 (2021).

[19]S. K. W. Clark Griffith and J. Kitching, "Femtotesla atomic magnetometry in a microfabricated vapor cell", Optics Express **18**, 27167–27172 (2010).

[20]Y. Bidel, O. Carraz, R. Charriere, M. Cadoret, N. Zahzam, and A. Bresson, "Compact cold atom gravimeter for field applications", Appl. Phys. Lett. **102**, 144107 (2013).

[21]V. Menoret, P. Vermeulen, N. Le Moigne, S. Bonvalot, P. Bouyer, A. Landragin, and B. Desruelle, "Gravity measurements below 10^{-9} g with a transportable absolute quantum gravimeter", Sci. Rep. **8**, 12300 (2018).

[22]B. Schrinski, P. Haslinger, J. Schmiedmayer, K. Hornberger, and S. Nimmrichter, "Testing collapse models with bose-einstein-condensate interferometry", Phys. Rev. A **107**, 043320 (2023).

[23]A. G. Sinclair, E. Riis, and M. J. Snadden, "Improved trapping in a vapor-cell magneto-optical trap with multiple laser frequencies", Journal of the Optical Society of America B **11**, 2333–2339 (1994).

[24]C. Qiang, L. Xin-Yu, G. Kui-Yi, W. Xiao-Rui, C. Dong-Min, and W. Ru-Quan, "Improved atom number with a dual color magneto—optical trap", Chinese Phys. B **21**, 10.1088/1674-1056/21/4/043203 (2012).

[25]D. A. Steck, *Rubidium 85 d line data*, 2023.

[26]D. A. Steck, *Caesium d line data*, 2023.

[27]D. A. Steck, *Rubidium 87 d line data*, 2023.

[28]C. J. Foot, *Atomic physics* (Oxford University Press, 2005).

[29]L. Salasnich, *Quantum physics of light and matter. a modern introduction to photons, atoms and many-body systems* (Springer, 2014).

[30]E. D. Ros, "Integrating cold caesium atoms into optical waveguides", PhD thesis (University of Nottingham, 2020).

[31]H. Metcalf and P. Straten, *Laser cooling and trapping* (Springer, 1999).

[32]P. D. Lett, R. N. Watts, C. I. Westbrook, W. D. Phillips, P. L. Gould, and H. J. Metcalf, "Observation of atoms laser cooled below the doppler limit", Phys. Rev. Lett. **61**, 169–172 (1988).

[33]J. Dalibard and C. Cohen-Tannoudji, "Laser cooling below the doppler limit by polarization gradients: simple theoretical models", J. Opt. Soc. Am. B **6**, 2023–2045 (1989).

[34]M. W. R. Grimm and Y. B. Ovchinnikov, "Optical dipole traps for neutral atoms", vol. 42. Advances In Atomic, Molecular, and Optical Physics (2000).

[35]Y. Wu, B. Sun, and X. Li, "Semiconductor laser active frequency stabilization technologies: a review", Journal of the Korean Physical Society **79**, 795–809 (2021).

[36]RP Photonics Encyclopedia, https://www.rp-photonics.com/externa_cavity_diode_lasers.html.

[37]D. W. Preston, "Doppler-free saturated absorption: laser spectroscopy", Am. J. Phys. **64**, 1432–1436 (1996).

[38]W. Demtröder, *Laser spectroscopy* (Springer Berlin, Heidelberg, 2008).

[39]M. Hafiz, G. Coget, E. Clercq, and R. Boudot, "Doppler-free spectroscopy on the Cs D1 line with a dual-frequency laser", Opt. Lett. **41**, 2982 (2016).

[40]M. Hafiz, D. Brazhnikov, G. Coget, A. Taichenachev, V. Yudin, E. Clercq, and R. Boudot, "High-contrast sub-Doppler absorption spikes in a hot atomic vapor cell exposed to a dual-frequency laser field", New J. Phys. **19**, 073028 (2017).

[41]D. Brazhnikov, S. Ignatovic, I. Mesenzova, A. Mikhailov, R. Boudot, and M. Skortsov, "Two-frequency sub-Doppler spectroscopy of the caesium D1 line in various configurations of counterpropagating laser beams", Quantum Electron. **50**, 1015 (2020).

[42]M. Zhao, X. Jiang, R. Fang, Y. Qiu, Z. Ma, C. Han, B. Lu, and C. Lee, "Laser frequency stabilization via bichromatic Doppler-free spectroscopy of an ^{87}Rb D1 line", Appl. Opt. **60**, 5203 (2021).

[43]M. Zhao, X. Jiang, R. Fang, Y. Qiu, Z. Ma, C. Han, B. Lu, C. Lee, A. Gusching, M. Petersen, N. Pasilly, D. Brazhnikov, and M. Abdel Hafiz, "Laser frequency stabilization via bichromatic doppler-free spectroscopy of an 87rb d1 line", Appl. Optics **60**, 5203–5207 (2021).

[44]F. Riehle, *Frequency standards: basics and applications* (Wiley-VCH, Weinheim, 2006).

[45]S. Pustelny, V. Schultze, T. Scholtes, and D. Budker, "Dichroic atomic vapor laser lock with multi-gigahertz stabilization range", Arxiv (2016).

[46]A. Paris-Mandoki, "A single apparatus for the production of ultracold fermionic lithium and cold bosonic caesium gases", PhD thesis (University of Nottingham, 2015).

[47]J. Nute, "A quantum integrated light and matter interface", PhD thesis (University of Nottingham, 2017).

[48]S. Warriar, "Towards an ultracold bose-fermi mixture of cesium and lithium atoms", PhD thesis (Univerity of Nottingham, 2014).

[49]M. Jones, "Preparation of cold samples of caesium-133 and lithium-6 in a single apparatus for bose-fermi mixture experiments", PhD thesis (Univerity of Nottingham, 2014).

[50]S. Dürr, K. W. Miller, and C. E. Wieman, "Improved loading of an optical dipole trap by suppression of radiative escape", Phys. Rev. A **63**, 011401 (2000).

[51]G. Li, J. Shang, Y. Ji, L. Lu, and Z. Pan, "Integration of chip-scale serf atomic magnetometers for magnetoencephalography measurement", in 2018 ieee 68th electronic components and technology conference (ectc) (2018), pp. 802–807.

[52]J. Metcalf and P. Van der Straten, "Laser cooling and trapping of atoms", Journal of the Optical Society of America. B, Optical physics 20.5 (2003).

[53]S. A. Diddams, "The evolving optical frequency comb", Journal of the Optical Society of America B **27**, 10.1364/JOSAB.27.000B51 (2010).

[54]S. Herr, "Frequency comb up- and down-conversion in synchronously driven (2) optical microresonators", Optics Letters **43**, 10.1364/OL.43.005745 (2018).

[55]P. Milonni and H. Erberly, *Laser physics 2ed* (John Wiley & sons, 2010).

[56]P. Ehlers, "Further development of nice-ohms", PhD thesis (Umea University, 2014).

[57]P. Knight and I. Walmsley, "UK national quantum technology programme", Quantum Sci. Technol. **4**, 040502 (2019).

[58]K. Bongs, V. Boyer, M. Cruise, A. Freise, M. Holynski, J. Hughes, A. Kaushik, Y.-H. Lien, A. Niggebaum, M. Perea-Ortiz, et al., "The UK national quantum technologies hub in sensors and metrology (keynote paper)", in Quantum optics, Vol. 9900 (International Society for Optics and Photonics, 2016), p. 990009.

[59]S. Madkhaly, L. Coles, C. Morley, C. Colquhoun, M. Fromhold, N. Cooper, and L. Hackermüller, "Performance-optimized components for quantum technologies via additive manufacturing", PRX Quantum **2**, 030326 (2021).

[60]S. Madkhaly, N. Cooper, L. Coles, and L. Hackermüller, "High-performance, additively-manufactured atomic spectroscopy apparatus for portable quantum technologies", Opt. Express. **30**, 25753–25764 (2022).

[61]N. Cooper, S. Madkhaly, D. Johnson, B. Hopton, D. Baldolini, and L. Hackermüller, "Dual-frequency doppler-free spectroscopy for simultaneous laser stabilization in compact atomic physics experiments", Phys. Rev. A **108**, 013521 (2023).

[62]F. Wang, N. Cooper, Y. He, B. Hopton, D. Johnson, P. Zhao, T. M. Fromhold, C. J. Tuck, R. H. R. D. W. andLyudmila Turyanska, and L. Hackermüller, "Additive manufacturing of functionalised atomic vapour cells for next-generation quantum technologies", arXiv:2406.15255 (2024).

[63]I. Georgescu, "25 years of BEC", Nat. Rev. Phys. **2**, 396 (2020).

[64]J. Kitching, S. Knappe, and E. Donley, "Atomic sensors — a review", IEEE Sens. J. **11**, 9 (2011).

[65]K. Tilburg, N. Leefer, L. Bougas, and D. Budker, "Search for ultralight scalar dark matter with atomic spectroscopy", Phys. Rev. Lett. **115**, 011802 (2015).

[66]S. Bize, P. Laurent, M. Abgrall, H. Marion, I. Maksimovic, L. Cacciapuoti, J. Grünert, C. Vian, F. P. Dos Santos, P. Rosenbusch, et al., "Cold atom clocks and applications", J. Phys. B **38**, S449 (2005).

[67]A. Fregosi, C. Gabbanini, S. Gozzini, L. Lenci, C. Marinelli, and A. Fioretti, "Magnetic induction imaging with a cold-atom radio frequency magnetometer", Appl. Phys. Lett. **117**, 144102 (2020).

[68]E. Boto, N. Holmes, J. Legget, G. Roberts, V. Shah, S. Meyer, L. Munoz, K. Mullinger, T. Tierney, Bestmann, et al., "Moving magnetoencephalography towards real-world applications with a wearable system", Nature **555**, 657–661 (2018).

[69]C. Deans, L. Marmugi, and F. Renzoni, "Sub-Sm^{-1} electromagnetic induction imaging with an unshielded atomic magnetometer", Appl. Phys. Lett. **116**, 133501 (2020).

[70]D. W. Allan, ed., *Statistics of atomic frequency standards*, Vol. 54 (1966), pp. 221–230.

[71]M. Gehm, *Properties of* ^{6}*li*, 2003.

[72]N. B. Vilas, C. Hallas, L. Anderegg, P. Robichaud, A. Winnicki, D. Mitra, and J. M. Doyle, "Magneto-optical trapping and sub-doppler cooling of a polyatomic molecule", Nature **606**, 70–74 (2022).

[73]N. Behbood, F. M. Ciurana, G. Colangelo, M. Napolitano, M. W. Mitchell, and R. J. Sewell., "Real-time vector field tracking with a cold-atom magnetometer", Appl. Phys. Lett. **102**, `10.1063/1.4803684` (2013).

[74]V. Schultze, T. Scholtes, R. Ijsselsteijn, and H. Meyer, "Improving the sensitivity of optically pumped magnetometers by hyperfine repumping", JOSA B **32**, 730–736 (2016).

[75]R. Li, C. Perrella, and A. Luiten, "Repumping atomic media for an enhanced sensitivity atomic magnetometer", Optics Express **30**, 31752 (2022).

[76]S. Losev, D. Sevostianov, V. Vassiliev, and V. Velishansky, "Production of miniature glass cells with rubidium for chip scale atomic clock", Phys. Procedia **71**, 242–246 (2015).

[77]Y. Ji, J. Shang, G. Li, J. Zhang, and J. Zhang, "Microfabricated shaped rubidium vapor cell for miniaturized atomic magnetometers", IEEE Sensors Lett. **4**, 2 (2020).

[78]E. Talker, P. Arora, R. Zektzer, Y. Sebbag, M. Dikopltsev, and U. Levy, "Light-induced atomic desorption in microfabricated vapor cells for demonstrating quantum optical applications", Phys. Rev. Appl. **15**, L051001 (2021).

[79]V. G. Lucivero, A. Zanoni, G. Corrielli, R. Osellame, and M. W. Mitchell, "Laser-written vapor cells for chip-scale atomic sensing and spectroscopy", Opt. Express **30**, 27149–27163 (2022).

[80]J. Luo, L. J. Gilbert, C. Qu, R. G. Landers, D. A. Bristow, and E. C. Kinzel, "Additive manufacturing of transparent soda-lime glass using a filament-fed process", Journal of Manufacturing Science and Engineering **139**, 061006 (2017).

[81]C. Inamura, M. Stern, D. Lizardo, P. Houk, and N. Oxman, "Additive manufacturing of transparent glass structures", 3D Printing and Additive Manufacturing **5**, 269–283 (2018).

[82]K. C. Datsiou, E. Saleh, F. Spirrett, R. Goodridge, I. Ashcroft, and D. Eustice, "Additive manufacturing of glass with laser powder bed fusion", Journal of the American Ceramic Society **102**, 4410–4414 (2019).

[83]J. Lei, Y. Hong, Q. Zhang, F. Peng, and H. Xiao, "Additive manufacturing of fused silica glass using direct laser melting", in Cleo: applications and technology (Optica Publishing Group, 2019), AW3I–4.

[84]K. Sasan, A. Lange, T. D. Yee, N. Dudukovic, D. T. Nguyen, M. A. Johnson, O. D. Herrera, J. H. Yoo, A. M. Sawvel, M. E. Ellis, et al., "Additive manufacturing of optical quality germania–silica glasses", ACS applied materials & interfaces **12**, 6736–6741 (2020).

[85]K. Shun, Y. Hirai, O. Tabata, and T. Tsuchiya, "Microfabricated cs vapor cells filled with an on-chip dispensing component", Jpn. J. Appl. Phys. **60**, 10.35848/1347-4065/abe203 (2021).

[86]V. G. Lucivero, A. Zanoni, G. Corrielli, R. Osellame, and M. W. Mitchell, "Laser-written vapor cells for chip-scale atomic sensing and spectroscopy", Opt. Express **30**, 27149–27163 (2022).

[87]P. J. Abbott and Z. J. Jabour, "Vacuum technology considerations for mass metrology", Journal of Research of the National Institute of Standards and Technology **116** (2011).

[88]I. Alonso et al., "Cold atoms in space: community workshop summary and proposed road-map", EPJ Quantum Technology **9**, 10.1140/epjqt/s40507-022-00147-w (2022).

[89]E. Sartori, M. Siragusa, P. Sonato, F. Siviero, M. Mura, E. Maccallini, A. Ferrara, P. Manini, S. Hanke, and C. Day, "Development of non evaporable getter pumps for large hydrogen throughput and capacity in high vacuum regimes", Vacuum **214**, 10.1016/j.vacuum.2023.112198 (2023).

[90]J. A. Rushton, M. Aldous, and M. D. Himsworth, "Contributed review: the feasibility of a fully miniaturized magneto-optical trap for portable ultracold quantum technology", Review of Scientific Instruments **85**, 10.1063/1.4904066 (2014).

[91]D. Sertore, P. Michelato, L. Monaco, P. Manini, and F. Siviero, "Use of non evaporable getter pumps to ensure long term performances of high quantum efficiency photocathodes", Journal of Vacuum Science Technology A **32**, 031602 (2014).

[92]O. Seify, O. B. Malyshev, R. Širvinskaitė, R. Valizadeh, and A. N. Hannah, "Optimisation of the rga location in the evaluation of neg coating pumping properties", Vacuum **195** (2019).

Dual-frequency Doppler-free spectroscopy for simultaneous laser stabilization in compact atomic physics experiments

Nathan Cooper,[1,*] Somaya Madkhaly,[1,2] David Johnson,[1] Benjamin Hopton,[1] Daniele Baldolini,[1] and Lucia Hackermüller[1]
[1]*School of Physics and Astronomy, University of Nottingham, University Park, Nottingham NG7 2RD, United Kingdom*
[2]*Department of Physics, Jazan University, Jazan 45142, Kingdom of Saudi Arabia*

(Received 16 December 2022; revised 9 June 2023; accepted 26 June 2023; published 31 July 2023)

Vapor-cell spectroscopy is an essential technique in many fields and is particularly relevant for quantum technologies. Most atom- and ion-trapping experiments rely on simultaneous spectroscopy of two atomic transitions, employing a separate apparatus for each transition. We demonstrate simultaneous spectroscopy on two atomic transitions, within a single apparatus, using spatially overlapped beams from two independent lasers. This method enables compact setups and offers superior spectroscopic performance, leading to sharper spectroscopy peaks, stronger absorption signals, and superior laser stability. Doppler-free locking features become accessible over a frequency range several hundred megahertz wider than for standard saturated absorption spectroscopy. Exploring the full parameter space associated with dual-frequency spectroscopy reveals a latticelike structure of sharp resonance features, which enhances experimental versatility by allowing laser frequency stabilization within a wide manifold of locations in two-dimensional frequency space. We present data for ^{133}Cs and ^{85}Rb and compare our results to a theoretical model. Employing the technique for frequency stabilization close to the D_2 line of ^{85}Rb results in an improvement in frequency stability by a factor typically between 2 and 3 for averaging times of up to 1 s. The technique will advance portable quantum technologies and facilitate high-precision measurements.

DOI: 10.1103/PhysRevA.108.013521

I. INTRODUCTION

The last decade has seen an explosion of interest in quantum technologies and experiments that exploit the coherent interaction of atoms with frequency-stabilized laser radiation. This includes not only growth in laboratory-based precision experiments [1–3] but also ambitious proposals to test key aspects of fundamental physics using space-based apparatus [4–7] and distributed atomic sensor networks [8]; these rely on precise laser frequency stabilization. At the same time, the quantum technology sector is finding highly important, real-world applications for atomic physics techniques in areas such as subterranean mapping, inertial navigation, and medical imaging [9–14], resulting in the need for compact and robust systems. Typically, at least two independent lasers are required, as light resonant with two different atomic transitions, referred to as the "cooler" and "repumper" transitions, is essential [15].

Herein, we demonstrate simultaneous frequency stabilization of two lasers using a single spectroscopic setup, achieving superior frequency stability compared to standard techniques while at the same time reducing the size and complexity of the required hardware.

Frequency stabilization of lasers for atom-cooling and -trapping experiments is generally achieved via a feedback servo that controls the laser diode current and/or other feedback parameters. The signal used for this feedback is usually generated from spectroscopic measurements on an atomic vapor cell, although a range of other approaches is possible; see [16] for a full review of active laser frequency stabilization. A common technique with atomic vapor is based on saturated absorption spectroscopy [17,18], combined with modulation of the laser current and phase-sensitive detection of the spectroscopic signal [19].

Dual-frequency spectroscopy techniques were previously applied to stabilize lasers for multistep excitation processes [20] and the generation of Rydberg atoms [21], in atomic vapor magnetometry [22,23], and to address atypical atomic transitions [24]. Herein, we show the utility and unique benefits of the approach in the context of laser stabilization for cooling and trapping experiments; variation of both lasers' frequencies opens up a two-dimensional parameter space where optical pumping effects create a lattice of Doppler-free resonance features, offering an expanded set of potential "locking points" at which the lasers' frequencies can be stabilized. We show how two lasers can be stabilized simultaneously, with improved frequency stability, based on the resulting spectroscopic signals. This differs significantly from previous implementations in cooling and trapping experiments, which were based on fixed-frequency modulation of a single laser source [24–27].

*nathan.cooper@nottingham.ac.uk

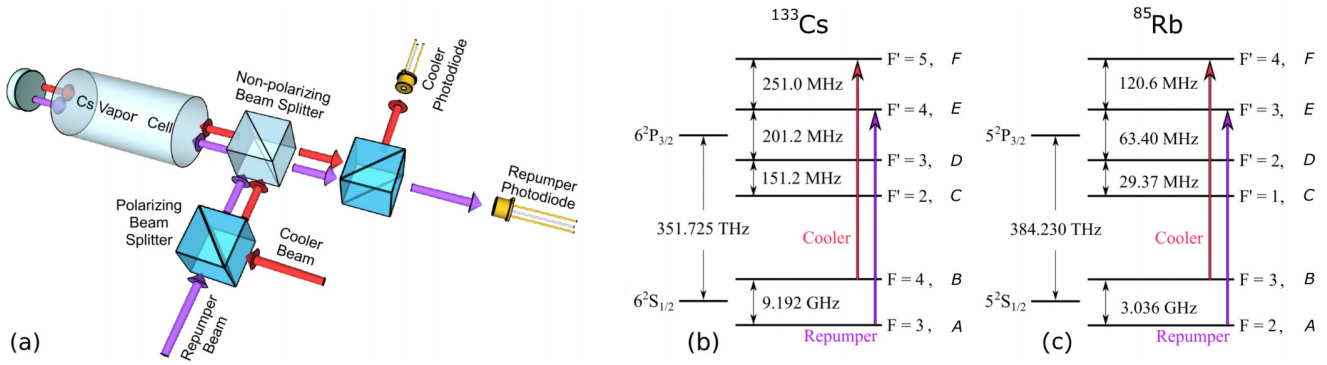

FIG. 1. (a) Experimental setup used for dual-beam spectroscopy. For clarity, the spatially overlapped laser beams are illustrated side by side. (b) Level structure for ^{133}Cs, indicating the role of the cooler and repumper lasers. (c) Level structure for ^{85}Rb.

These results are of particular relevance to the burgeoning field of portable quantum technologies [28–31]. Here, the achievable reductions in size, weight, and complexity offered by allowing multiple beams to share one spatial pathway are important. Furthermore, the drive for miniaturization increases the desirability of using small vapor cells with correspondingly reduced optical depths [32–35]. Operating these quantum technology systems outside the laboratory results in exposure to increased environmental noise, requiring improvements in signal strength and sensitivity. We analyze two examples for alkali atoms, ^{133}Cs and ^{85}Rb, which are frequently used and highly relevant in quantum technologies. The locking scheme was successfully applied in [30] to create a magneto-optical trap with 10^8 Rb atoms, without further description.

This paper is structured as follows: we describe the experimental implementation of this technique and present a rate-equation model that explains its key features. Experimental results spanning the full two-dimensional (2D) frequency space associated with dual-frequency spectroscopy are shown, and simultaneous frequency stabilization of lasers addressing two different transitions within the same atomic species is performed. As a result, the frequency stability of these lasers is found to be up to 3 times better than that achieved using conventional spectroscopic stabilization.

II. SETUP AND LAYOUT

Consider two orthogonally polarized laser beams from independent lasers, which are combined and spatially overlapped at a polarizing beam splitter. The two beams copropagate through a Doppler-free spectroscopy setup [18], sharing the same optical components, as illustrated in Fig. 1(a). After interacting with the cell the laser beams are separated at a polarizing beam splitter, and their intensities are individually recorded on separate photodiodes, yielding outputs V_1 and V_2. This configuration is chosen as required for most atomic physics experiments, which rely on two frequencies (cooler and repumper) for atom cooling, as shown for the examples of ^{133}Cs and ^{85}Rb in Fig. 1(b).

The frequencies of both beams are tuned close to resonance with the D_2 line of the relevant atomic species, in our case ^{133}Cs and ^{85}Rb: the repumper laser is resonant with transitions from the lower hyperfine state of the "ground" (S-state) manifold, and the cooler laser is resonant with transitions from the upper hyperfine state [see Fig. 1(b)]. Throughout this paper, laser frequencies will always be specified relative to the highest-frequency atomic transition in their respective manifolds, e.g., relative to the $F = 4 \rightarrow F' = 5$ transition for the cooler laser for ^{133}Cs.

The use of only a single optical frequency for spectroscopy on the D lines of alkali-metal atoms results in pumping of the atomic population into a state not addressed by the pumping light, just as observed in magneto-optical trapping experiments [15,36], leading to attenuation of the atomic response and a weaker spectroscopic signal. When light resonant with both cooler and repumper transitions is present [see Fig. 1(b)], there are no long-lived, noninteracting states in which atoms can accumulate; simultaneous use of both lasers therefore prevents attenuation of the spectroscopic signal via optical pumping. Figure 2 shows the results of this experiment with one laser frequency fixed and the other scanned, corresponding to a one-dimensional (1D) slice through the available parameter space, for ^{133}Cs. Figure 2(a) details the output of the repumper photodiode, with one laser scanned across the $F = 3 \rightarrow F' = 3, 4, 5$ transition (blue line), while light tuned to -365 MHz from the $F = 4 \rightarrow F' = 5$ transition is also present. The full experimental parameters used are given in Appendix B.

Figure 3 shows a comparable measurement for ^{85}Rb. Figure 3(a) presents the spectrum measured by the cooler photodiode, where one laser is scanned across the $F = 2 \rightarrow F' = 2, 3, 4$ transition, while light tuned to the $F = 3 \rightarrow F' = 3$ transition is also present (blue line). Figures 2(a) and 3(a) clearly show that the use of dual-frequency spectroscopy (blue line) substantially increases the overall absorption of the light by the atomic vapor and the size and spread of the sub-Doppler features in comparison to standard Doppler-free spectroscopy (gray line). The dashed lines represent a fit to the Doppler valley, i.e., the expected absorption in the absence of sub-Doppler features revealed by pump-probe spectroscopy; the spectroscopic signals are then locally normalized against this fit (a standard approach to removing the Doppler-broadened absorption and leaving only the desired sub-Doppler features) and differentiated with respect to the frequency of the scanned laser to yield the "error signal" S,

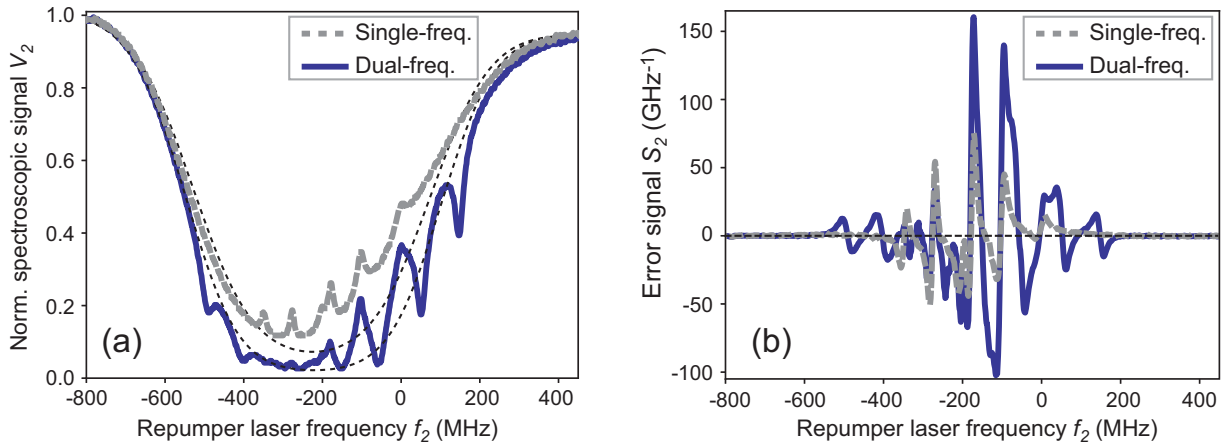

FIG. 2. (a): ^{133}Cs spectroscopy signal V_2 from the repumper photodiode [see Fig. 1(a)] while light from the cooler laser, tuned 365 MHz below the $F = 4 \rightarrow F' = 5$ transition, is also present in the cell (solid blue line). A standard Doppler-free saturated absorption spectroscopy signal (gray dashed line) is shown for reference, while the dotted lines are fits to the Doppler-broadened absorption profile in each case. The addition of light tuned to the cooler transition substantially increases the size and spread of the Doppler-free features. (b) Doppler-free error signal (see text) resulting from the spectroscopic signals in (a). In both panels, the laser-frequency axis is that of the repumper laser relative to the $F = 3 \rightarrow F' = 4$ transition.

plotted in Figs. 2(b) and 3(b); this is the signal typically used for feedback stabilization of a laser's frequency based on Doppler-free spectroscopy, and it is given by $S(f_i) = V_{\mathrm{DB},i}^{-1}(dV_i/df_i)$, where $V_{\mathrm{DB},i}$ is the photodiode signal corresponding to the fitted, Doppler-broadened light transmission for a given laser frequency, V_i denotes the measured photodiode output, and f_i is the frequency of the relevant laser.

The comparisons in Figs. 2(b) and 3(b) show how dual-frequency spectroscopy yields greater error signal sensitivity dS/df and broader capture ranges (the range of laser frequencies over which the sign of dS/df is unchanged) about the zero crossings of the error signal, known as the "lock points" because laser frequency can be stabilized most effectively at these values. In addition, a greater number of potential lock points become available over a wider frequency range than for conventional pump-probe spectroscopy.

III. MODEL AND THEORY

An intuitive analysis of this system can explain the enhanced absorption, the increased number of absorption peaks, and the latticelike structure observed in 2D frequency space, which is seen Figs. 4(a) and 5(a). When the cooler and repumper lasers are simultaneously resonant with atoms with similar velocities, the absorption of light from both beams is enhanced. For copropagating beams the simultaneous resonance condition requires that the two laser frequencies are separated by a fixed amount, thus creating a set of sharp

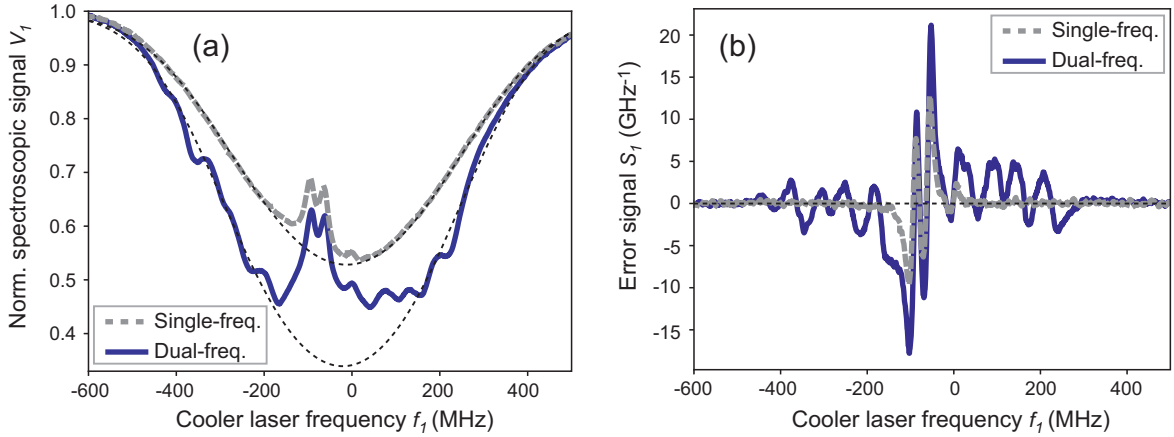

FIG. 3. (a) ^{85}Rb spectroscopy signal V_1 from the cooler photodiode [see Fig. 1(a)] while light from the repumper laser, resonant with the $F = 3 \rightarrow F' = 3$ transition, is also present in the cell (solid blue line). A standard Doppler-free saturated absorption spectroscopy signal (dashed gray line) is shown for reference, while the dotted lines are fits to the Doppler-broadened absorption profile in each case. The addition of light tuned to the repumper transition increases the size and spread of the Doppler-free features. (b) Doppler-free error signal (see text) resulting from the spectroscopic signals in (a). In both panels, the laser-frequency axis is that of the cooler laser relative to the $F = 4 \rightarrow F' = 5$ transition.

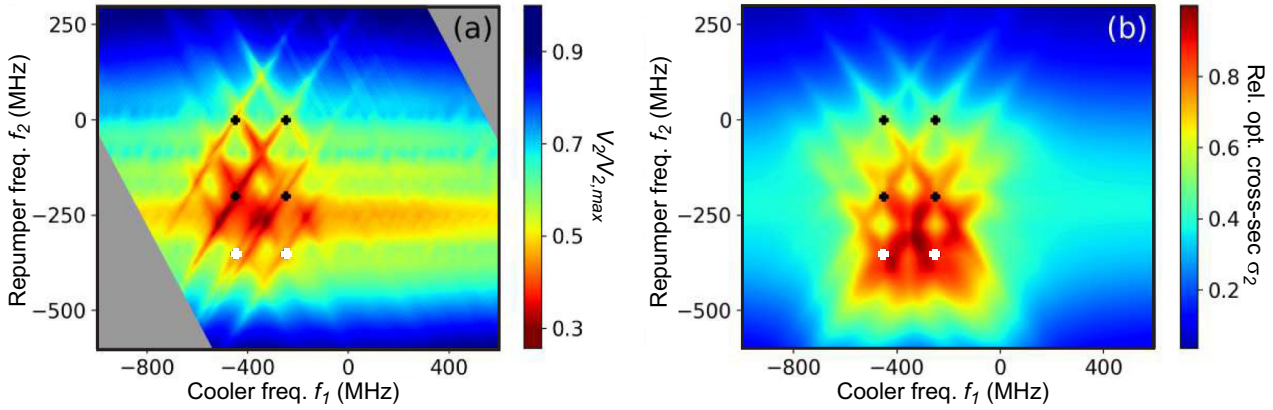

FIG. 4. (a) Spectroscopic signal V_2 from the ^{133}Cs repumper laser photodiode as a function of the frequencies of both lasers. Frequencies for the cooler and repumper lasers are given relative to the $F = 4 \rightarrow F' = 5$ and $F = 3 \rightarrow F' = 4$ transitions, respectively. (b) Prediction of the rate-equation model for the relative optical absorption cross section per atom from the repumper beam σ_2. To guide the eye, pluses indicate the points where the two lasers are simultaneously resonant with relevant transitions in stationary atoms such that optical pumping effects lead to diagonal line features; the black pluses represent transitions that produce line features in the absorption of both lasers, while the white pluses represent cycling transitions that do not heavily affect the absorption of the other laser. The rate-equation model describes the observed key features very well. The simulation assumes that the intensity of the return beam is always half of that of the incoming beam.

features, similar to those seen in saturated absorption spectroscopy, that map out diagonal lines of positive slope in 2D frequency space. For counterpropagating beams, the same effect is present, but the sign of the slope is reversed. Since both copropagating and counterpropagating beams are present in the vapor cell, the dual-frequency optical pumping effects can be expected to produce diagonal line features with both positive and negative slopes. We show below that the full lattice structure is required for efficient, simultaneous laser stabilization.

We develop a theoretical model that correctly predicts the key features of our results and elucidates the underlying physical mechanisms. For this the transient behavior of atoms traversing the beam is approximated as follows: we assume that some fraction of the atoms N_F recently entered the laser beam and remains in an equal mixture of the two hyperfine states of the $6S_{1/2}$ level. The remaining atomic population is taken to be in a state of dynamic equilibrium. This is a reasonable approximation, as very few cycles of optical pumping are required to redistribute the atomic population.

To determine the influence of these "equilibrium-state" atoms on the spectroscopic signals, we adopt a similar approach to [37], developing a rate-equation-based model in which we consider the six-level systems shown in Fig. 1. For convenience, we label the atomic states A–F, in ascending order from the bottom of the figure. For now, consider only a single atom with fixed laser detunings—the thermal distribution of atomic velocities and corresponding Doppler shifts will be factored in later. We define a set of rate coefficients, τ_{ij} and Γ_{ij}, such that the stimulated and spontaneous transition rates between, for example, states E and B are given by $\tau_{EB}I_{EB}$ and Γ_{EB}, respectively, where I_{EB} is the intensity of the laser light tuned to the relevant set of transitions (i.e., cooler or repumper). The spontaneous decay rates for the

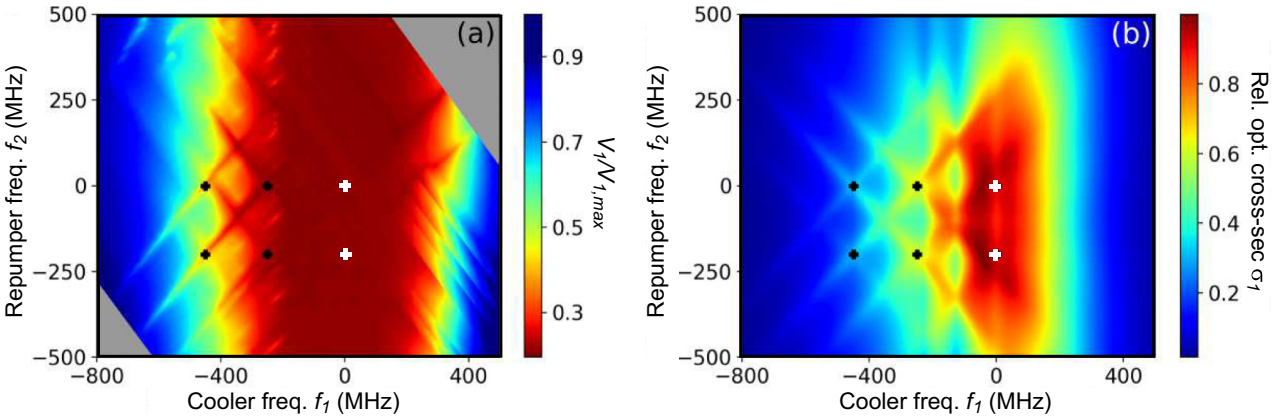

FIG. 5. (a) Spectroscopic signal V_1 from the ^{133}Cs cooler laser photodiode as a function of the frequencies of both lasers. (b) Corresponding theoretical prediction for the optical absorption cross section per atom σ_1. Both panels are analogous to their counterparts in Fig. 4 and were produced under the same conditions.

relevant transitions are already known accurately; see, for example, [38]. To determine the rate coefficients for stimulated transitions, we equate the steady-state results for the upper state population produced by our rate-equation model to those produced by solving the full optical Bloch equations for a two-level system. For a transition with spontaneous decay rate Γ, illumination of detuning δ, and intensity I, with Rabi frequency Ω, we obtain

$$\frac{\Omega^2/4}{\delta^2+\Omega^2/2+\Gamma^2/4}=\frac{\tau I}{2\tau I+\Gamma}. \tag{1}$$

Therefore, labeling the dipole matrix element $\langle E|x|B\rangle$ between two levels as X_{EB}, we find that

$$\tau_{EB}=\frac{\Omega_{EB}^2\Gamma_{EB}}{4I_{EB}\left(\delta_{EB}^2+\Gamma_{EB}^2/2\right)}=\frac{e^2|X_{EB}|^2\Gamma_{EB}}{2\hbar^2c\epsilon_0\left(\delta_{EB}^2+\Gamma_{EB}^2/2\right)}, \tag{2}$$

with similar results for the other transitions. Hence, using each state's label to denote the population fraction in that state, the rate equations governing the system are given by

$$\frac{dF}{dt}=(B-F)\tau_{FB}I_{FB}-F\Gamma_{FB}, \tag{3}$$

with corresponding expressions for the time derivatives of the populations of the remaining states (see Appendix A). Setting all time derivatives to zero and the total population across all states equal to 1, we solve the equations to find the fractional steady-state populations in each state. The full derivation is given in Appendix A. Here, we simply quote the result, first defining the following notation:

$$\gamma_{ij}=\tau_{ij}I_{ij}+\Gamma_{ij}, \tag{4}$$

$$k_{ij}=\frac{\tau_{ij}I_{ij}}{\sum_k\gamma_{ik}}, \tag{5}$$

$$\zeta_i=\frac{1}{\sum_j\tau_{ji}I_{ji}}, \tag{6}$$

and the composite coefficient

$$\Phi=\frac{(k_{EA}\gamma_{EB}+k_{DA}\gamma_{DB})\zeta_B}{1-(k_{FB}\gamma_{FB}+k_{EB}\gamma_{EB}+k_{DB}\gamma_{DB})\zeta_B}, \tag{7}$$

with summations carried out only where explicitly indicated, over all dipole-allowed transitions. We find that in the steady state

$$A=\left[1+\sum_i k_{iA}+\Phi\left(1+\sum_j k_{jB}\right)\right]^{-1}, \tag{8}$$

with the remaining fractional populations given by

$$B=\Phi A, \tag{9}$$

and for the upper manifold

$$i=k_{iA}A+k_{iB}B, \tag{10}$$

where $i\in\{C,D,E,F\}$, as given in Fig. 1.

Having obtained the steady-state populations, we can now determine the rate of photon loss per equilibrium-state atom $L_{\rm eq}$ from a given beam as

$$L_{\rm eq}=\sum(j-i)\tau_{ij}I_{ij}, \tag{11}$$

where the sum is taken over all combinations of upper manifold states i and lower manifold states j between which dipole-allowed transitions can be stimulated by the chosen beam ignoring the negligible stimulation of cooler (repumper) transitions by repumper (cooler) lasers. The unpumped atoms can be taken into consideration at this stage as well, yielding

$$L=(1-N_F)\sum(j-i)\tau_{ij}I_{ij}+N_F\sum\frac{1}{2}\tau_{ij}I_{ij}. \tag{12}$$

Equation (12) can be used to determine the rate of attenuation of a laser beam by stationary atoms subject to known illumination conditions. To accurately model a thermal atomic vapor, the velocity distribution of the atoms and corresponding Doppler shift in each beam's effective detuning must be taken into account. This can be done by integrating Eq. (12) over the atomic velocity distribution, where the dependence of L on atomic velocity comes in via the dependence of the values of δ_{ij} in Eq. (2) on atomic velocity (due to the Doppler shift) and the corresponding variation in the values of τ_{ij}. We define $L_{\rm thermal}$ as the average loss rate of photons from the beam per atom, given the atoms' thermal velocity distribution. In the case of a thermal atomic vapor at temperature T, considering only the first-order Doppler shift, this is given by

$$L_{\rm thermal}=\frac{1}{N}\int_{-\infty}^{\infty}L(v)\exp\left(-mv^2/2k_{\rm B}T\right)dv, \tag{13}$$

where m is the mass of the atoms, $k_{\rm B}$ is the Boltzmann constant, and the integration variable v corresponds to the atomic velocity component along the axis of the laser beams. $N=\sqrt{2\pi k_{\rm B}T/m}$ is the normalization constant for the 1D Boltzmann distribution. Furthermore, one must consider that there are counterpropagating beams within the vapor cell. These can be taken into account by summing the contributions of the different beams to the stimulated transition rates, such that in the equations above $\tau_{ij}I_{ij}$ becomes $\tau_{ij}I_{ij}$(beam 1) + $\tau_{ij}I_{ij}$(beam 2). Note that for counterpropagating beams the signs of the Doppler shift on the value of δ_{ij} in Eq. (2) will be opposite for the two beams.

With this substitution made, Eq. (13) can be used to deduce the mean optical absorption cross section per atom [39]. for a given laser as a function of both laser frequencies; normalized against its maximum value, we label the absorption cross section per atom σ_1 and σ_2 for the repumper and cooler lasers, respectively.

The results are shown in Figs. 4 and 5 alongside our experimental data. The theoretical model explains the key observed features well. The presence of each beam increases the strength of the absorption of the other beam and creates sharp locking features, similar to those seen in saturated absorption spectroscopy, in a diagonal crisscross pattern across the Doppler valley. Exact, quantitative agreement requires a more complex model that is not developed here.

IV. EXPERIMENTAL RESULTS

Figures 4 and 5 show the output signals from the photodiodes depicted in Fig. 1(a) as a function of the frequencies of both the cooler and repumper lasers for the case of ^{133}Cs. These were obtained by synchronously scanning both laser frequencies across the relevant frequency range. This results

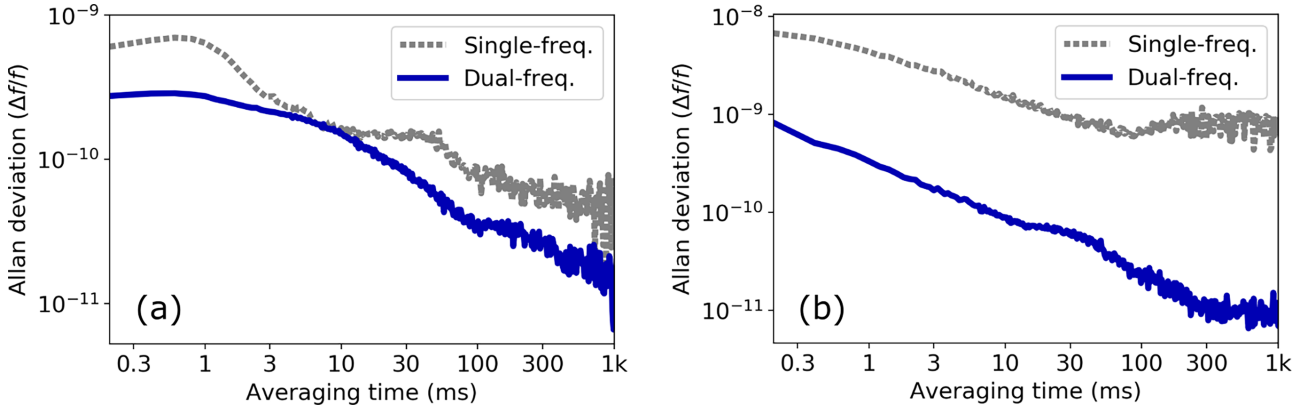

FIG. 6. Measured Allan deviation of the frequency of lasers stabilized to the (a) cooler and (b) repumper transitions of the D_2 line of ^{85}Rb, using both dual-frequency (solid blue line) and conventional Doppler-free (dotted gray line) spectroscopy to generate the feedback signal for laser stabilization. Note that the point of interest is not the absolute degree of stability achieved, but the improvement consistently provided by employing the dual-frequency spectroscopy scheme.

in the collection of data along diagonal lines in 2D frequency space. The gray area in Figs. 4 and 5 indicates parts between the plot axes where no data have been taken.

Figure 4(a) shows the output of the repumper photodiode V_2 for ^{133}Cs in comparison to the result of the rate-equation model in Fig. 4(b). An independent frequency reference was provided by simultaneously directing light from each of the lasers to a standard saturated absorption spectroscopy apparatus. The rate-equation model reproduces the experimentally observed features well for a 75-mm cell at 298 K. The diameter of each beam was 1.25 mm, with 0.14 mW of cooler light and 0.23 mW of repumper light present.

Figures 4 and 5 show that the rate-equation model successfully explains the key features of the technique and predicts qualitative trends; the numerical model reveals both the enhanced absorption and the existence and origins of the diagonal line features observed. A quantitative comparison is not attempted due to the simplifications involved in the model. The core benefits of dual-frequency spectroscopy are clearly visible in both spectra: the presence of the additional cooler (repumper) frequency light enhances the absorption signal of the repumper (cooler) light by the atomic vapor and generates sharp, sub-Doppler features in a diagonal grid pattern over a frequency range of about 700 MHz—considerably broader than the 450 MHz (for the cooler laser) or 350 MHz (for the repumper laser) over which conventional saturated absorption spectroscopy produces Doppler-free resonance features. This enables the technique to be used for frequency stabilization at a wider range of frequency offsets than is usually possible.

The enhancement of the absorption signal is also shown in Fig. 2(a). For reference, the blue dual-frequency data displayed in Fig. 2(a) would correspond to a vertical slice through Fig. 4(a) at a cooler frequency of −365 MHz, while the conventional, single-frequency spectrum [gray data in Fig. 2(a)] would be reproduced by a vertical slice in the limit of large detuning of the cooler laser. The strong observed enhancement of the absorption signal translates to more accurate laser frequency stabilization by providing a feedback signal with improved sensitivity and signal-to-noise ratio. This will be discussed and characterized in the next section.

V. APPLICATION TO LASER FREQUENCY STABILIZATION

As shown above, dual-frequency spectroscopy offers improved feedback signal strength and sensitivity compared to conventional spectroscopy. The dual-frequency error signals allow superior laser frequency stabilization for two lasers simultaneously, as seen in Fig. 6, which is discussed in more detail below.

The simplest way to achieve this is to select the correct locations in 2D frequency space (lock points) at which to stabilize the lasers' frequencies; in general, the dual-frequency stabilization signal for each laser can depend on the frequency of the other laser, but efficient frequency stabilization is possible at lock points where the local gradient of each laser's stabilization signal with respect to the other laser's frequency is zero or at a wider range of points through the use of a composite feedback signal (see Appendix C).

The simplest approach to this, and the one we adopt in our cold-atom experiment [30,31], is to stabilize the lasers at positions in 2D frequency space where, to first order in frequency changes about the chosen point, there is no dependence of the error signal for one laser on the frequency of the other laser, i.e.,

$$\frac{dS_1}{df_2} = \frac{d^2V_1}{df_1 df_2} = 0, \tag{14}$$

with the corresponding condition for dS_2/df_1. Figure 7 shows the "cross derivatives"—the derivatives of the absorption strength for one laser with respect to both laser frequencies—for ^{133}Cs as an example. These are derived as $d^2\sigma_1/(df_1 df_2)$ and $d^2\sigma_2/(df_2 df_1)$ from the results shown in Figs. 5(b) and 4(b).

From Fig. 7, one can identify the positions where these derivatives are both zero and, therefore, independent laser frequency stabilization (to first order) is possible. The corresponding figure for Rb is given in Appendix D. In particular, this condition is fulfilled wherever local maxima or minima in both V_1 and V_2 are coincident in frequency space. A local minimum in both signal voltages occurs at each of the intersections of the lines of positive and negative slope in 2D frequency

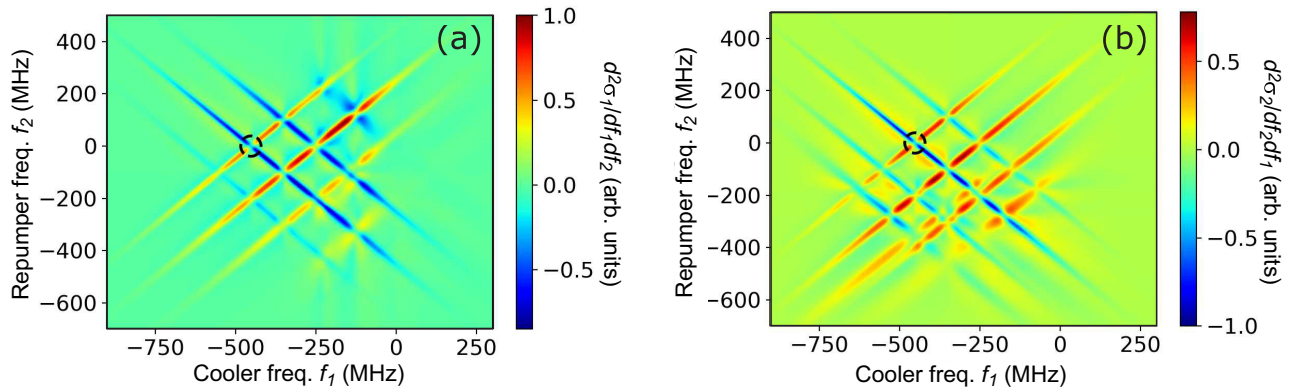

FIG. 7. Normalized cross derivatives (see text) of the theoretical optical absorption cross section per atom σ for ^{133}Cs (a) cooler and (b) repumper lasers, with respect to the frequencies of both lasers, $d^2\sigma_1/(df_1df_2)$ and $d^2\sigma_2/(df_2df_1)$, respectively. Zeros of these derivatives, such as those that occur at the intersections of the diagonal line features of opposite slope, are locations where the lasers can be simultaneously stabilized without interdependence of their lock points. The dashed black circles highlight one such point, showing that the zero of the cross derivative occurs at the same point in frequency space for both lasers.

space that occur in both laser signals; see, for example, the point highlighted in Fig. 7. This immediately creates a number of suitable locking points equal to the square of the number of relevant transition pairings (corresponding to the four black diamonds that are common to both Figs. 4 and 5). The locations of these locking points depend only on the frequency of the two lasers, not on the applied optical power (except for extremely high or low illumination intensities that would not be used in real experiments); the method is therefore not adversely affected by changes in incident optical power. As an example, for ^{133}Cs this yields 16 potential dual-frequency locking points, well in excess of the ∼5 plausible locking points generally usable with conventional spectroscopic stabilization. Furthermore, these lock points are spread over a frequency range 200 MHz broader than the standard transition manifold, allowing more flexibility for off-resonant laser stabilization.

The stability of two simultaneously locked lasers is characterized in Fig. 6 by determining the Allan deviation of the laser frequencies for averaging times between 0.2 ms and 1 s and compared to conventional Doppler-free spectroscopic stabilization with otherwise identical system parameters. The frequency stability was measured by logging the deviation of the stabilization signal from zero over a period of 10 s. Figure 6 compares dual-frequency stabilization to the $F = 3 \rightarrow F' = 3$ and $F = 2 \rightarrow F' = 3$ transitions of ^{85}Rb against individual stabilization to the $F = 3 \rightarrow F' = 4$ transition and the $F = 2 \rightarrow F' = 2 \otimes 3$ crossover transition [40].

The absolute values of the frequency stability achieved are within the expected range, being superior to those measured in systems with a broader response, such as wavemeter-based stabilization [41] but inferior to those obtained with custom-built, ultrastable laser systems [42,43]. Since our cooler and repumper lasers employ very different hardware—a butterfly packaged-distributed-feedback laser and an external cavity diode laser, respectively—they experience different technical sources of frequency instability, so the differing time profiles of their Allan deviations are not unexpected.

The improvement in stability achieved through the use of dual-frequency spectroscopy, within an otherwise identical system, is clearly visible in Fig. 6 and, for the cooler laser, corresponds approximately to the improvement expected from the increase in the gradient of the stabilization feedback signal over most of the range of averaging times studied. Over a small range of averaging times on the order of 10 ms the Allan deviation for the cooler laser becomes comparable using both single- and dual-frequency spectroscopy; the reason for this are not fully understood, but it may be related to nontrivial coupled feedback effects in the laser stabilization electronics and is likely a technical artifact specific to our experimental arrangement.

Similarly, the full stability improvement seen for the repumper laser—a factor >10 over most of the range of averaging times studied—cannot be explained by our model. The better than expected performance here could stem from technical considerations specific to our feedback hardware or from a sharpening of the atomic response by coherent effects omitted from our rate-equation model.

Going beyond the method described here, a broader range of locking points can be accessed through the generation of composite feedback signals that are a function of the outputs from both photodiodes; this technique is explained in detail in Appendix C.

For simultaneous laser stabilization using dual-frequency spectroscopy, both lasers must be brought to and maintained at frequencies close to the desired locking point while the feedback control is engaged. If passive laser stability is poor, this can be slightly more challenging than locking a single laser. This difficulty can be mitigated with customized control electronics and user interfaces.

VI. CONCLUSIONS

Our results show that the use of spatially overlapping beams tuned to different atomic transitions can allow optical pumping effects to be exploited to enhance signal strength in atomic vapor spectroscopy. Optical pumping effects lead to a large number of crossover features, allowing laser stabiliza-

tion at a greater range of frequencies than via conventional Doppler-free spectroscopy. The technique provides clear advantages wherever two frequencies are required and space, weight, and optical components are at a premium, as well as in situations where signal strength and frequency sensitivity are important. This applies to a number of quantum technology research areas, ranging from portable devices such as gravimeters, magnetometers, and atomic clocks to precision laboratory-based experiments where the accuracy of laser frequency stabilization is paramount.

We provided detailed data on spectroscopy on the D_2 lines of cesium and rubidium in unheated, 75-mm-long cells at 20 °C. The enhanced contrast of the absorption signal is particularly relevant for short vapor cells [34,35,44]. The same principles demonstrated here will apply within any atomic vapor that exhibits sharp, saturable optical transitions. In particular, the absence of a "cycling transition" in lower-mass alkali-metal atoms (Li, Na, and K), brought about by the small energy separation of the hyperfine states of the upper manifold of the D_2 lines, suggests that the benefits of avoiding optical pumping to dark states may be enhanced for these species.

Future extensions of this technique include demodulation of the signal from one photodiode at the current modulation frequencies of both lasers, thus yielding two different derivative signals from each photodiode (e.g., dV_1/df_1 and dV_1/df_2 from the cooler photodiode) and enabling frequency stabilization at almost any point in 2D frequency space. Dual-frequency forms of modulation transfer spectroscopy [45] should also be possible, allowing this important technique to be exploited through current modulation of either one of the two lasers, avoiding the need for costly electro-optic modulation equipment. Finally, including further laser frequencies may open up yet more technical possibilities and reveal additional physical phenomena.

All data necessary to support the conclusions of this paper are given in the paper. All further data related to this work are available from the authors upon request.

ACKNOWLEDGMENTS

The authors thank B. Foxon and I. Lesanovsky for useful discussions and R. Chacko for assistance with data collection. This work was supported by IUK Projects No. 133086 and No. 10031462, EPSRC Grants No. EP/R024111/1 and No. EP/M013294/1, JTF Grant No. 62420, and the European Commission grant ErBeStA (Grant No. 800942).

The authors declare the following competing interests: N.C. and L.H. are inventors on UK pending patent application GB 1916446.6 (applicant: University of Nottingham, inventors: Nathan Cooper, Lucia Hackermüller, Laurence Coles) for a miniaturized spectroscopy device in which dual-frequency beam overlap is exploited as an aid to compactness.

APPENDIX A: RATE EQUATION MODEL

We provide the expressions for the time derivatives of the remaining atomic state populations:

$$\frac{dE}{dt} = (A-E)\tau_{EA}I_{EA} + (B-E)\tau_{EB}I_{EB} - E\Gamma_{EB} - E\Gamma_{EA}, \tag{A1}$$

$$\frac{dD}{dt} = (B-D)\tau_{DB}I_{DB} + (A-D)\tau_{DA}I_{DA} - D\Gamma_{DB} - D\Gamma_{DA}, \tag{A2}$$

$$\frac{dC}{dt} = (A-C)\tau_{CA}I_{CA} - C\Gamma_{CA}, \tag{A3}$$

$$\frac{dB}{dt} = (F-B)\tau_{FB}I_{FB} + (E-B)\tau_{EB}I_{EB} + (D-B)\tau_{DB}I_{DB} + F\Gamma_{FB} + E\Gamma_{EB} + D\Gamma_{DB}, \tag{A4}$$

and

$$\frac{dA}{dt} = (E-A)\tau_{EA}I_{EA} + (D-A)\tau_{DA}I_{DA} + (C-A)\tau_{CA}I_{CA} + E\Gamma_{EA} + D\Gamma_{DA} + C\Gamma_{CA}. \tag{A5}$$

Then, employing the terms defined in Eq. (1), (2), and (4)–(7) and setting all time derivatives to zero, as is the case in the steady state, Eq. (3) and its counterparts above can be rearranged to give

$$F = \frac{B\tau_{FB}I_{FB}}{\gamma_{FB}} = Bk_{FB}, \tag{A6}$$

$$E = \frac{A\tau_{EA}I_{EA} + B\tau_{EB}I_{EB}}{\gamma_{EA}+\gamma_{EB}} = Ak_{EA} + Bk_{EB}, \tag{A7}$$

$$D = \frac{A\tau_{DA}I_{DA} + B\tau_{DB}I_{DB}}{\gamma_{DA}+\gamma_{DB}} = Ak_{DA} + Bk_{DB}, \tag{A8}$$

$$C = \frac{A\tau_{CA}I_{CA}}{\gamma_{CA}} = Bk_{CA}, \tag{A9}$$

$$B = \frac{D\gamma_{DB} + E\gamma_{EB} + F\gamma_{FB}}{\tau_{DB}I_{DB} + \tau_{EB}I_{EB} + \tau_{FB}I_{FB}} = \frac{D\gamma_{DB} + E\gamma_{EB} + F\gamma_{FB}}{\zeta_B}, \tag{A10}$$

and

$$A = \frac{C\gamma_{CA} + D\gamma_{DA} + E\gamma_{EA}}{\tau_{CA}I_{CA} + \tau_{DA}I_{DA} + \tau_{EA}I_{EA}} = \frac{C\gamma_{CA} + D\gamma_{DA} + E\gamma_{EA}}{\zeta_A}. \tag{A11}$$

Substitution of Eqs. (A6) to (A8) into (A10) then yields

$$B = \zeta_B^{-1}[\gamma_{DB}(Ak_{DA} + Bk_{DB}) + \gamma_{EB}(Ak_{EA} + Bk_{EB}) + \gamma_{FB}Bk_{FB}]. \tag{A12}$$

Collecting terms in A and B and dividing through by the coefficient of B, one finds that

$$B = \Phi A. \tag{A13}$$

Now all other state populations can be expressed in terms of A. As a final constraint, we impose the condition that the sum over all state-population fractions must be equal to 1. Expressing all state populations in terms of A and setting their sum equal to 1 yields Eq. (8). Combining this with Eq. (A6) to (A9) and (A13) above directly gives all of the steady-state population fractions.

APPENDIX B: DETAILS OF EXPERIMENTAL DATA COLLECTION

During the data collection for Fig. 2 in the main text, 0.37 mW of cooler light, at a fixed frequency of −365 MHz (relative to the $F = 4 \rightarrow F' = 5$ transition), was directed into the apparatus alongside 0.25 mW of repumper light. For Fig. 3, the same beam diameters were used with 0.17 mW of cooler light and 0.42 mW of repumper light. The repumper light was resonant with the $F = 3 \rightarrow F' = 3$ transition of the D_2 line of ^{85}Rb.

In Figs. 4(a) and 5(a) optical transmission data were collected across a broad region of 2D frequency space by synchronously scanning the frequencies of both lasers. Synchronous laser frequency ramps were performed by adding a linear ramp to the current supplied to each laser diode and simultaneously ramping the voltage supplied to piezoelectric transducers that control the alignment of diffraction gratings used for external cavity feedback. The result is laser frequencies, f_1 and f_2, described by

$$f_1 = a + bt, \quad f_2 = c + dt, \tag{B1}$$

where t is the time since the start of the ramp, f_1 and f_2 are the frequencies of the cooler and repumper lasers, respectively, and a–d are constant coefficients. The resulting equation expressing f_2 as a function of f_1 is

$$f_2 = \frac{d}{b} f_1 + \left(c - \frac{da}{b}\right). \tag{B2}$$

This equation describes a diagonal line in the parameter plane displayed in Fig. 4, with gradient d/b and offset $c - (da/b)$. By adjusting either of the static frequency offsets, a and c, data along multiple such lines were collected and used to build up a full 2D data set as displayed. Note that the boundaries of the region within which data were collected consequently form diagonal lines in 2D frequency space, hence the grayed-out triangles in the corners of Figs. 4(a) and 5(a). The spectroscopic signals from conventional, single-frequency spectroscopy apparatus were collected at the same time for each laser, enabling independent determination of laser frequency.

APPENDIX C: STABILIZATION WITH NONZERO CROSS DERIVATIVES

In the main text laser frequency stabilization at selected locations in 2D frequency space was considered, where the derivative of each laser's stabilization signal with respect to the frequency of the other laser was zero. However, a more general method exists that enables frequency stabilization at a much wider range of locations within 2D frequency space. Consider two lasers with frequencies f_1 and f_2 generating corresponding photodiode outputs V_1 and V_2. We assume that the currents of the two lasers are modulated at different frequencies to avoid direct cross talk.

Evaluating all derivatives at the chosen locking point, the gradient of the spectroscopic signal after demodulation S_1 is given by

$$\frac{dS_1}{df_1} = \vartheta_1 \frac{d^2V_1}{df_1^2} \tag{C1}$$

and

$$\frac{dS_1}{df_2} = \vartheta_1 \frac{d^2V_1}{df_1\, df_2}, \tag{C2}$$

where ϑ_1 and ϑ_2 are constants that depend on the parameters of the laser current modulation, with corresponding expressions for the gradient of S_2. One can therefore define a composite parameter χ_1 with no first-order dependence on f_2:

$$\chi_1 = S_1 - \kappa_1 S_2, \tag{C3}$$

where

$$\kappa_1 = \frac{\vartheta_1}{\vartheta_2} \frac{d^2V_1}{df_1\, df_2} \left(\frac{d^2V_2}{df_2^2}\right)^{-1}, \tag{C4}$$

with the value of κ_1 being determined by the requirement that the contributions of the first and second terms in (C3) to the gradient of χ_1 with respect to f_2 cancel. Corresponding expressions exist for χ_2. Thus, it is possible to generate a feedback signal for each laser that is, to first order, independent of the frequency of the other laser.

To determine the expected laser frequency stability when using this approach, one can define the "signal-limited stability factor" (M_{SL}), which is equal to the ratio of the sensitivity of the spectroscopic signal (to changes in laser frequency, about the desired lock point) in dual-frequency spectroscopy to the same parameter in a conventional spectroscopic setup; in this case the SLSF for laser 1 is therefore given by

$$M_{\mathrm{SL},1} = \frac{d\chi_1}{df_1} \Bigg/ \left(\frac{dS_{\mathrm{con}}}{df_{\mathrm{con}}} \sqrt{1 + \kappa_1^2}\right), \tag{C5}$$

where $dS_{\mathrm{con}}/df_{\mathrm{con}}$ is the gradient of the feedback signal about the lock point in an equivalent conventional saturated absorption spectroscopy apparatus. The factor of $\sqrt{1 + \kappa_1^2}$ normalizes against the amplification of the feedback signal that has been performed via postprocessing. One therefore finds that

$$M_{\mathrm{SL},1} = \left(\frac{dS_1}{df_1} - \kappa_1 \frac{dS_2}{df_1}\right) \Bigg/ \left(\frac{dS_{\mathrm{con}}}{df_{\mathrm{con}}} \sqrt{1 + \kappa_1^2}\right), \tag{C6}$$

with an equivalent expression for $M_{\mathrm{SL},2}$. This factor represents the quality of the frequency stabilization that can be achieved at any given locking point; lasers can be stabilized with superior performance to conventional spectroscopy at any location where both SLSF values exceed 1.

APPENDIX D: CROSS DERIVATIVES AND LOCKING POINTS FOR ^{85}Rb

By applying our theoretical model to ^{85}Rb, we obtain the structure of the cross derivatives of the optical

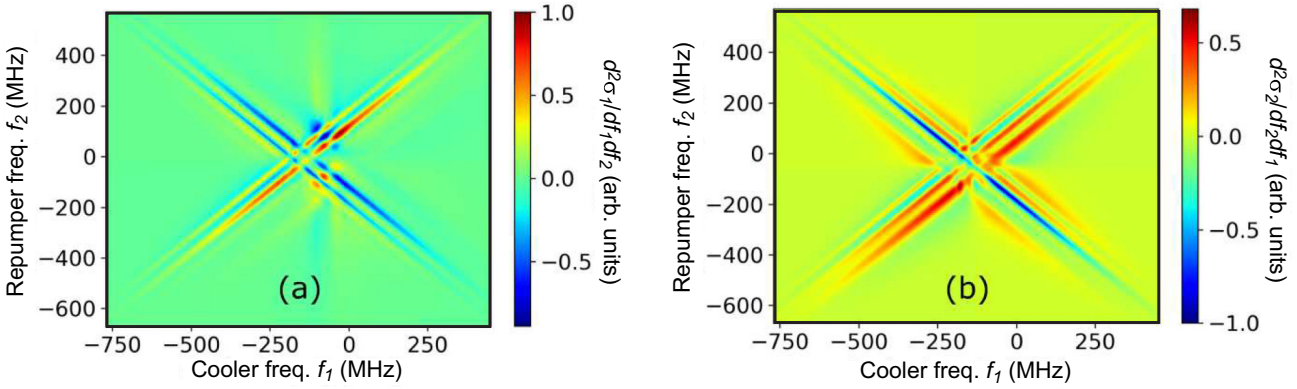

FIG. 8. Normalized cross derivatives of the theoretical optical absorption cross section per atom σ for ^{85}Rb (a) cooler and (b) repumper lasers, analogous to those shown in Fig. 7 for ^{133}Cs, with respect to the frequencies of both lasers. Zeros of this derivative, such as those that occur at the intersections of the diagonal line features of opposite slope, are locations where the lasers can be simultaneously stabilized without interdependence of their lock points.

absorption cross section for this species. Figure 8 shows the cross derivatives $d^2\sigma_1/(df_1df_2)$ and $d^2\sigma_2/(df_2df_1)$ vs f_1 and f_2 and highlights suitable locking points for the case of ^{85}Rb.

[1] I. Georgescu, 25 years of BEC, Nat. Rev. Phys. **2**, 396 (2020).

[2] J. Kitching, S. Knappe, and E. Donley, Atomic sensors—A review, IEEE Sens. J. **11**, 9 (2011).

[3] K. Van Tilburg, N. Leefer, L. Bougas, and D. Budker, Search for Ultralight Scalar Dark Matter with Atomic Spectroscopy, Phys. Rev. Lett. **115**, 011802 (2015).

[4] F. Sorrentino, K. Bongs, P. Bouyer, L. Cacciapuoti, M. De Angelis, H. Dittus, W. Ertmer, A. Giorgini, J. Hartwig, M. Hauth *et al.*, A compact atom interferometer for future space missions, Microgravity Sci. Technol. **22**, 551 (2010).

[5] S. Herrmann, H. Dittus, and C. Lammerzahl, Testing the equivalence principle with atomic interferometry, Classical Quantum Gravity **29**, 184003 (2012).

[6] P. Graham, J. Hogan, M. Kasevich, S. Rajendran, and R. Romani, Mid-band gravitational wave detection with precision atomic sensors, arXiv:1711.02225.

[7] I. Alonso, C. Alpigiani, B. Altschul, H. Araujo, G. Arduini, J. Arlt, L. Badurina, A. Balaz, S. Bandarupally, B. Barish, M. Barone, M. Barsanti, and S. Bass, Cold atoms in space: Community workshop summary and proposed road-map, EPJ Quantum Technol. **9**, 30 (2022).

[8] L. Badurina, E. Bentine, D. Blas, K. Bongs, D. Bortoletto, T. Bowcock, K. Bridges, W. Bowden, O. Buchmueller, C. Burrage *et al.*, AION: An atom interferometer observatory and network, J. Cosmol. Astropart. Phys. 05 (2020) 011.

[9] S. Bize, P. Laurent, M. Abgrall, H. Marion, I. Maksimovic, L. Cacciapuoti, J. Grünert, C. Vian, F. Pereira dos Santos, P. Rosenbusch, P. Lemonde, G. Santarelli, P. Wolf, A. Clairon, A. Luiten, M. Tobar, and C. Salomon, Cold atom clocks and applications, J. Phys. B **38**, S449 (2005).

[10] Y. Bidel, O. Carraz, R. Charriere, M. Cadoret, N. Zahzam, and A. Bresson, Compact cold atom gravimeter for field applications, Appl. Phys. Lett. **102**, 144107 (2013).

[11] V. Menoret, P. Vermeulen, N. Le Moigne, S. Bonvalot, P. Bouyer, A. Landragin, and B. Desruelle, Gravity measurements below 10^{-9} g with a transportable absolute quantum gravimeter, Sci. Rep. **8**, 12300 (2018).

[12] A. Fregosi, C. Gabbanini, S. Gozzini, L. Lenci, C. Marinelli, and A. Fioretti, Magnetic induction imaging with a cold-atom radio frequency magnetometer, Appl. Phys. Lett. **117**, 144102 (2020).

[13] E. Boto, N. Holmes, J. Legget, G. Roberts, V. Shah, S. S. Meyer, L. Duque Muñoz, K. J. Mullinger, T. M. Tierney, S. Bestmann, G. R. Barnes, R. Bowtell, and M. J. Brookes, Moving magnetoencephalography towards real-world applications with a wearable system, Nature (London) **555**, 657 (2018).

[14] C. Deans, L. Marmugi, and F. Renzoni, Sub-Sm^{-1} electromagnetic induction imaging with an unshielded atomic magnetometer, Appl. Phys. Lett. **116**, 133501 (2020).

[15] E. L. Raab, M. Prentiss, A. Cable, S. Chu, and D. E. Pritchard, Trapping of Neutral Sodium Atoms with Radiation Pressure, Phys. Rev. Lett. **59**, 2631 (1987).

[16] Y. Wu, B. Sun, and X. Li, Semiconductor laser active frequency stabilization technologies: A review, J. Korean Phys. Soc. **79**, 795 (2021).

[17] D. W. Preston, Doppler-free saturated absorption: Laser spectroscopy, Am. J. Phys. **64**, 1432 (1996).

[18] W. Demtröder, *Laser Spectroscopy* (Springer, Berlin, 2008).

[19] F. Riehle, *Frequency Standards: Basics and Applications* (Wiley-VCH, Weinheim, 2006).

[20] P. Mandal, V. Naik, V. Dev, A. Chakrabarti, and A. Ray, Blue fluorescence as a frequency offset reference in the rubidium 5S-5P-5D transition, Appl. Opt. **57**, 3612 (2018).

[21] D. Fahey and M. Noel, Excitation of Rydberg states in rubidium with near infrared diode lasers, Opt. Express **19**, 17002 (2011).

[22] V. Schultze, T. Scholtes, R. Ijsselsteijn, and H. Meyer, Improving the sensitivity of optically pumped magnetometers by hyperfine repumping, J. Opt. Soc. Am. B **32**, 730 (2015).

[23] R. Li, C. Perrella, and A. Luiten, Repumping atomic media for an enhanced sensitivity atomic magnetometer, Opt. Express **30**, 31752 (2022).

[24] M. Zhao, X. Jiang, R. Fang, Y. Qiu, Z. Ma, C. Han, B. Lu, and C. Lee, Laser frequency stabilization via bichromatic Doppler-free spectroscopy of an ^{87}Rb D_1 line, Appl. Opt. **60**, 5203 (2021).

[25] M. Hafiz, G. Coget, E. Clercq, and R. Boudot, Doppler-free spectroscopy on the Cs D1 line with a dual-frequency laser, Opt. Lett. **41**, 2982 (2016).

[26] M. Abdel Hafiz, D. Brazhnikov, G. Coget, A. Taichenachev, V. Yudin, E. Clercq, and R. Boudot, High-contrast sub-Doppler absorption spikes in a hot atomic vapor cell exposed to a dual-frequency laser field, New J. Phys. **19**, 073028 (2017).

[27] D. Brazhnikov, S. Ignatovic, I. Mesenzova, A. Mikhailov, R. Boudot, and M. Skortsov, Two-frequency sub-Doppler spectroscopy of the caesium D1 line in various configurations of counterpropagating laser beams, Quantum Electron. **50**, 1015 (2020).

[28] P. Knight and I. Walmsley, UK national quantum technology programme, Quantum Sci. Technol. **4**, 040502 (2019).

[29] K. Bongs, V. Boyer, M. Cruise, A. Freise, M. Holynski, J. Hughes, A. Kaushik, Y.-H. Lien, A. Niggebaum, M. Perea-Ortiz *et al.*, The UK national quantum technologies hub in sensors and metrology (keynote paper), Proc. SPIE **9900**, 990009 (2016).

[30] S. H. Madkhaly, L. A. Coles, C. Morley, C. D. Colquhoun, T. M. Fromhold, N. Cooper, and L. Hackermüller, Performance-optimized components for quantum technologies via additive manufacturing, PRX Quantum **2**, 030326 (2021).

[31] S. Madkhaly, N. Cooper, L. Coles, and L. Hackermüller, High-performance, additively-manufactured atomic spectroscopy apparatus for portable quantum technologies, Opt. Express **30**, 25753 (2022).

[32] S. Losev, D. Sevostianov, V. Vassiliev, and V. Velishansky, Production of miniature glass cells with rubidium for chip scale atomic clock, Phys. Procedia **71**, 242 (2015).

[33] Y. Ji, J. Shang, G. Li, J. Zhang, and J. Zhang, Microfabricated shaped rubidium vapor cell for miniaturized atomic magnetometers, IEEE Sens. Lett. **4**, 2500104 (2020).

[34] E. Talker, P. Arora, R. Zektzer, Y. Sebbag, M. Dikopltsev, and U. Levy, Light-Induced Atomic Desorption in Microfabricated Vapor Cells for Demonstrating Quantum Optical Applications, Phys. Rev. Appl. **15**, L051001 (2021).

[35] V. G. Lucivero, A. Zanoni, G. Corrielli, R. Osellame, and M. W. Mitchell, Laser-written vapor cells for chip-scale atomic sensing and spectroscopy, Opt. Express **30**, 27149 (2022).

[36] O. Schmidt, K.-M. Knaak, R. Wynands, and D. Meschede, Cesium saturation spectroscopy revisited: How to reverse peaks and observe narrow resonances, Appl. Phys. B **59**, 167 (1994).

[37] N. Cooper and T. Freegarde, Trapping of ^{85}Rb atoms by optical pumping between metastable hyperfine states, J. Phys. B **46**, 215003 (2013).

[38] D. A. Steck, Alkali D line data, http://steck.us/alkalidata.

[39] Note that the cross section varies between atoms according to velocity and location and between the outward and return components of the light; the value given by (13) is an average over this distribution.

[40] Stabilization to exactly identical frequencies is not possible, as appropriate lock points do not exist in the conventional Doppler-free absorption spectra.

[41] S. Utreja, H. Rathore, M. Das, and S. Panja, Frequency stabilization of multiple lasers to a reference atomic transition of Rb, Sci. Rep. **12**, 20624 (2022).

[42] A. Strangfeld, B. Wiegand, J. Kluge, M. Schoch, and M. Krutzik, Compact plug and play optical frequency reference device based on doppler-free spectroscopy of rubidium vapor, Opt. Express **30**, 12039 (2022).

[43] A. Gusching, M. Petersen, N. Passilly, D. Brazhnikov, M. Hafiz, and R. Boudot, Short-term stability of Cs microcell-stabilized lasers using dual-frequency sub-doppler spectroscopy, J. Opt. Soc. Am. B **38**, 3254 (2021).

[44] V. Maurice, C. Carlé, S. Keshavarzi, R. Chutani, S. Queste, L. Gauthier-Manuel, J. Cote, R. Vicarini, M. Abdel Hafiz, R. Boudot, and N. Passilly, Wafer-level vapor cells filled with laser-actuated hermetic seals for integrated atomic devices, Microsyst. Nanoeng. **8**, 129 (2022).

[45] D. McCarron, S. King, and S. Cornish, Modulation transfer spectroscopy in atomic rubidium, Meas. Sci. Technol. **19**, 105601 (2008).

Additive Manufacturing of functionalised atomic vapour cells for next-generation quantum technologies

F. Wang,[1] N. Cooper,[2] Y. He[1],[1] B. Hopton,[2] D. Johnson,[2] P. Zhao,[1] T. M. Fromhold,[2]
C. J. Tuck,[1] R. Hague,[1] R. D. Wildman,[1] L. Turyanska,[1] and L. Hackermüller[2]

[1] *Faculty of Engineering, University of Nottingham, University Park, Nottingham, NG7 2RD, UK**
[2] *School of Physics and Astronomy, University of Nottingham, University Park, Nottingham, NG7 2RD, UK†*

(Dated: June 24, 2024)

Atomic vapour cells are an indispensable tool for quantum technologies (QT), but potential improvements are limited by the capacities of conventional manufacturing methods. Using an additive manufacturing (AM) technique - vat polymerisation by digital light processing - we demonstrate, for the first time, a 3D-printed glass vapour cell. The exploitation of AM capacities allows intricate internal architectures, overprinting of 2D optoelectronical materials to create integrated sensors and surface functionalisation, while also showing the ability to tailor the optical properties of the AM glass by in-situ growth of gold nanoparticles. The produced cells achieve ultra-high vacuum of 2×10^{-9} mbar and enable Doppler-free spectroscopy; we demonstrate laser frequency stabilisation as a QT application. These results highlight the transformative role that AM can play for QT in enabling compact, optimised and integrated multi-material components and devices.

I. INTRODUCTION

Growing understanding of fundamental quantum processes offers benefits in multiple sectors, from medicine [1, 2] and sensing applications [3–5], positioning and security [6, 7] to quantum computing [8]. However, realising these benefits requires innovations in quantum technology (QT) hardware, which must become smaller, lighter, cheaper, and better suited to the needs of specific applications. Additive manufacturing (AM) has the potential to transform QT [9, 10] by enabling miniaturised, robust devices that can be fabricated on demand with advanced architectures for enhanced operation, such as the innovative ultra-high vacuum apparatus [11] previously reported. AM also presents opportunities for integration, both of novel hardware with existing equipment [12, 13] or of functionalised components within a larger device.

A critical QT component is the atomic vapour cell [14, 15], it underpins many technologies, spanning laser frequency stabilisation [16, 17], atom, molecule and ion-trapping [18–20] thermal vapour magnetometers [21], medical imaging [1, 2] and industrial scanning applications [22, 23]. However, vapour cells are difficult to manufacture, rely on the art of glass-blowing and are consequently limited in size and shape. They are usually cylindrical with dimensions on the order of centimetres, and have only limited scope for miniaturisation or customisation.

Planar lithographic processes [24, 25] and microelectromechanical systems (MEMS) with anodic bonding [26–28] can produce microfabricated cells with great potential for miniaturisation, but lack 3D-versatility and offer only two optical interfaces, which is insufficient for some applications; nor do they have the same transformative potential for integration and customisation as AM.

Additive manufacturing can provide the means to overcome these limitations. AM of glass was demonstrated using fused filament fabrication of molten glass [29, 30], selective laser melting with silica powder [31, 32] and direct ink writing using silica sol-gel inks [33]. However, significant technological challenges such as limited building resolution, evident surface roughness, cracking and low optical transparency have also been identified. Glass printing via the use of photocurable polymer / silica nanoparticle composites has led to optically useful constructs [34–39], but to date, the use of these formulations has been limited to structural ornaments, classical optics and fluidics.

Here we provide the first demonstration of an ultra-high vacuum (UHV) compatible AM glass QT component and show that, by modifying the inks and printing procedures, transparent printed structures with integrated active elements (i.e. electronics, photodetectors) can be realised. These structures are of high optical quality, have the potential to transform vapour cell based QTs and open a route to the scalable manufacture of key components for spectroscopy and quantum sensing (Figure 1a)).

We describe the fabrication of glass vapour cells with sizes < 1 cm^3 by a vat polymerisation method based on digital light processing (DLP) of high loading silica nanoparticles resins (Figure 1b). As a QT application, the cells are used to demonstrate atomic spectroscopy and show excellent vacuum performance, with pumped cells reaching pressures below 2×10^{-9} mbar and sustaining this pressure throughout the experiments. The cells were thermally tested up to 150°C and were not noticeably degraded by exposure to high-temperature Rb vapour.

We performed atomic vapour spectroscopy within the cells and demonstrated its application to laser frequency

* ppzfw@exmail.nottingham.ac.uk
† nathan.cooper@nottingham.ac.uk

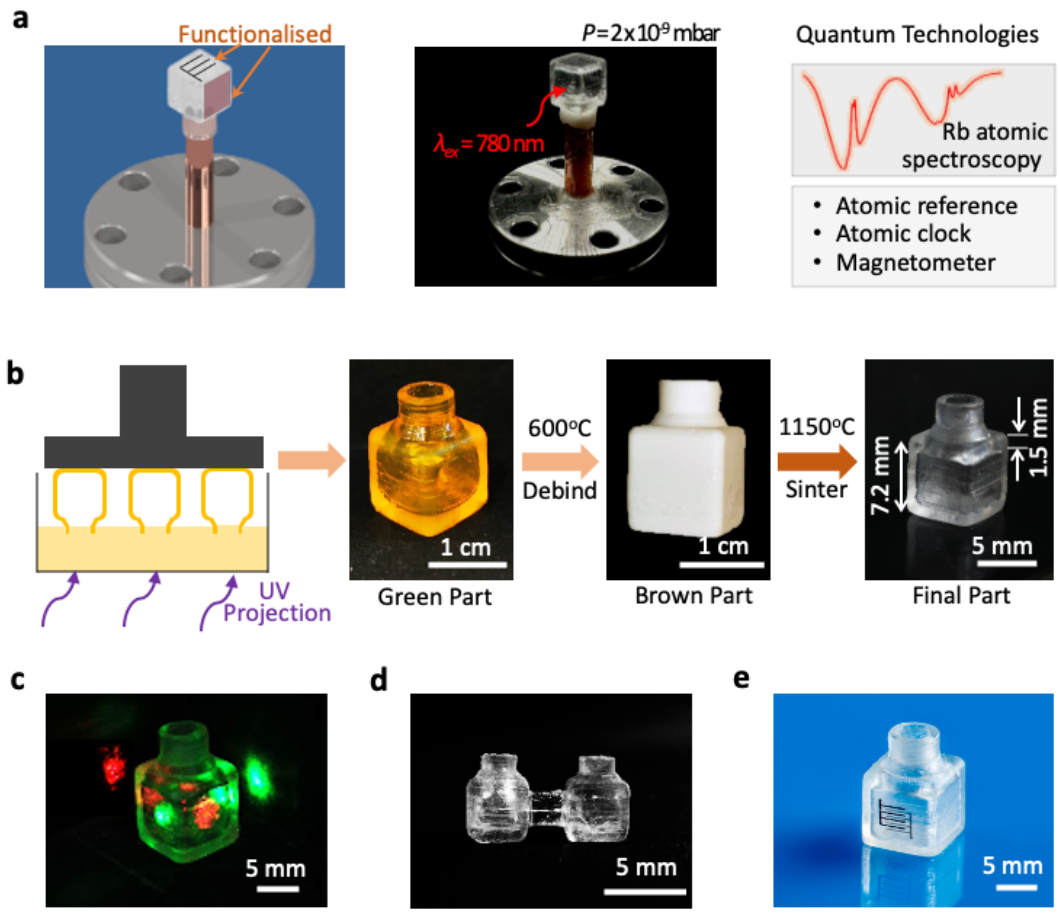

FIG. 1. **Additive manufacturing of a vapour cell for QT applications.** **a** Schematic diagram of the AM vapour cell for QT applications. Left: Illustration of the design of the cell mounted on an ultra-high vacuum flange via a copper tube. Middle: The photo of AM cell mounted for pumping to a pressure of 2×10^{-9} mbar and loading with Rb atomic vapour. Right: Doppler-free pump-probe absorption spectroscopy of Rb vapour in the AM vapour cell and applications for QT. **b** Vat polymerisation of glass vapour cells via DLP and optical images of the printed green, brown and final parts following debinding and sintering steps. **c** Photograph of the printed cell with red and green laser beams propagating through the cell. **d** New structures are achievable: photograph of two inter-connected cells. **e** Integrated functionalisation: Inkjet printed graphene and silver inter-digit electrodes for direct photon detection on the cell.

stabilisation [40] on the D2 line of ^{85}Rb.

The fabrication methodology is further applied to create complex cell geometries, while in-situ growth of metal nanoparticles is used to selectively tune the optical transmission of the produced glass, providing a clear demonstration of the versatility and transformative potential of such a method for creating optical materials for QT.

These functionalised cells enable exciting applications, e.g. for the creation of sub-cm sized optically pumped magnetometers incorporating magnetic-field shielding conductors and photodetectors directly printed on the cell, thereby providing a significant jump in system flexibility and imaging resolution for non-invasive magnetoencephalography [41].

II. RESULTS AND DISCUSSION

A. Additive manufacturing of a vapour cell

To manufacture the glass vapour cell (Figure 1), a resin was formulated based on [34] containing fumed silica nanoparticles with an average size of 40 nm, dispersed in a mixture of 2-hydroxyethyl methacrylate (HEMA), tetra(ethylene glycol) diacrylate (TEGDA) and phenoxyethanol (POE). HEMA forms a solvation layer on the nanoparticles, hence allowing high silica loading of the resin. TEGDA is used to improve cross-linking, thus strengthening the mechanical structure of the printed part. A concentration of 50 wt% silica nanoparticles was achieved following a multi-step homogenising process [42]. The viscosity of the resin was measured to be 297 mPa·s at a shear rate of 1000 s^{-1}. For demonstra-

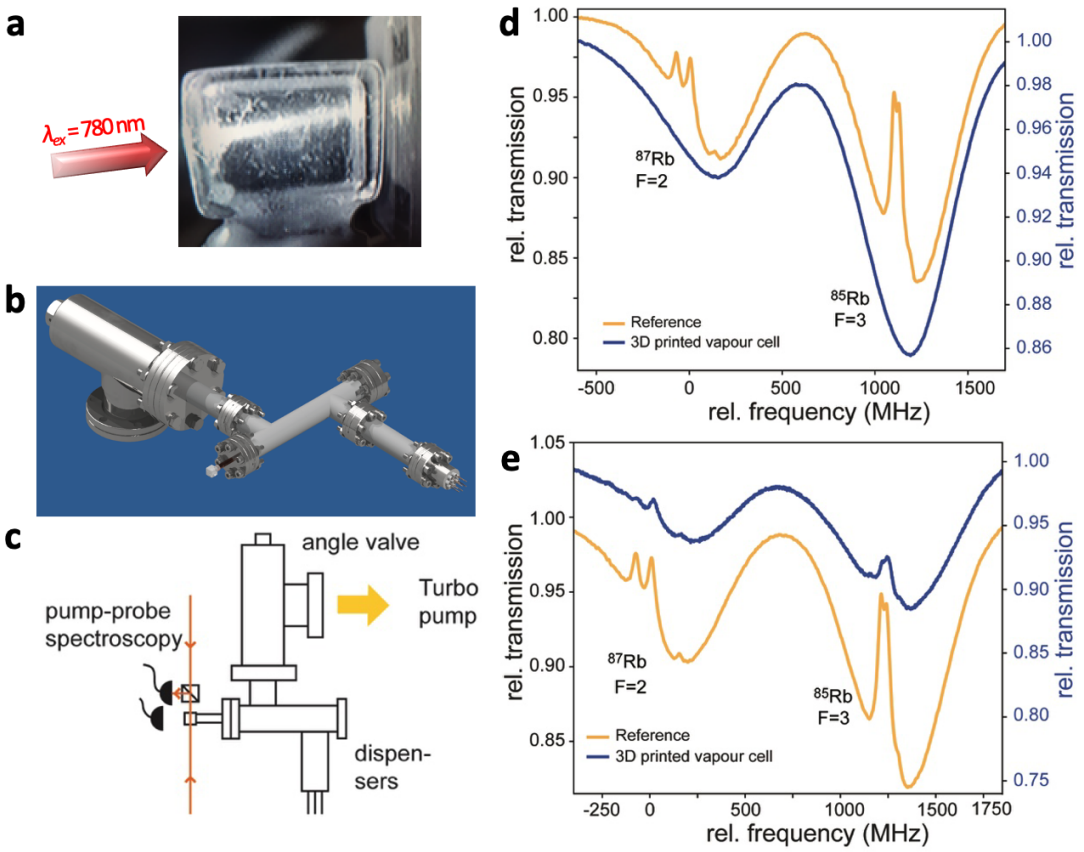

FIG. 2. **Absorption spectroscopy of Rb vapour in the AM vapour cell. a** Rb fluorescence image inside the cell under exposure to $\lambda_{ex} = 780\,\text{nm}$ laser light. **b** and **c** CAD model and a scheme of the vacuum and optical setups. **d** Single beam absorption spectroscopy. The scale of the reference signal (yellow) is vertically offset by 0.02 for clarity. The frequency scale in d and e is set relative to the ^{87}Rb $F = 2 \rightarrow F' = 2 \times 3$ transition. **e** Doppler-free pump-probe absorption spectroscopy. For clarity, the scale of the reference signal (yellow) is vertically offset by -0.05.

tion purposes, and to facilitate comparison with existing vapour cells used in commercial QTs, our cells have a cuboid shape featuring two pairs of parallel optical interfaces, in contrast to the single pair of parallel interfaces in wafer-based cells [43] and most glass-blown cells. The intended cell dimensions were 7.2 mm (L) × 7.2 mm (W) × 7.2 mm (H) with 1.5 mm wall thickness; the initial print was therefore 1 cm^3 with 2 mm thick walls, to allow for shrinkage. An inlet on one side (Figure 1b) enables vapour loading and connection to our experimental apparatus.

To optimise the degree of curing during printing and obtain a high shape fidelity between the printed part and the design, the exposure time of each layer and the concentration of the absorber was adjusted by measuring the curing depth with different absorber concentrations (Appendix A1, Figure A1). The optimal degree of polymerisation, curing depth and shape fidelity, was achieved with 6.5 s exposure time, 45 mW/cm^2 intensity and 0.035 wt% absorber content. A simulation of light-scattering from the silica nanoparticles showed an anisotropic distribution, however an isotropic degree of polymerisation can be achieved using this resin composition (Appendix A2, Figure A2).

The residual uncured resin was removed in washing and post-curing steps, resulting in a green part with good mechanical strength. Thermal debinding followed, with a gradual and uniform release of the internal mechanical stress, which was tailored to avoid cracking or collapse of the structure. The resulting debound porous brown part maintained the same geometry as the green part without volume shrinkage, but with a 51% weight loss as a consequence of the debinding process.

To eliminate porosity, the part was sintered in an inert argon atmosphere at a temperature of $T = 1150\,^{\circ}\text{C}$ for 12 h. This process allows the silica nanoparticles to merge and form amorphous glass (Figure A3). We note that the argon atmosphere prevents the risk of crystallisation, which was previously observed in synthesis of parts in the presence of oxygen [44]. X-ray diffraction (XRD) analysis confirmed the amorphous structure of the printed material (Figure A3a) [45]. The density of the sintered part is 2.2 gcm^{-3} and the sintered part had no observable porosity (see SEM images in Figure A3b)). The

cells printed using this formulation show high mechanical stability under external pressures and good optical flatness/transparency (see below) and enabled us to achieve and retain vacuum down to 2×10^{-9} mbar.

For our formulation, we observed $\sim 27\%$ linear shrinkage, both horizontally and vertically. The shrinkage of the part matched the estimation based on the solid weight concentration of the silica [42] and was accounted for in the design. The two pairs of parallel transparent flat surfaces of the cells allow two perpendicular beams to pass through with minimal distortion (Figure A1c). An additional polishing step (Grit 1000 polishing paper) was introduced to reduce outer wall roughness.

B. QT sensing with an additively manufactured cell

To demonstrate the suitability of the printed cells for quantum technology applications, we performed rubidium spectroscopy in the cell. For this, the cell was mounted to an ultra-high vacuum (UHV) flange via an annealed copper tube (Figure 2a) and connected to a vacuum test system (Figure 2b). The cells were leak tested and found to retain pressures down to 2×10^{-9} mbar. The annealed copper tube allows for a separation of the cells from the vacuum apparatus after evacuation and use of the cell as a stand-alone device, via a standard copper pinch-off technique. The cell was then filled with a mixture of ^{85}Rb and ^{87}Rb via atomic dispensers. The geometry of the cell is also compatible with alternative filling methods, reported previously [43, 46]. The cell performance was first characterised through single-pass absorption spectroscopy. A single-mode, Gaussian laser beam with a diameter of 1.25 mm, a wavelength of 780 nm and a power of 0.06 mW was passed through the printed cell and detected on a photodiode (see Figure 2c). The transmission through the cell without Rb vapour is $> 90\,\%$.

The frequency of the laser light was scanned across the D2 resonance of rubidium 85 and fluorescence observed (inset of Figure 2a). The single-pass transmission spectrum (Figure 2d) displays the typical Voigt-profiles with all expected features. The yellow line shows Doppler-free absorption spectroscopy for comparison - this was obtained with a standard, commercial 75 mm long glass cell. The Doppler-valleys corresponding to the D2 absorption lines of ^{85}Rb and ^{87}Rb are clearly resolved, showing single pass absorption along the ^{87}Rb $F = 2$ transition manifold and the ^{87}Rb $F = 3$ transition manifold (Figure 2d). The frequency axis in Figure 3e is given relative to the ^{87}Rb $F = 2 \rightarrow F' = 2 \times 3$ transition. As an example of QT-sensing, Doppler-free saturated absorption spectroscopy was demonstrated with the cell at room temperature. Counter-propagating linearly polarised beams with powers of 0.06 mW (probe) and 0.3 mW (pump) were set up as shown in Figure 2c. The transmission of the probe beam (blue line in Figure 2e) shows the Doppler-free spectrum that allows the resolution of the hyperfine states, ^{87}Rb $F = 2 \rightarrow F' = 1, 2, 3$ and ^{85}Rb $F = 3 \rightarrow F' = 2, 3, 4$ (Figure 5e).

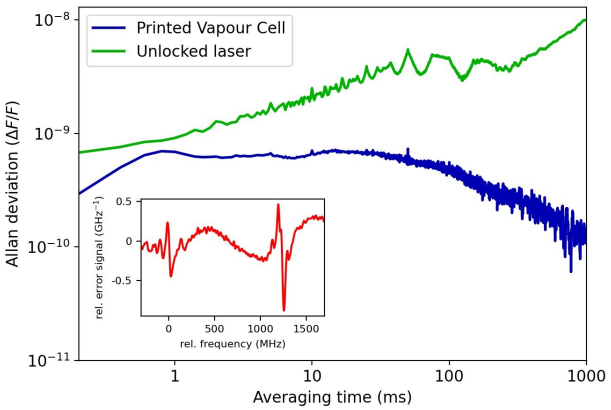

FIG. 3. **Allan deviation of the unlocked laser, and with the laser locked using the printed vapour cell.** Inset: The error signal (red) is shown for reference.

Doppler-free spectroscopy enables laser frequency stabilisation ("locking") to the hyperfine transitions. We stabilised a laser to the ^{85}Rb $F = 3 \rightarrow F' = 3 \times 4$ crossover transition and thus demonstrated that the cell can be used as a frequency standard. The laser current was modulated with a frequency of 100 kHz, the photodiode signal was demodulated and an error signal obtained that corresponds to the derivative of the spectroscopy signal. This signal was used to frequency-stabilise the laser through feedback to the laser diode drive current.

To analyse the resulting frequency stability, the error signal was recorded over a period of twenty minutes, while the laser was frequency locked via the signal from the printed vapour cell. By analysing the error signal, the Allan deviation was obtained for the locked laser and compared to the unlocked or free-running laser (see Figure 3).

The stabilisation based on the printed vapour cell reaches $\Delta F/F = 2 \times 10^{-10}$ at long interrogation times ($t \sim 1\,s$), an improvement of 1-2 orders of magnitude in comparison with the free-running laser, and provides significant stability improvements on all time scales. This demonstrates that the printed vapour cell can provide stable, Doppler-free laser locking. A similar setup based on polarisation can be used to operate the cell as a magnetometer [43, 47]. We compared the locking performance to a standard 75 mm long commercial vapour cell (Thorlabs, made by conventional glass blowing); taking the 15 times difference in optical path length into account, the Allan deviation normalised to optical path length is similar or slightly better for the printed cell (Figure A5).

To evaluate the applicability of printed vapour cells for magnetometry and polarisation dependent QT applications, the effect of the printed cell on beam shape

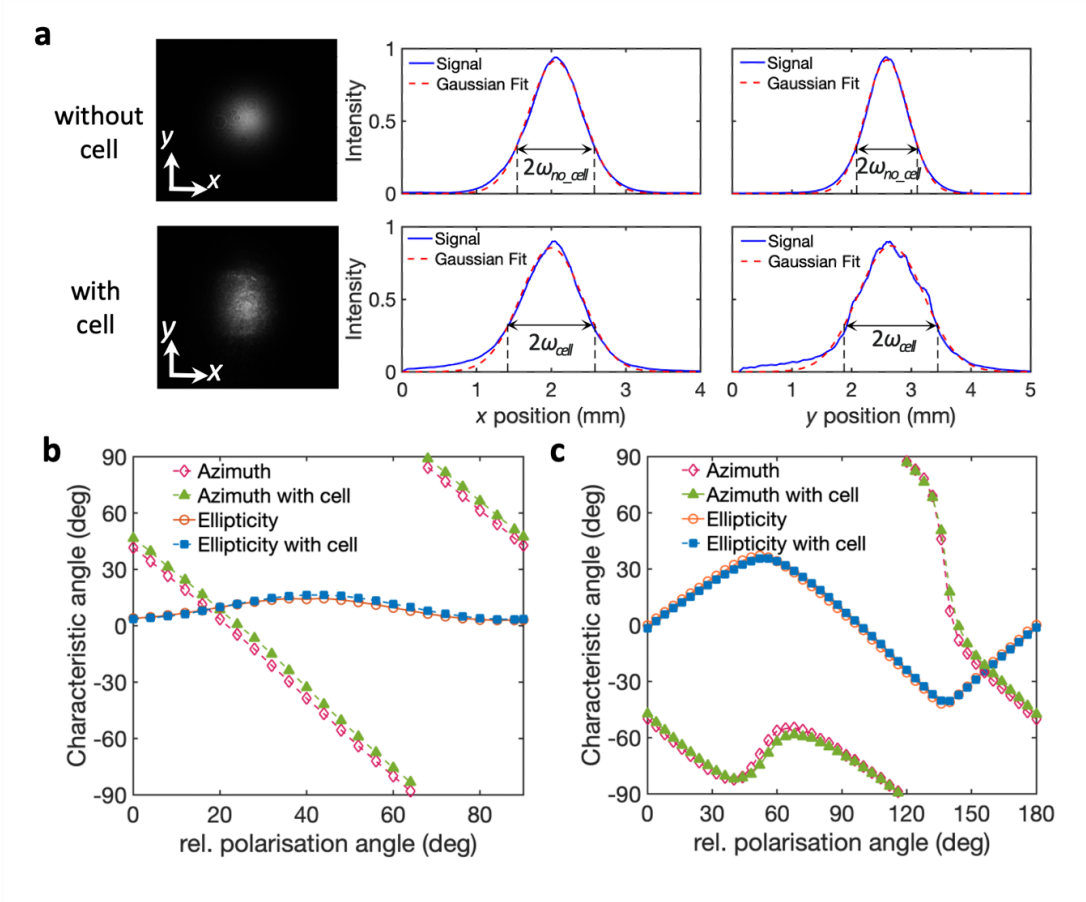

FIG. 4. **Transmission and polarisation measurement of the AM vapour cell. a** Beam profile of a 780 nm test laser beam with and without passing through the cell.**b** Azimuth and ellipticity measured using a polarisation analyser for varying angles of polarisation, with and without the presence of the printed vapour cell, for initially linearly polarised light. **c** The Azimuth and ellipticity for varying angles of a preceding quarter-waveplate, with and without the presence of the printed vapour cell, for initially linearly polarised light.

and the polarisation of laser light (780 nm) was investigated with an internal vacuum of 2×10^{-9} mbar. By analysing the Gaussian beam profile with and without the cell in the optical path, negligible distortion and a slight increase of the beam waist from the horizontally printed faces as shown in Figure 4a. For the vertically printed faces, the beam waist increased by $\sim 50\%$ [$\omega_{\text{no\_cell}} = (0.51 \pm 0.1)$ mm and $\omega_{\text{cell}} = (0.78 \pm 0.1)$ mm] most likely due to curvature of the internal surface, which can be considered in future designs. Small undulations are caused by the layer-by-layer printing process.

The effect of the printed vapour cell on polarisation was analysed, for linearly polarised light, for various input polarisation angles obtained via tuning of a half-wave plate, with a measurement of the azimuth and ellipticity taken every 4° using a polarisation analyser. The measurements with and without the printed vapour cell (Figure 4b) revealed negligible change (comparable to the resolution of the instrument) of azimuth and ellipticity when the cell is present in the optical path. The half-wave plate was then switched for a quarter-wave plate and the same measurement technique was repeated, to study the effect of the cell on elliptically polarised light. The results are shown in Figure 5c.

C. Functionalisation of AM vapour cell

Our method of 3D-printing vapour cells offers exceptional opportunities for improved quantum technologies. We are able to demonstrate a range of desirable features for vapour cell performance that are only made possible through additive manufacturing. The geometric design freedom of AM enabled printing of two inter-connected cells with a variable length tube (two 4.5 mm cuboid cells connected with a 3 mm channel, Figure 1d), thus offering increased optical depth, while by overprinting the cell with conductive materials (Figure 1e) we demonstrate integration and compactification potential for sensors and detectors. Tuneable modification of the optical transparency of 3D printed glass has previously been achieved by dipping the brown part into solutions containing metal

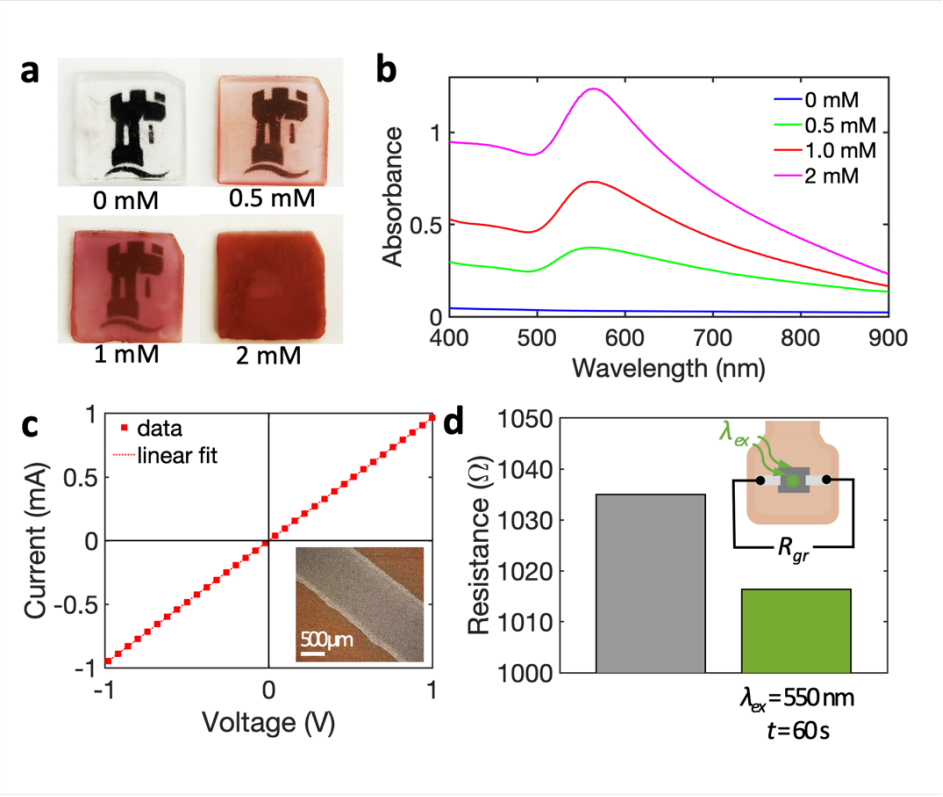

FIG. 5. **Functionalisation of AM glass - AuNP doping and graphene tracks. a** Photographs of printed glass slabs of 1.25×1.25 cm, with different concentrations of AuNP dopant, positioned over the University of Nottingham logo. **b** Measured absorbance of glass printed with different concentrations of AuNP dopant. **c** Representative I(V) dependence of a graphene track (10 mm by 2 mm) inkjet printed onto the 0.5 mM AuNP doped glass and (inset) optical microscopy image of the printed graphene track. **d** Electrical resistance, Rgr, of the graphene track printed onto an AuNP doped glass slab (0.5mM) measured in the dark and under continuous illumination with green laser light ($\lambda = 550$ nm, $P = 25$ mW). Inset: Schematic of the measurement scheme.

salts [34, 48**?**]. We propose a facile method where AuNP are formed in situ to modify the glass absorption in the visible wavelength range.

Gold salt, $AuCl_3$, was added to the resin before printing to form Au nanoparticles (AuNPs) in situ by a photothermal reduction process, thereby causing the glass to acquire a cranberry-red colour [49]. An absorption peak, characteristic of AuNPs, was observed at a wavelength of ~ 565 nm (Figure 5b) for the glass produced with 1 mM of $AuCl_3$, indicating the formation of AuNPs with a size of ~ 20 nm. By varying the $AuCl_3$ concentration from 0 to 2 mM, the colour of the resulting glass changes to dark deep red (Figure 5a), indicating the formation of larger size AuNPs, and the absorption peak shifts to a longer wavelength from 562 nm for 0.5 mM to 567 nm for 2 mM (Figure 5b). Importantly, the doped glass retains sufficient optical transparency in the near infrared range, as required for Rb atomic spectroscopy, while filtering out shorter wavelength visible light from environmental sources. In the context of magnetometer cells, doped glass offers the exciting exploitation of surface plasmon resonances (SPR) of AuNP for local optically-activated heating, which can be used to achieve higher vapour pressure in the cell faster than standard current-based heating methods [50].

To demonstrate SPR, we inkjet printed a graphene (iGr) track (10 mm (L) × 2 mm (W)) onto one side of the glass slab as shown in Figure 5c. Upon exposure of the undecorated side of the AuNP-glass to green laser light ($\lambda = 550$ nm), the resistance of the graphene track decreased by 2% in 60 s (Figure 5d), which is a typical change in resistance expected for a temperature increase of 30 °C. An equivalent track on undoped glass produced no detectable response under the same conditions (Figure A4a), confirming that the localised heating was generated by SPR of AuNPs. For medical sensing applications, e.g. magnetometry for brain imaging, this is a very relevant feature as the vapour pressure can be increased without heating coils and without raising the temperature of the environment; this reduces power dissipation and the need for thermal insulation, hence allowing the sensor to be brought closer to the tissues being studied. The technique also enables glass with a customisable optical absorption range within one glass structure (see Figure A4 b)).

Similarly to the overprinted graphene path, the vapour

cell can be surface-decorated with other functional materials, including conductive layers/devices that can be inkjet printed onto the cell. A pair of 300 µm wide interdigitated conductive tracks was deposited using inkjet printing of silver nanoparticle ink and graphene inks (Figure 1e), with a sheet resistance of 0.53 Ω/sq and 207 Ω/sq respectively, which is comparable to the values achieved on other substrates [51, 52]. The conductive tracks exhibit good adhesion to the printed glass cell, enabling e.g. heating or magnetic field shielding elements that are co-manufactured with, and integral to, the vapour cell. The AM build process also facilitates integration of other active components, such as inkjet-printed perovskite photon sensors [53], which can be used for in situ monitoring.

III. CONCLUSIONS

Additive manufacturing of transparent glass elements has immense potential to improve components for quantum technologies. A glass vapour cell has been produced by digital light processing and a wide range of functionalisation capabilities have been demonstrated, including integrated 3D printed electronics and active optoelectronic components for enhanced device functionality, and wavelength-selective absorption for surface plasmonic heating.

The printed vapour cell was successfully pumped to the UHV regime (2×10^{-9} mbar) and loaded with atomic rubidium vapour. The cell exhibits high transparency and polarisation stability, enabling the observation of atomic spectroscopy, including signature Doppler-valley and sub-Doppler features. Used as a frequency reference, laser stabilisation has been achieved with an Allan deviation $\Delta F/F < 10^{-9}$, limited by electronic feedback hardware, not the AM vapour cell.

This work will inspire new AM-QT research directions, for example, how the sensitivity of a spin-exchange relaxation-free magnetometer based on modified surfaces in a 3D printed vapour cell compares to established designs [27]. The process could enable manufacture of > 40 glass cells (green parts) per lab-based printer per hour and the times required for debinding and sintering each cell could be effectively shortened with large volume furnaces.

Our methods open the way for the creation of novel, high-performance sensors based on functionalised glass vapour cells for enhanced quantum technology devices, such as magneto-encephalography sensors or atomic clocks. The upscalability of the AM process, together with good optical quality and high vacuum performance, makes such devices a scalable, convenient and customisable fabrication solution for many QT application sectors.

DATA AVAILABILITY STATEMENT

The data used in this work are available from the corresponding author upon reasonable request.

ACKNOWLEDGEMENTS

The fabrication work of the glass vapour cell was supported by EPSRC grants EP/P031684/1, EP/T001046/1 and EP/M013294/1. The characterisation work was supported by IUK project No.133086, EPSRC grants EP/T001046/1, EP/R024111/1 and EP/M013294/1, and by the European Comission grant ErBeStA (no. 800942).

EXPERIMENTAL METHODS

Resin formulation: A mixture of 60 vol% 2-hydroxyethyl methacrylate (HEMA), 10 vol% tetra (ethylene glycol) diacrylate (TEGDA) and 30 vol% phenoxyethanol (POE) was prepared, and blended with 0.2 wt% of bis (2,4,6 trimethylbenzoyl)phenylphosphineoxide as a photoinitiator, 0.1 wt% of hydroquinone monomethyl ether as an inhibitor and 0.035 wt% of Sudan Orange UV absorber. Aerosil OX50 silica nanopowder (50 wt%) was added in 10 small doses with 15 min bath sonication to prevent agglomeration. The final slurry was further bath sonicated for 30 mins and then degassed at a low pressure of 200 mbar for 3 min.

Additive manufacturing process: The design was printed on a Cellink Lumen X printer (45 mW/cm^2 UV power intensity at 405 nm) with 50 μm hatching distance and 6.5 s exposure time for each layer. The printed part was immersed in propylene glycol methyl ether acetate (PGMEA) and washed using a tube roller at 80 rpm for 5 minutes to remove the residual non-polymerised material. The washing cycle was repeated three times. Then the part was exposed to ultraviolet floodlight using a Wicked Curebox for 10 minutes for post-curing.

Post-process debinding and sintering: The green part was debound in a high-temperature furnace (Carbolite HRF 7/22 box furnace) with the ambient temperature being increased at 0.35°C/min to $T = 130$°C, held at this temperature for 2 hours, then increased at the same rate to 320°C for 4 hours and 600°C for 2 hours. The resulting brown part was further sintered at $T = 1150$°C for 12 hours with 3°C/min heating and cooling rates under 1 bar argon flow using a tube furnace (Carbolite STF 15/50).

Functionalisation: Doping with Au nanoparticles was achieved by adding $AuCl_3$ to the resin, with final concentrations of 0.5 mM, 1 mM and 2 mM, before adding fumed silica powder. Conductive tracks were

deposited with a 300 μm wide interdigitated design using a Dimatix DMP-2831 inkjet printer and a Samba cartridgeof 2.4 pL drop volume. Three layers of AgNP ink (XTPL IJ36) were deposited using a 20 μm drop spacing and ten layers of graphene ink (Merck 793663) were printed using 10 μm drop spacings.

Electrical and optical characterisation: The sheet resistance of the printed silver and graphene samples was measured using a Keithley 2400 sourcemeter and a micromanipulator with a four-probe method, also known as the Kelvin technique, to eliminate contact resistance. Each I-V curve was measured three times using both forward and backwards scanning. The derivative of the I-V curve reveals the conductivity of the printed line with the exact geometry measured by an optical microscope.

Characterisation of polarised light: The laser beam was set up to pass through a linear polariser and a waveplate (either quarter-wave or half-wave as appropriate), before passing through the printed vapour cell, which was under internal vacuum so that no gases in the cell could alter the polarisation.

Atomic spectroscopy: The cell was connected to a UHV-flange via an annealed copper tube and attached to the tube using UV-curing glue (Dymax OP-67-LS). The system shown in Fig. 2b was used to demonstrate the vacuum compatibility of the cells. Following bake-out for 24hrs at 150°C and leak-testing, pressures down to 2×10^{-9} mbar were achieved. Laser light resonant with the rubidium absorption lines from a Toptica 110 tapered amplifier laser was then guided into the cell and the resulting absorption measured on a Thorlabs DET10A amplified photodiode. Doppler-free spectroscopy was obtained using a pump-probe setup as shown in Fig. 2b with 0.06 mW probe beam power and 0.3 mW pump beam power in beams with a diameter of 1.25 mm. The commercial reference vapour cell of $\varnothing$25.4mm $\times$ 71.8 mm was purchased from Thorlabs (GC25075-RB). For laser locking with this commercial cell, the probe beam is retro-reflected back through the cell, instead of separate probe and pump beams.

[1] N. Aslam, H. Zhou, E. K. Urbach, M. J. Turner, R. L. Walsworth, M. D. Lukin, and H. Park, Quantum sensors for biomedical applications, Nature Reviews Physics **5**, 157 (2023).

[2] E. Boto, N. Holmes, J. Legget, G. Roberts, V. Shah, S. Meyer, L. Munoz, K. Mullinger, T. Tierney, S. Bestmann, G. Barnes, R. Bowtell, and M. Brookes, Moving magnetoencephalography towards real-world applications with a wearable system, Nature **555**, 657 (2018).

[3] Y. Arita, M. Mazilu, and K. Dholakia, Laser-induced rotation and cooling of a trapped microgyroscope in vacuum, Nature communications **4**, 2374 (2013).

[4] K. Bongs, M. Holynski, J. Vovrosh, P. Bouyer, G. Condon, E. Rasel, C. Schubert, W. Schleich, and A. Roura, Nature Reviews Physics **1**, 731 (2019).

[5] J. Lee, M. Lisanti, W. A. Terrano, and M. Romalis, Laboratory constraints on the neutron-spin coupling of fevscale axions, Phys. Rev. X **13**, 011050 (2023).

[6] D. Feng, Review of quantum navigation, in *IOP Conference Series: Earth and Environmental Science*, Vol. 237 (IOP Publishing, 2019) p. 032027.

[7] B. Stray, A. Lamb, A. Kaushik, J. Vovrosh, A. Rodgers, J. Winch, F. Hayati, D. Boddice, A. Strabawa, and A. Niggebaum, Quantum sensing for gravity cartography, Nature **602**, 590 (2022).

[8] S. J. Evered, D. Bluvstein, M. Kalinowski, S. Ebadi, T. Manovitz, H. Zhou, S. H. Li, A. A. Geim, T. T. Wang, N. Maskara, H. Levine, G. Semeghini, M. Greiner, V. Vuletic, and M. D. Lukin, High-fidelity parallel entangling gates on a neutral-atom quantum computer, Nature **622**, 268 (2023).

[9] P. Ruchka, S. Hammer, M. Rockenhäuser, R. Albrecht, J. Drozella, S. Thiele, H. Giessen, and T. Langen, Microscopic 3d printed optical tweezers for atomic quantum technology, Quantum Science and Technology **7**, 045011 (2022).

[10] J. Vovrosh, G. Voulazeris, P. Petrov, J. Zou, Y. Gaber, L. Benn, D. Woolger, M. M. Attallah, V. Boyer, K. Bongs, and M. Holynski, Additive manufacturing of magnetic shielding and ultra-high vacuum flange for cold atom sensors, Scientific Reports **8**, 2023 (2018).

[11] N. Cooper, L. Coles, S. Everton, I. Makery, R. Campion, S. Madkhaly, C. Morley, J. O'Shea, W. Evans, R. Saint, P. Krüger, F. Orucevic, C. Tuck, R. Wildman, T. Fromhold, and L. Hackermüller, Additively manufactured ultra-high vacuum chamber for portable quantum technologies, Additive Manufacturinig **40**, 101898 (2021).

[12] S. Madkhaly, L. Coles, C. Morley, C. Colquhoun, T. Fromhold, N. Cooper, and L. Hackermüller, Performance-optimized components for quantum technologies via additive manufacturing, PRX Quantum **2**, 030326 (2021).

[13] H. Stærkind, K. Jensen, J. H. Müller, V. O. Boer, E. T. Petersen, and E. S. Polzik, Precision measurement of the excited state landé g-factor and diamagnetic shift of the cesium d_2 line, Phys. Rev. X **13**, 021036 (2023).

[14] L. A. Liew, S. Knappe, J. Moreland, H. Robinson, L. Hollberg, and J. Kitching, Microfabricated alkali atom vapor cells, Applied Physics Letters **84**, 2694 (2004).

[15] V. Maurice, C. Carle, S. Keshavarzi, R. Chutani, S. Queste, L. Gauthier-Manuel, J.-M. Cote, R. Vicarini, M. Abdel Hafiz, R. Boudot, and N. Passilly, Wafer-level vapor cells filled with laser-actuated hermetic seals for integrated atomic devices, Microsystems & Nanoengineering **8**, 129 (2022).

[16] N. Cooper, S. Madkhaly, D. Johnson, B. Hopton, D. Baldolini, and L. Hackermüller, Dual-frequency doppler-free spectroscopy for simultaneous laser stabilization in compact atomic physics experiments, Phys. Rev. A **108**, 013521 (2023).

[17] G. D. Martinez, C. Li, A. Staron, J. Kitching, C. Raman, and W. R. McGehee, A chip-scale atomic beam clock, Nature Communications **14**, 3501 (2023).

[18] N. B. Vilas, C. Hallas, L. Anderegg, P. Robichaud, A. Winnicki, D. Mitra, and J. M. Doyle, Magneto-optical trapping and sub-doppler cooling of a polyatomic molecule, Nature **606**, 70 (2022).

[19] H. Häffner, C. Roos, and R. Blatt, Quantum computing with trapped ions, Physics Reports **469**, 155 (2008).

[20] C. D. Marciniak, T. Feldker, I. Pogorelov, R. Kaubrugger, D. V. Vasilyev, R. van Bijnen, P. Schindler, P. Zoller, R. Blatt, and T. Monz, Optimal metrology with programmable quantum sensors, Nature **603**, 604 (2022).

[21] A. Fabricant, I. Novikova, and G. Bison, How to build a magnetometer with thermal atomic vapor: a tutorial, New Journal of Physics **25**, 025001 (2023).

[22] A. Pross, A. Crisan, S. Bending, V. Mosser, and M. Konczykowski, Second-generation quantum-well sensors for room-temperature scanning hall probe microscopy, Journal of Applied Physics **97**, 0964105 (2005).

[23] M. Behzadirad, S. Mecholdt, J. N. Randall, J. B. Ballard, J. Owen, A. K. Rishinaramangalam, A. Reum, T. Gotszalk, D. F. Feezell, I. W. Rangelow, *et al.*, Advanced scanning probe nanolithography using gan nanowires, Nano Letters **21**, 5493 (2021).

[24] Y. Pétremand, C. Affolderbach, R. Straessle, M. Pellaton, D. Briand, G. Mileti, and N. F. de Rooij, Microfabricated rubidium vapour cell with a thick glass core for small-scale atomic clock applications, Journal of Micromechanics and Microengineering **22**, 025013 (2012).

[25] V. Shah, S. Knappe, P. D. Schwindt, and J. Kitching, Subpicotesla atomic magnetometry with a microfabricated vapour cell, Nature Photonics **1**, 649 (2007).

[26] F. Gong, Y.-Y. Jau, K. Jensen, and W. Happer, Electrolytic fabrication of atomic clock cells, Rev. Sci. Instrum. **77**, 076101 (2006).

[27] W. C. Griffith, S. Knappe, and J. Kitching, Femtotesla atomic magnetometry in a microfabricated vapor cell, Optics Express **18**, 27167 (2010).

[28] C. H. Lee, H. Guo, S. Radhakrishnam, A. Lal, C. Szekely, T. McClelland, and A. P. Pisano, in *Proc. Solid-State Sensors, Actuators and Microsystems Workshop (Hilton Head Island, SC, 6–10 June 2004)* (2004).

[29] J. Luo, L. J. Gilbert, C. Qu, R. G. Landers, D. A. Bristow, and E. C. Kinzel, Additive manufacturing of transparent soda-lime glass using a filament-fed process, Journal of Manufacturing Science and Engineering **139**, 061006 (2017).

[30] C. Inamura, M. Stern, D. Lizardo, P. Houk, and N. Oxman, Additive manufacturing of transparent glass structures, 3D Printing and Additive Manufacturing **5**, 269 (2018).

[31] K. C. Datsiou, E. Saleh, F. Spirrett, R. Goodridge, I. Ashcroft, and D. Eustice, Additive manufacturing of glass with laser powder bed fusion, Journal of the American Ceramic Society **102**, 4410 (2019).

[32] J. Lei, Y. Hong, Q. Zhang, F. Peng, and H. Xiao, Additive manufacturing of fused silica glass using direct laser melting, in *CLEO: Applications and Technology* (Optica Publishing Group, 2019) pp. AW3I–4.

[33] K. Sasan, A. Lange, T. D. Yee, N. Dudukovic, D. T. Nguyen, M. A. Johnson, O. D. Herrera, J. H. Yoo, A. M. Sawvel, M. E. Ellis, *et al.*, Additive manufacturing of optical quality germania–silica glasses, ACS applied materials & interfaces **12**, 6736 (2020).

[34] F. Kotz, K. Arnold, W. Bauer, D. Schild, N. Keller, K. Sachsenheimer, T. M. Nargang, C. Richter, D. Helmer, and B. E. Rapp, Three-dimensional printing of transparent fused silica glass, Nature **544**, 337 (2017).

[35] I. Cooperstein, E. Shukrun, O. Press, A. Kamyshny, and S. Magdassi, Additive manufacturing of transparent silica glass from solutions, ACS applied materials & interfaces **10**, 18879 (2018).

[36] D. G. Moore, L. Barbera, K. Masania, and A. R. Studart, Three-dimensional printing of multicomponent glasses using phase-separating resins, Nature materials **19**, 212 (2020).

[37] J. T. Toombs, M. Luitz, C. C. Cook, S. Jenne, C. C. Li, B. E. Rapp, F. Kotz-Helmer, and H. K. Taylor, Volumetric additive manufacturing of silica glass with microscale computed axial lithography, Science **376**, 308 (2022).

[38] F. Kotz, A. S. Quick, P. Risch, T. Martin, T. Hoose, M. Thiel, D. Helmer, and B. E. Rapp, Two-photon polymerization of nanocomposites for the fabrication of transparent fused silica glass microstructures, Advanced Materials **33**, 2006341 (2021).

[39] D. Han, C. Yang, N. X. Fang, and H. Lee, Rapid multi-material 3d printing with projection micro-stereolithography using dynamic fluidic control, Additive Manufacturing **27**, 606 (2019).

[40] N. Cooper, S. Madkhaly, D. Johnson, B. Hopton, D. Baldolini, and L. Hackermüller, Dual-frequency doppler-free spectroscopy for simultaneous laser stabilization in compact atomic physics experiments, Phys. Rev. A **108**, 013521 (2023).

[41] M. J. Brookes, J. Legget, M. Rea, R. M. Hill, N. Holmes, E. Boto, and R. Bowtell, Magnetoencephalography with optically pumped magnetometers (opm-meg): the next generation of functional neuroimaging, Trends in Neurosciences **45**, 621 (2022).

[42] P. Cai, L. Guo, H. Wang, J. Li, J. Li, Y. Qiu, Q. Zhang, and Q. Lue, Effects of slurry mixing methods and solid loading on 3d printed silica glass parts based on dlp stereolithography, Ceramics International **46**, 16833 (2020).

[43] V. G. Lucivero, A. Zanoni, G. Corrielli, R. Osellame, and M. W. Mitchell, Laser-written vapor cells for chip-scale atomic sensing and spectroscopy, Opt. Express **30**, 27149 (2022).

[44] O. Yong-Taeg, S. Fujino, and K. Morinag, Fabrication of transparent silica glass by powder sintering, Science and Technology of Advanced Materials **3**, 297 (2002).

[45] S. K. Milonjić, L. S. Čerović, D. M. Čokeša, and S. Zec, The influence of cationic impurities in silica on its crystallization and point of zero charge, Journal of colloid and interface science **309**, 155 (2007).

[46] K. Shun, Y. Hirai, O. Tabata, and T. Tsuchiya, Microfabricated cs vapor cells filled with an on-chip dispensing component, Japanese Journal of Applied Physics **60**, SCCL01 (2021).

[47] S. P. Alvarez, P. Gomez, S. Coop, R. Zamora-Zamora, C. Mazzinghi, and M. W. Mitchell, Single-domain bose condensate magnetometer achieves energy resolution per bandwidth below $\hbar$, PNAS **119**, e2115339119 (2022).

[48] C. Liu, B. Qian, R. Ni, and J. Qiu, 3d printing of multicolor luminescent glass, RSC Advances **8**, 31564 (2018).

[49] Q. Hu, X.-Z. Sun, C. D. Parmenter, M. W. Fay, E. F. Smith, G. A. Rance, Y. He, F. Zhang, Y. Liu, and D. Irvine, Scientific reports **7**, 17150 (2017).

[50] R. Bharadwaj and S. Mukherji, Gold nanoparticle coated u-bend fibre optic probe for localized surface plasmon resonance based detection of explosive vapours, Sensors and Actuators B: Chemical **192**, 804 (2014).
[51] G. F. Trindade, F. Wang, J. Im, Y. He, A. Balogh, D. Scurr, I. Gilmore, M. Tiddia, E. Saleh, D. Pervan, *et al.*, Residual polymer stabiliser causes anisotropic electrical conductivity during inkjet printing of metal nanoparticles, Communications Materials **2**, 47 (2021).
[52] F. Wang, J. H. Gosling, G. F. Trindade, G. A. Rance, O. Makarovsky, N. D. Cottam, Z. Kudrynskyi, A. G. Balanov, M. T. Greenaway, R. D. Wildman, *et al.*, Interflake quantum transport of electrons and holes in inkjet-printed graphene devices, Advanced Functional Materials **31**, 2007478 (2021).
[53] J. S. Austin, N. D. Cottam, C. Zhang, F. Wang, J. H. Gosling, O. Nelson-Dummet, T. S. James, P. H. Beton, G. F. Trindade, Y. Zhou, *et al.*, Photosensitisation of inkjet printed graphene with stable all-inorganic perovskite nanocrystals, Nanoscale **15**, 2134 (2023).
[54] A. L. Faria-E-Silva and C. S. Pfeifer, Impact of thiourethane additive and filler type on light-transmission and depth of polymerization of dental composites, Dental Materials **33**, 1274 (2017).
[55] P. Zhao, Y. He, G. F. Trindade, M. Baumers, D. J. Irvine, R. J. Hague, I. A. Ashcroft, and W. R. D., Modelling the influence of uv curing strategies for optimisation of inkjet based 3d printing, Materials & Design **208**, 109889 (2021).

APPENDIX

A1. Optimisation of printing parameters for the resin

By comparing the curing depth of the resins containing different concentrations of UV absorbers of 0.01 wt%, 0.02 wt%, 0.035 wt% and 0.05%, as shown in Figure A1, the 0.035 wt% was chosen as the optimum for the 50μm layer thickness used by the Lumen X printer, which results in a high geometrical fidelity at short printing times.

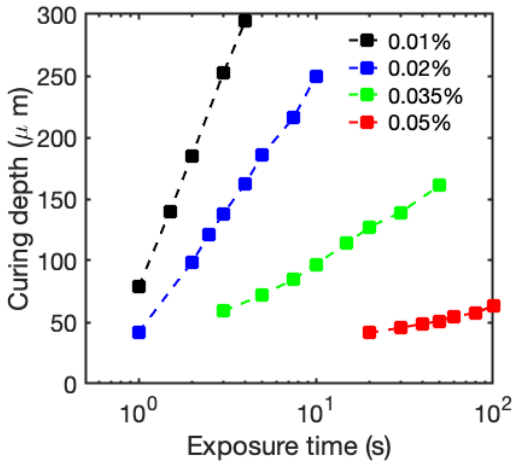

FIG. A1. Measured curing depth versus exposure time under irradiance of 45 mW/cm^2 UV light for resins with concentrations of UV absorbers of 0.01%, 0.02%, 0.035% and 0.05%.

A2. Modelling of scattered light of nanoparticles in the resin

Previous studies have highlighted that the existence of nanoparticles in UV curable resins promotes the curing depth due to the light scattered from the nanoparticles [54], and the extra energy overcures the photocurable material in the curing layer which reduces the printing resolution or even interferes with the curing of the next layer in DLP printing (A2a)). Following previous work on the modelling of polymerisation kinetics[55], the degree of curing caused by scattering in our resin formulation was calculated and confirmed that the formulated resin successfully suppressed the curing inhomogeneity caused by scattered light around the nanoparticles.

The scattered light intensity distribution, $I(\theta)$, due to Rayleigh scattering of one OX 50 nanoparticle can be calculated by

$$I(\theta) = I_0 \frac{1+\cos\theta}{2R^2} \left(\frac{2\pi}{\lambda}\right)^4 \left(\frac{n^2-1}{n^2+2}\right)^2 \left(\frac{d}{2}\right)^6 \tag{A1}$$

where $I_0 = 45\,\mathrm{mW/cm^2}$ is the intensity of the Lumen X printer used in this work, R is the mean distance between the particles, θ is the scattering angle, $n = 1.45$ is the refractive index of the resin, $d = 40\,\mathrm{nm}$ is the average diameter of the particle and $\lambda = 405\,\mathrm{nm}$ is the wavelength of the light.
Taking $R = 1.02\,d$, which matches the 50 wt% of nanoparticles in the resin, the distribution of the scattered light intensity $I(\theta)$ is anistropic and the scattered light is 1.9 times stronger along the direction of the incoming UV light (z-direction) than the perpendicular x-y-plane (Figure A1b)).

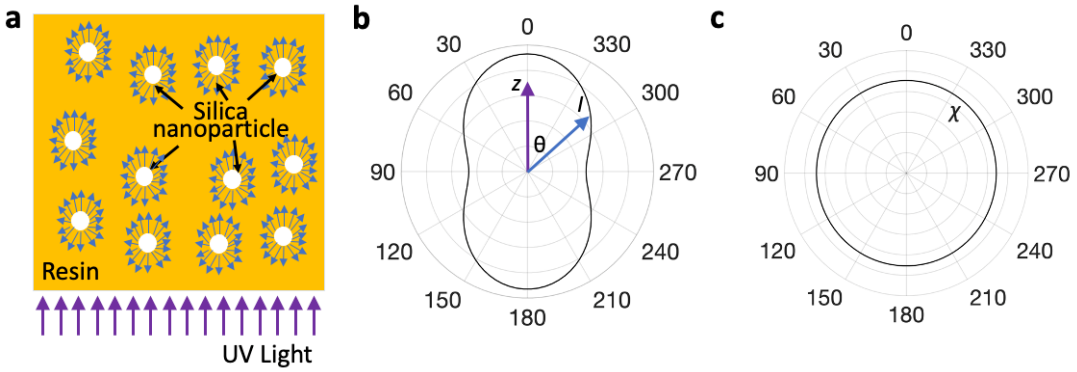

FIG. A2. a) Sketch showing the light scattering by the silica nanoparticles in the resin. b) Light scattering power density distribution from a silica nanoparticle when $R = 1.02d$ from equ. (A1). c) The resulting, homogeneous consumption of the vinyl group χ due to scattering around the nanoparticle from equ. (A2), when $R = 1.02d$ is chosen.

Despite the anistropic angular distribution of the scattered light intensity, the formulated resin exhibits an isotropic degree of polymerisation. The total consumption of the vinyl groups during polymerisation, χ, can be described by a model developed in [55], which combines classical theory of free radical polymerisation with consumption χ_p, and an autoacceleration effect with consumption χ_a,

$$\chi = \chi_p + \chi_a = \chi_{\mathrm{max,p}} \left(1 - e^{k_p \Lambda}\right) + \frac{\chi_{\mathrm{max,a}}}{1 + e^{k_a(\Lambda - \Lambda_C)}}, \tag{A2}$$

where $\Lambda = \sqrt{I}t$ is the UV radiation dose ($t = 6.5$ s is the exposure time), $\chi_{\mathrm{max,p}} = 0.2079$ and $\chi_{\mathrm{max,a}} = 0.5729$ are the maximum degrees of vinyl group consumption that can be achieved by the classical radical polymerisation and the autoacceleration polymerisation respectively. The rate constant of free radical polymerisation $k_p = -0.0083(\mathrm{kg/s})^{-1/2}$, the rate constant for the autoacceleration stage $k_a = -0.1258(\mathrm{kg/s})^{-1/2}$ and the required UV radiation dose to achieve half of the maximum degree of vinyl group consumption at the autoacceleration stage $\Lambda_C = 14.0719(\mathrm{kg/s})^{1/2}$ are parameters determined by the compositions of the monomers, photoinitiators and absorbers in the formulation utilising the method described in [55]. For the used resin formulation, the expected angular distribution for the degree of curing χ has an isotropic distribution as shown in Fig.A2, which indicates a similar degree of curing along all directions.

A3. Characterisation of printed and functionalised glass structures

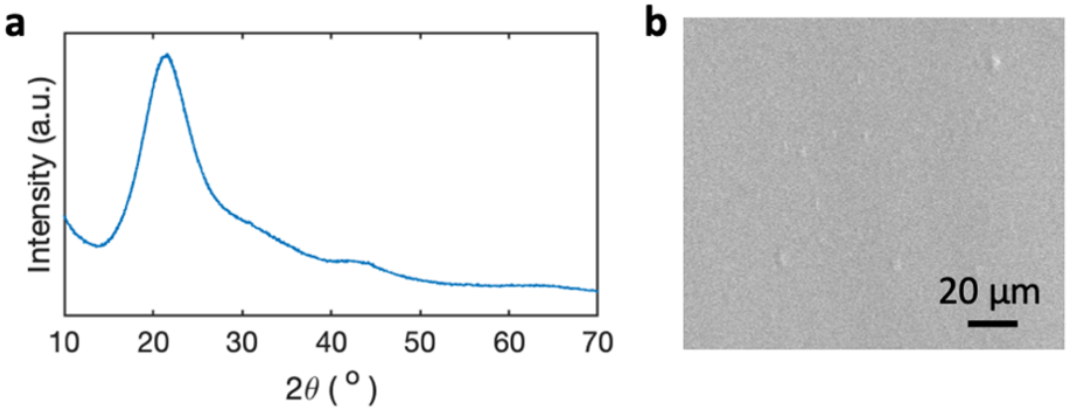

FIG. A3. a) X-ray diffraction (XRD) pattern and b) a representative, cross-section scanning electron microscope (SEM) image of the final printed glass part showing an amorphous structure after sintering.

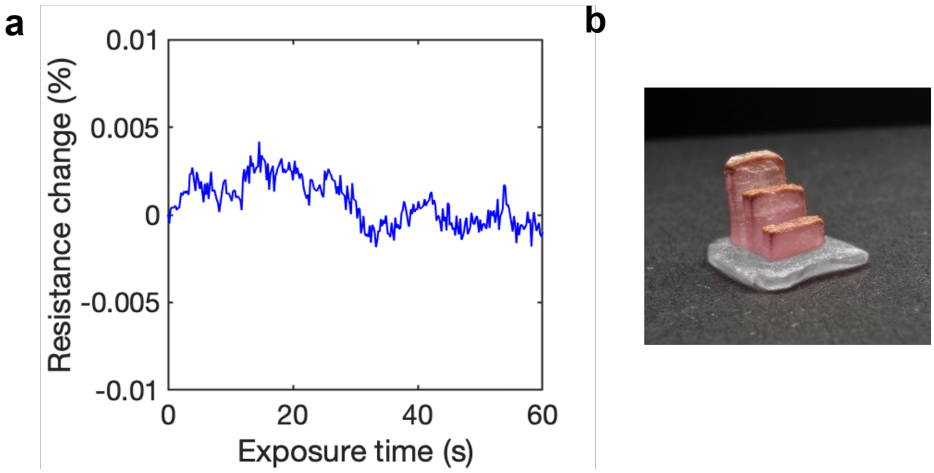

FIG. A4. a) Resistance change of a graphene track printed onto a non-doped glass slab during exposure to continuous illumination with green laser light (550 nm, P = 25 mW). b) Printed glass structures with two different colours. The base is without doping and the standing surfaces are doped with 0.5 mM AuNP.

A4. Laser locking comparison to Thorlabs 75 mm vapour cell

For laser frequency stabilisation, we compared the performance of our printed vapour cell to a standard Thorlabs 75 mm vapour cell. For laser locking with this cell, the probe beam is retro-reflected back through the cell, instead of separate probe and pump beams. Note that the total path length is 15 times that for the printed vapour cell. The resulting Allen deviation is shown in Figure A5.

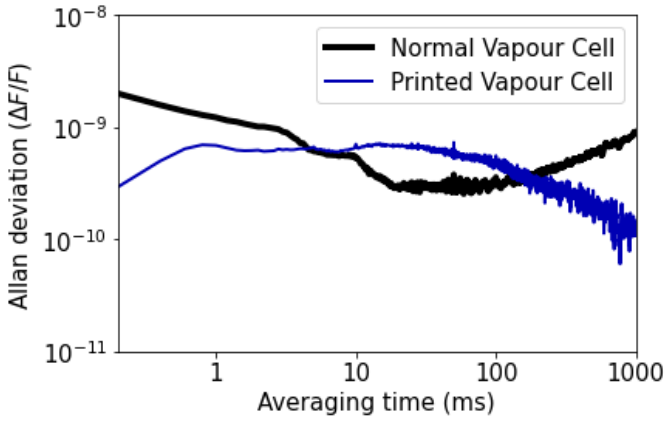

FIG. A5. Allan deviation comparison of the printed vapour cell and the commercial vapour cell, adjusted for the ratio of the corresponding optical path lengths.

A5. Polarisation characterisation of the printed vapour cell

The stability of the polarisation was also measured by analysing the polarisation over time (Figure A6). No time-dependent change (e.g. through a local temperature change) in polarisation was detected.

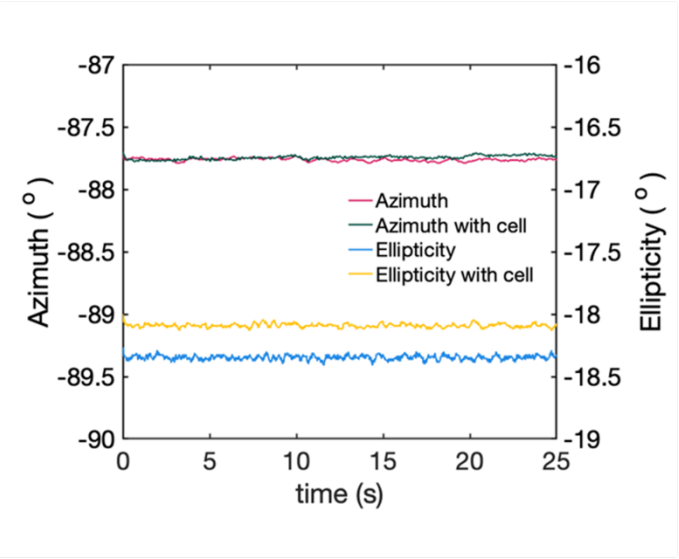

FIG. A6. The azimuth and ellipticity measured on a polarisation analyser over time, with and without the presence of the printed vapour cell, for a given incident polarisation.